universität wien

DISSERTATION

Titel der Dissertation

Radiation damage in ABO_4 minerals

Verfasserin

Diplom-Mineralogin Katja Ruschel

angestrebter akademischer Grad

Doktor der Naturwissenschaften (Dr. rer. nat)

Wien, 2011

Studienkennzahl lt. Studienblatt:	A 091 427
Dissertationsgebiet lt. Studienblatt:	Mineralogie-Kristallographie
Betreuer:	Univ.-Prof. Dr. Lutz Nasdala

Abstract

This work summarises several individual studies on radiation-damaged ABO_4 minerals that address aspects of the quantification of the radiation damage, its effects on material properties, and commonly occurring, subsequent alteration processes. Many natural minerals are characterised by structural damage that results from the radioactive decay of actinides. Such radiation damage is typically associated with property chances, including generally reduced physical stability and increased chemical reactivity. The insights gained are relevant for the Earth sciences as well as the materials sciences.

Two individual studies have focused on the ability of light-spectroscopic techniques to characterise the lattice disorder. For monazite–(Ce), a method to distinguish between effects of the chemical composition and the structural disorder on the Raman spectrum was developed. This method will be the indispensable premise for the Raman-spectroscopic estimation of the degree of radiation damage of natural monazite–(Ce). In the case of zircon, the spectroscopic evaluation of the radiation damage is a well-established method that has proved useful in many cases already. In a DAC (diamond anvil cell) study it was verified that the degree of the radiation damage in zircon can be quantified based on spectroscopic parameters even if samples are affected by high pressures.

In another study, a natural monazite–(Ce) sample that showed moderate radiation damage but heavy secondary alteration effects, was characterised in detail. It was found that a significant fraction of the thorium was released during the chemical alteration process, and re-deposited in fracture fillings. This leads to a critical assessment of the performance of orthophosphates as potential host materials for the storage of radioactive waste. By contrast, the ability of fergusonite–(Y) for the long-term immobilisation of radionuclides could be supported based on two detailed studies. The highly radiation-damaged fergusonite–(Y) samples investigated showed only a low mobility of the actinides incorporated, even though one of them had suffered severe chemical alteration. Raman- and luminescence spectroscopic changes observed upon thermal annealing of monazite–(Ce) and fergusonite–(Y) were compared to those of radiation-damaged baddeleyite.

Kurzfassung

Die vorliegende Arbeit fasst mehrere Teilstudien an strahlengeschädigten ABO_4-Mineralen zusammen, die sich mit der Quantifizierung der Strahlenschädigung, ihrer Auswirkung auf die Materialeigenschaften und den in Folge häufig auftretenden Alterationsprozessen beschäftigen. Viele natürliche Minerale weisen eine Schädigung ihrer Struktur auf, die auf den radioaktiven Zerfall von Aktinoiden zurückzuführen ist. Eine solche Strahlenschädigung geht typischerweise mit Änderungen der Materialeigenschaften einher, wie allgemein verringerter physikalischer Stabilität und erhöhter chemischer Reaktivität. Die diesbezüglich neuen Ergebnisse sind sowohl für erdwissenschaftliche als auch materialwissenschaftliche Belange von Bedeutung.

Die Eignung der Licht-Spektroskopie zur Charakterisierung der Gitter-Fehlordnung stand im Fokus zweier Teilstudien. So wurde für Monazit–(Ce) eine Methode entwickelt, um die Effekte von chemischer Zusammensetzung und struktureller Fehlordnung auf das Ramanspektrum auseinanderhalten zu können. Diese Methode bildet die Grundlage, um den Grad der Strahlenschädigung von natürlichem Monazit–(Ce) mit Hilfe der Ramanspektroskopie abzuschätzen. Für Zirkon hat sich die spektroskopische Evaluierung der Schädigung bereits seit längerem bewährt. Im Rahmen einer Studie wurde hier unter Verwendung einer Diamantstempelzelle nachgewiesen, dass eine spektroskopische Quantifizierung des Strahlenschädigungsgrades von Zirkon auch bei hohen Drücken möglich ist.

In einer weiteren Teilstudie wurde ein moderat strahlengeschädigter, aber stark sekundär alterierter Monazit–(Ce) detailliert charakterisiert. Durch den Alterationsprozess kam es hier zu großen Verlusten an Thorium sowie dessen Ablagerung in Rissfüllungen. Dies führt zu einer kritischen Beurteilung der Eignung von Orthophosphaten als potentielle Wirtsmaterialien für die Lagerung radioaktiver Abfälle. Im Gegensatz dazu konnte die Fähigkeit des Minerals Fergusonit–(Y) zur Langzeit-Immobilisierung von Radionukliden anhand zweier umfassender Studien unterstrichen werden. Die untersuchten, hoch strahlengeschädigten Fergusonite–(Y) zeigten, ungeachtet der in einem Falle erfolgten intensiven chemischen Alteration, lediglich eine geringe Mobilität der enthaltenen Aktinoide. Raman- und lumineszenzspektroskopische Veränderungen beim thermischen Ausheilen von Monazit–(Ce) und Fergusonit–(Y) wurden mit jenen von strahlengeschädigtem Baddeleyit verglichen.

Table of contents

1 Introduction

Many natural minerals incorporate the actinides U and Th in their structure. Through the radioactive decay processes of these actinides and their daughter nuclei the minerals suffer irradiation, and damage is commonly created in the mineral structures. The overall goal of this work was to gain new insights into radiation-damaged minerals, especially the radiation-induced changes in physical and chemical properties, and subsequent alteration processes.

A concise introduction to radiation damage in minerals and the relevance of research in this field for Earth sciences and materials sciences is provided in subchapter 1.1. Raman spectroscopy was a particularly relevant method for the present work. In all five individual studies, the method was applied to characterise the structural state of minerals, and in two of these studies, its ability to quantify the radiation damage of minerals was examined. Therefore a short introduction to Raman spectroscopy is given in subchapter 1.2. Note that an in-depth treatment of the physical background is beyond the scope of this thesis. The research objectives of this thesis are described in more detail in subchapter 1.3. Results obtained in the individual studies are documented in chapter 2, in the form of published papers (subchapters 2.1-2.4), a submitted manuscript (subchapter 2.5), and some preliminary results, which in part have been published as conference contributions (subchapter 2.6). The results are followed by a final discussion and implications, including a brief discussion on the analytical techniques used for the studies.

1.1 Radiation damage

Radiation damage is induced in a crystalline structure by high-energy radiation. The degree of damage may vary from a partial destruction of the structure to the formation of a completely amorphous state of the material. Irradiation of a mineral may occur due to internal radiation sources that is radioactive elements incorporated in the crystal structure (e.g., Nasdala et al. 2004) or due to external radiation sources. The latter include natural ones [e.g., inclusions of actinide-bearing minerals (e.g., Nasdala et al. 2006)] and artificial ones [e.g., irradiation experiments with ions or electrons (e.g., Meldrum et al. 1997; Krickl et al. 2008; Nasdala et al. 2011)].

Three processes may cause self-irradiation damage in minerals: alpha decay, beta decay and spontaneous fission events. Out of these, alpha decay events are considered to be responsible for most of the self-irradiation damage in actinide-containing minerals (Murakami et al. 1991; Weber et al. 1998). Beta-decay is considered to be generally ineffective in generating permanent damage. A spontaneous fission event is able to create extensive damage, but due to its low probability of occurring, fission events do not significantly contribute to the damage accumulation in actinide-bearing solids.

During an alpha decay event an unstable (radioactive) isotope spontaneously transforms into a heavy daughter nucleus and an alpha particle (i.e., a ^{4}He nucleus) (see Fig. 1). The alpha particle is emitted with a kinetic energy of ~3.9–8.8 MeV and is able to move a few tens of micrometers through the mineral. It will mainly loose its energy by ionisation processes, but particularly near the

end of its path the alpha particle collides with other atoms and may cause up to a few hundred Frenkel defect pairs (Weber et al. 1998). The heavy daughter nucleus experiences a recoil impulse. Compared to the alpha-particle, the recoil nucleus has a lower kinetic energy of ~0.1 MeV and its stopping range is only a few tens of nanometres (Murakami et al. 1991; Nasdala et al. 2001). Nevertheless the nuclei will lose most of its energy in elastic collisions with nuclei of lattice atoms and generate thousands of displacements due to its high atomic mass. A damage cluster by collision cascades of displaced lattice atoms may result (Murakami et al. 1991; Weber et al. 1998; Nasdala et al. 2001). An additional reason for the appreciable contribution of alpha-decay events to damage accumulation is that the decay chain of a single actinide ion consists of several successive alpha-decays. The isotopes ^{238}U, ^{235}U and ^{232}Th undergo eight, seven and six alpha-decays, respectively until their stabile isotopes ^{208}Pb, ^{207}Pb and ^{206}Pb are formed.

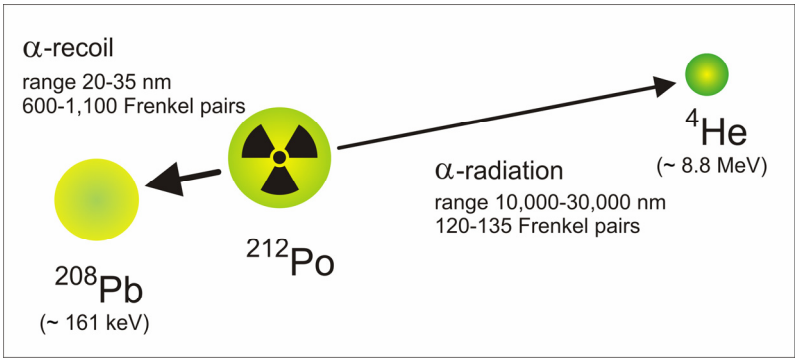

Fig. 1 Formation of an alpha-particle and an alpha-recoil nuclei during an alpha-decay event.

The accumulation of radiation damage may lead to complete destruction of the crystal structure. The transition of the crystalline to the amorphous state of the material is referred to as metamictisation (Ewing 1994; Zhang et al. 2002). There exist several models to explain the process of metamictisation: (i) progressive (homogeneous) amorphisation due to point defect accumulation, (ii) interface-controlled amorphisation, (iii) cascade-overlap (heterogeneous) amorphisation and (iv) in-cascade (heterogeneous) amorphisation (see Weber 1998 and references therein). Note, however, that amorphisation of a mineral might involve more than one of these processes and so far for most minerals no well-defined model exists (Weber et al. 1998).

However, whether or not a mineral becomes metamict depends on the damage accumulation, as well as, the damage recovery upon thermal annealing (Meldrum et al. 1998). As long as the damage accumulation rate is less than or equal to the annealing rate, complete amorphisation can not occur. The temperature above which no amorphisation can be induced under particular conditions is defined as the critical amorphisation temperature (T_c) and is specific to the material (Meldrum et al. 1998, 2000; Ewing 2005). Recovery of the structure is not restricted to thermal annealing. Irradiation (i.e., electron beams or alpha particles) (Meldrum et al. 1996; Ouchani et al. 1997; Harrison et al. 2002) or recrystallisation processes (e.g., through an alteration event) (Nasdala et al. 2001) might also cause structural reconstitution.

As a consequence of an increasing degree of radiation damage, the physical durability of minerals is reduced and their chemical reactivity increased (Lumpkin 2001; Horie et al. 2006; Lenting et al. 2010). Changes of physical properties may include decreases in elastic properties and

hardness (Chakoumakos et al. 1991; Weber et al. 1998; Ewing et al. 2003; Picot et al. 2008) and changes in optical properties (Holland & Gottfried 1955; Nasdala et al. 2009). Furthermore radiation-induced expansion of the unit cell (volume swelling) and a decrease of density are commonly observed (Holland & Gottfried 1955; Bakker et al. 1998; Picot et al. 2008).

The (sometimes heterogeneous) volume expansion of the material may cause microfractures in the material (Fig. 2; see e.g., Chakoumakos et al. 1987; Weber et al. 1998). The subsequently increased surface area enhances fluid access and dissolution (Lee & Tromp 1995). Such fluid transport through cracks and voids is typical for secondary alteration processes, e.g. hydrothermal overprinting or near-surface weathering processes (Lumpkin & Ewing 1995). The process of fluid-driven alteration may cause extensive element mobilisation and is often referred to as "dissolution–reprecipitation" (Putnis 2002). In contrast, primary alteration is mostly dominated by intracrystalline elemental diffusion. Such diffusion, as well as the susceptibility of the minerals to dissolution is typically enhanced by radiation-induced disorder and amorphisation (Lumpkin 2001; Cherniak & Watson 2003; Tromans 2006).

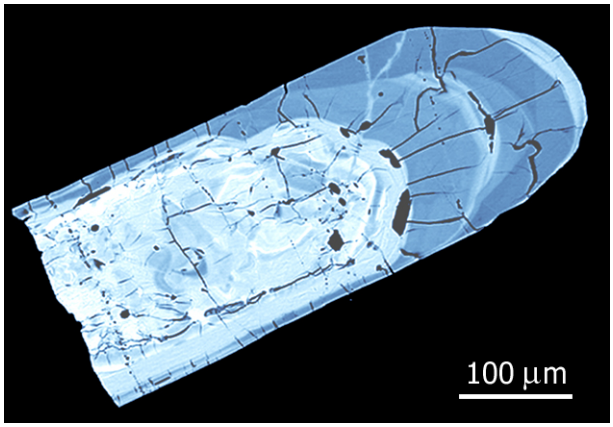

Fig. 2 Back-scattered electrons image of a complexly zoned zircon grain from a gneiss from Afella, In Ouzzal Massif, Algeria. Image modified from Nasdala et al. (2001), for details on the host rock see Peucat et al. (1996). The strongly radiation-damaged central zone (bright BSE) is more volume-expanded than the surrounding zones; it is hence surrounded by the typical radial fracture pattern.

Knowledge on the degree of radiation damage may yield important information in reconstructing the geological history of a mineral. As an effect of alteration processes, the U–Th–Pb system of a mineral may be disturbed by depleting and/or enriching, actinide and/or Pb concentrations (Suzuki et al. 1994; Goncalves et al. 2005; Kuiper 2005). Such isotopic disturbance may bias dating results that is the mineral may be affected by the generation of normal or reverse discordance, or data interpretation may be completely prevented. Understanding the mechanisms that might affect the U-Th-Pb system is fundamental for the interpretation of dating results (e.g., to better understand the post growth history of minerals and to avoid biased age data). Hence investigations on geochronological significant minerals, like zircon, monazite–(Ce) and apatite (commonly used for U/Th–Pb dating or fission-track dating) are of particular interest.

Minerals that are able to incorporate actinides in their crystal structure (e.g., zircon, zirconolite, monazite–(Ce), pyrochlore, etc.) are commonly discussed as potential carrier phases for actinides in ceramic nuclear waste forms (Ewing 1999; Trocellier 2000; Lumpkin 2006; Omel'yanenko et al. 2007; Weber et al. 2009; Montel 2011). Any release of radionuclides from the waste forms has to be prevented. Hence long-term chemical and mechanical durability (including mechanical strength, thermodynamic stability, etc.) are essential properties of waste forms for the

immobilisation of actinides (Ewing 1999). As underground repositories are commonly discussed for the disposal of such nuclear waste forms, it needs for instance to be considered that groundwater infiltration might affect the waste form. Therefore low solubility in natural fluids is of crucial importance for potential waste form phases. The susceptibility of materials to undergo chemical alteration, the chemical alteration process itself and as to which degree these materials can resist the release of radionuclides is of particular interest.

It is therefore understandable that radiation-induced property changes in minerals provided a wide area of research in recent years. Information on the suitability and performance of materials for the immobilisation of radionuclides (e.g., their alteration behaviour) is obtained from laboratory experiments performed on natural and synthetic materials as well as from observations on natural minerals. Laboratory studies such as irradiation or leaching experiments offer a number of advantages. The behaviour of minerals can for instance be studied under controlled conditions (e.g., under high temperature, high pressure, etc.), or the stability of different minerals under identical conditions can be compared (e.g., Meldrum et al. 2000; Terra 2003). Nevertheless all the experimental investigations have to be supported by observations made on naturally radiation-damaged and/or naturally chemically altered mineral samples. Natural minerals are able to provide information on the long-term accumulation of radiation damage in crystals and on their long-term behaviour (including chemical alteration processes) in a geological environment (e.g., in the presence of aqueous solutions). In short-term laboratory experiments, such natural processes, proceeding at a low temperature over millions of years, can not be simulated.

1.2 Raman spectroscopy

The Raman effect was observed for the first time in 1928 by the Indian physicist C.V. Raman (Raman & Krishnan 1928). It describes an interaction of an electromagnetic wave with matter (gasses, liquids or solids). The decisive process is the inelastic scattering of a light quantum (photon) from the examined molecule (respectively crystal lattice). For this an electromagnetic radiation, commonly monochromatic laser light in the visible range, is focused onto the sample and the energy-shifted fraction of the scattered light is detected.

The quantum-mechanical model is often used to explain the Raman effect in terms of the discrete vibrational energy states of each molecular vibrational mode. According to this model, an incoming photon might be absorbed if its energy matches to the energy difference between two allowed vibrational levels of a molecule. A quantum of vibrational energy (phonon) with the same energy is excited. This may occur upon irradiation with middle to far infrared light.

In the case of visible light no such absorption can take place. Here, the incoming photon excites the system to a virtual state. In most cases, upon relaxation of the excited state a new photon is emitted, having the same energy as the photon of the incident laser light, and the remaining molecule has the same vibrational state as before. Such a scattering process, where no energy is transferred, is called elastic or Rayleigh scattering. However, very rarely a vibrational transition to a higher or lower vibrational state than before the interaction is induced. In this case an energy transfer occurs and the photon energy of the scattered light is different from the incident

one. This process is called inelastic or Raman scattering. The energy differences between Raman-scattered photons and incident photons are equal to the difference in energy between two vibrational states of the molecule. If energy is transferred from the incident light to raise a vibration to the excited state, the scattered light shows a shift towards lower energies. This red shift is called the Stokes scattering. If energy is transferred from an already excited vibration that relaxes to the ground state, a vibrational phonon is destroyed and the scattered light shows a shift towards higher energies. This blue shift is called the anti-Stokes scattering. Accordingly, for the occurrence of anti-Stokes scattering the existence of molecules in an excited state is required. Further it is obvious that anti-Stokes scattering increases with rising temperature. Under ambient conditions Stokes scattering in the dominant process and the Stokes part of a Raman spectrum is recorded and considered for most applications.

Another approach to explain inelastic Raman scattering is to apply an electro-dynamical model. According to this model the electric field of the laser light induces a time-dependent dipole momentum in the molecule. The interaction of the time-dependent dipole momentum and the electromagnetic wave of the laser beam itself is controlled by the polarisability of the molecule. Molecular vibrations are only Raman active if the polarisability for the molecule changes with time. Number and type of possible vibrations can be calculated using group theory. The so-called (group theoretical) selection rules describe whether or not a vibrational mode is Raman active.

A Raman spectrum is a plot of light intensity versus the photon energy. The energy shift of the inelastic scattered light relative to the elastic scattering is called the Raman shift and usually given in relative wavenumbers. Anti-Stokes Raman bands have negative and Stokes Raman bands have positive relative wavenumbers. The Rayleigh line is observed at zero Raman shift.

A Raman system typically consists of several major components: (1) an excitation source (laser), (2) a sample illumination system and light collection optics, (3) dispersive gratings for spectral decomposition, and (4) a detector. Mirrors or glass fibres guide the laser beam through a beam expander and a laser line rejection filter (edge filter or notch filter) reflects the beam through a microscope onto the sample, where it interacts with the sample in the focal spot. The scattered light is collected by a microscope objective and directed on the laser line rejection filter, which rejects the elastically scattered light from entering the spectrometer. Only the inelastically scattered light passes and is spectrally decomposed by the dispersive gratings in the spectrometer before it is projected into the detector. In most instruments charge coupled device (CCD) detectors are used.

For a high spatial resolution and a reduction of the sampling volume an instrument with a confocal arrangement of the optical pathway is applied. Such instruments allow performing so-called "microprobe" analyses with a volume resolution better than 5 μm^3 (Markwort et al. 1995). A disadvantage of the confocal setup is the reduced light collection efficiency. For routine analyses a compromise between non-confocal and confocal mode may be reached using a pseudo-confocal instrument setup (Williams et al. 1994), which compared to a non-confocal aligned instrument offers an improved spatial resolution and compared to confocal systems a good light throughput.

It should be noted that Raman spectral parameters (especially Raman band intensities) depend on the crystallographic orientation of the sample relative to the polarisation plane of the

laser light. Hence in some cases oriented measurement might be required to allow a sensible comparison of Raman spectra.

Applications of Raman spectroscopy cover a wide field including for instance Earth sciences, archaeological sciences, forensic sciences, polymer research, semiconductor physics, etc. The Raman spectrum is highly specific for a certain substance and is mostly used as a "fingerprint method" for the identification of a material. In Earth sciences Raman spectroscopy is, besides for the identification of mineral phases, often used for structural investigations. It proved for instance to be a suitable method to study the short-range order of minerals. The decreased short-range order of radiation-damaged minerals can commonly be observed from spectral changes, such as band shifts (typically toward lower wavenumbers), increases of their widths (commonly expressed as FWHMs), intensity losses, and sometimes band asymmetries. Additionally the splitting of Raman bands or the appearance of additional bands might occur in a spectrum. For zircon the quantification of the degree of radiation damage by means of Raman spectroscopy is a well-established method (e.g., Geisler et al. 2001; Nasdala et al. 2001).

Note that for quantitative conclusions concerning Raman band width a band correction procedure has to be applied to obtain the real FWHMs (see e.g., Dijkman and van der Maas 1976). Further it needs to be considered that a suitable laser excitation wavelength is chosen for Raman analyses to avoid that the Raman signal is affected or even obscured by any simultaneously emitted photoluminescence signal. In principle Raman spectroscopy is a non-destructive method. Only in rare cases does the local temperature increase result in artefacts, such as the decomposition of the sample. Raman analyses do not require special preparation of the sample. Grains can be analysed as well as polished samples. Even mineral inclusions can be studied, as measurements can be done without any direct contact to the sample. Due to the high volume resolution small amounts of sample material as well as minerals showing a fine-scale zoning can be analysed.

1.3 Research objectives

Three ABO_4 minerals were in the focus of the present thesis (nominal chemical formulas in parentheses): monazite–(Ce) ($CePO_4$), zircon ($ZrSiO_4$) and fergusonite–(Y) ($YNbO_4$). They commonly incorporate actinides and are considered as potential carrier phases for the long-term immobilisation of radionuclides. In addition, monazite–(Ce) and zircon play an important role for a wide range of geochemical investigations and are often used for radiometric dating, which makes a better understanding of the alteration mechanisms crucial for these minerals.

The first main objective of this thesis, an evaluation of the potential of Raman spectroscopy to quantify the degree of short-range order in radiation-damaged minerals, is attended to in two studies (subchapters 2.1 and 2.5).

The band width of the zircon $\nu_3(SiO_4)$ Raman band is a reliable indicator of the degree of self-irradiation damage for zircon samples. The study reprinted in subchapter 2.1 was dedicated to the question whether the Raman band parameters can indicate the degree of radiation damage under high pressure conditions. Pressure-induced Raman spectral parameter changes of zircon

samples with different degrees of self-irradiation damaged and synthetic zircon have therefore been studied under hydrostatic compression in a diamond anvil cell (DAC).

The second study (subchapter 2.5) investigated the potential of Raman spectroscopy to estimate the degree of accumulated radiation damage in monazite–(Ce) samples whose chemical composition has been determined before. The degree of disorder generally depends on both the structural state and the chemical composition of the material. Regarding that monazite–(Ce) has an extremely broad range of chemical compositions it is hence crucial to primarily investigate how the chemical composition affects the monazite–(Ce) Raman spectrum. This was done on synthetic orthophosphates and non radiation-damaged analogues of the naturally radiation-damaged monazite–(Ce) samples, produced by dry annealing. Knowledge on the effect of chemical composition on the Raman spectrum might then be used to estimate the degree of structural radiation damage from the observed spectrum of a natural sample.

The second main objective was to study the effects of radiation damage and subsequent alteration processes on natural minerals. The samples studied in three case studies include a monazite–(Ce) sample from Moss (Norway) (subchapter 2.4), and fergusonite–(Y) samples from the Berere region (Madagascar) (subchapter 2.3) and Adamello (Italy) (subchapter 2.2). The samples were structurally and chemically characterised in detail using a broad range of imaging, spectroscopic and elemental (respectively isotope) techniques. Due to the reasons outlined in 1.1 the potential mobility of the actinides and Pb was of particular interest in these studies.

For three different radiation-damaged minerals, namely monazite–(Ce), fergusonite–(Y) and baddeleyite the Raman- and photoluminescence spectroscopic changes upon thermal annealing were compared (some preliminary results are presented in subchapter 2.6).

2.1 Raman study of radiation-damaged zircon under hydrostatic compression

(2008)

Nasdala, L., Miletich, R., Ruschel, K. & Váczi, T.

Physics and Chemistry of Minerals, 35:597–602

Phys Chem Minerals (2008) 35:597–602
DOI 10.1007/s00269-008-0251-5

ORIGINAL PAPER

Raman study of radiation-damaged zircon under hydrostatic compression

Lutz Nasdala · Ronald Miletich · Katja Ruschel · Tamás Váczi

Received: 25 April 2008 / Accepted: 19 June 2008 / Published online: 21 August 2008

Abstract Pressure-induced changes of Raman band parameters of four natural, gem-quality zircon samples with different degrees of self-irradiation damage, and synthetic $ZrSiO_4$ without radiation damage, have been studied under hydrostatic compression in a diamond anvil cell up to ~10 GPa. Radiation-damaged zircon shows similar up-shifts of internal SiO_4 stretching modes at elevated pressures as non-damaged $ZrSiO_4$. Only minor changes of band-widths were observed in all cases. This makes it possible to estimate the degree of radiation damage from the width of the $\nu_3(SiO_4)$ band of zircon inclusions in situ, almost independent from potential "fossilized pressures" or compressive strain acting on the inclusions. An application is the non-destructive analysis of gemstones such as corundum or spinel: broadened Raman bands are a reliable indicator of self-irradiation damage in zircon inclusions, whose presence allows one to exclude artificial color enhancement by high-temperature treatment of the specimen.

Keywords Zircon · Radiation damage · Diamond anvil cell · Raman spectroscopy

L. Nasdala (✉) · K. Ruschel · T. Váczi
Institut für Mineralogie und Kristallographie, Universität Wien, Althanstr. 14, 1090 Wien, Austria
e-mail: lutz.nasdala@univie.ac.at

R. Miletich
Mineralogisches Institut, Ruprecht-Karls-Universität Heidelberg, Im Neuenheimer Feld 236, 69120 Heidelberg, Germany

Introduction

The accumulation of self-irradiation damage in zircon ($ZrSiO_4$) leads to dramatic changes of physical properties and chemical resistance of this mineral and may finally lead to an amorphous "metamict" form (e.g., Ewing et al. 2003). The damage originates from the radioactive decay (i.e., alpha-decay events) of U and Th substituting on the Zr^{4+} sites within the lattice, and their instable daughter nuclei in the respective decay chains. The degree of radiation damage that is present in a certain sample, however, does not necessarily correlate with the self-irradiation dose. It has been shown that radiation damage is the result of the two competing processes damage accumulation and damage annealing, controlled by the sample's thermal history (Meldrum et al. 1999).

Nasdala et al. (1995) have introduced Raman spectroscopy as a method to estimate quantitatively the degree of radiation damage in zircon. They showed that Raman spectra of mildly to strongly radiation-damaged (but not yet amorphized) zircon show the same pattern of Raman bands as crystalline zircon. Bands, however, clearly shift towards lower wavenumbers and broaden, which reflects the loss of short-range order and the general expansion of the lattice. The FWHM (full width at half band-maximum) of the internal $\nu_3(SiO_4)$ mode at ~1,000 cm^{-1} was found to increase most sensitively with increasing radiation damage. It increases from <2 cm^{-1} for well-crystallized (i.e., undamaged) to well above 30 cm^{-1} for strongly radiation-damaged zircon. This parameter was used in many recent studies to estimate the degree of metamictization of unknown zircon samples. The Raman-based estimation of radiation damage provides the opportunity to do non-destructive in situ analyses with resolution on a micron-scale, opening up new opportunities for studying

the structural state of single zones and areas within zircon grains, and their internal heterogeneity. Applications were presented, for instance, by Wopenka et al. (1996), Hoskin and Black (2000), Zhang et al. (2000), Balan et al. (2001), and Pidgeon et al. (2007).

The objective of the present paper is to study the Raman spectral changes of radiation-damaged zircon (or, more precisely, zircon-structured $ZrSiO_4$) at elevated pressure. Such data have only been provided for crystalline zircon thus far by Knittle and Williams (1993), who found that $ZrSiO_4$ transforms from the zircon-type to a scheelite-type high-pressure polymorph at $\sim$37 GPa. Pressures applied in the present study have remained well below this transition. Note that the present study deals with effects of hydrostatic compression on the spectral behavior of zircon with accumulated self-irradiation damage. It is therefore not closely related to recent papers addressing the question how pressure affects the formation of local material changes, i.e., the process of damage accumulation due to relativistic heavy ions under pressure (e.g., Glasmacher et al. 2006; Lang et al. 2005, 2008). In contrast, we have focused on the following questions: (1) which spectral changes are observed for existing radiation damage in zircon on pressure changes within the hydrostatic regime; (2) as to which degree trends of spectral changes of significantly radiation-damaged zircon differ from those of non-damaged $ZrSiO_4$; and finally (3) whether or not the presence of pressure affects the quantification of radiation damage using the FWHM of the $\nu_3(SiO_4)$ Raman mode.

Samples and experimental

We have studied small chips of four zircon gemstones (ages 522–571 Ma) originating from the Sri Lankan Highland Complex, and synthetic (un-doped) $ZrSiO_4$. The latter was grown using the Li–Mo flux technique described by Hanchar et al. (2001). Chemical and isotopic composition and structural state of the four natural samples, namely M144, BR231, OR1, and G168, have been described in detail elsewhere (Nasdala et al. 2004). They cover the range from mildly (M144; 436 ppm U) to strongly radiation-damaged (G168; 1,499 ppm U). For analytical characterization of the synthetic (i.e., very-well crystallized) $ZrSiO_4$ see Nasdala et al. (2002b).

High-pressure experiments up to $\sim$10 GPa were performed in three runs using an "ETH-type" diamond anvil cell (DAC) that has been described in detail by Miletich et al. (2000). For all three individual loadings 0.09 ct type Ia low-fluorescence diamond anvils with 0.6 mm culets were placed on standard Be backing plates with 15° opening angles for the optical ports. The pre-indented steel gaskets had thicknesses of 85–95 μm, and the diameter of the mechanically-drilled circular pressure chamber was in the range 205–250 μm. The cell was loaded with one or two un-oriented crystal fragments (longest dimensions 90–150 μm). Cryogenically loaded argon was used as pressure-transmitting medium. For the determination of pressure inside the DAC, several small ruby spheres (sizes ca. 5–10 μm) were loaded together with zircon fragments. Pressures were calculated from the spectral position of the laser-induced R_1 emission line ($^2E \rightarrow {}^4A_2$ transition; Nelson and Sturge 1965) of Cr^{3+} centers incorporated in Al_2O_3. The R_1 emission lies at 14,405 cm^{-1} (which corresponds to $\lambda = 694.2$ nm) at ambient conditions and is shifted to lower wavenumbers (i.e., higher wavelengths) at elevated pressures. Calibrations have been provided, for instance, by Piermarini et al. (1975) and Mao et al. (1986). Measurements were done at least 30 min after manual pressure increase or decrease, to reach equilibrium conditions of pressure setting in the DAC. Pressures were derived from the wavelength shift relative to the respective measurement at 1 bar after complete pressure release, using the empirical calibration parameters given by Mao et al. (1986) for hydrostatic conditions.

Raman spectra were obtained by means of a Renishaw RM1000 spectrometer equipped with Leica DMLM optical microscope, a grating with 1,200 grooves per mm, and a Peltier-cooled charge-coupled device (CCD) detector. Spectra were excited with the 785 nm emission line of a NIR (near infrared) diode laser. The laser power at the sample was $<$3 mW, which is well below the threshold for any heating effects that hypothetically could be caused by local absorption of the laser light. A 20× ULWD (ultra-long working distance) objective (numerical aperture 0.40, free working distance $\sim$11 mm) was used. With this objective, the lateral resolution (with the system operated in the quasi-confocal mode) is estimated at about 20–30 μm, which was powerful enough for our needs. The spectrometer was calibrated using neon lamp emissions (cf. Lide 2003), in particular those at 14219.87 cm^{-1} (703.24 nm), 14431.12 cm^{-1} (692.95 nm), and 14887.5 cm^{-1} (671.7 nm), and the Rayleigh line. All spectra were obtained in the "continuous extended scan" mode, with accumulation times of 10 s for the Rayleigh and neon lamp lines, 30 s for the ruby R lines, and between 60 s (synthetic $ZrSiO_4$) and 900 s (OR1, G168) for zircon Raman spectra. The wavenumber accuracy was better than 0.5 cm^{-1}, and the spectral resolution was determined at $\sim$2.5 cm^{-1}.

Fitting was done assuming Lorentzian–Gaussian band shapes (except for the Rayleigh line, for which a simple Gaussian shape was assumed). Measured FWHMs were corrected for the experimental band broadening (i.e., apparatus function, spectral width of laser emission), and real FWHMs were calculated according to the procedure of

Verma et al. (1995). Estimated uncertainties of corrected FWHMs of the zircon $\nu_3(SiO_4)$ Raman band were between ± 0.4 cm^{-1} (synthetic $ZrSiO_4$) and ± 1.2 cm^{-1} (G168). Uncertainties of determined pressures are assessed to be below ± 0.1 GPa.

Results and discussion

Representative zircon Raman spectra obtained with 785 nm excitation are presented in Fig. 1. Near infrared (NIR) excitation was preferred for two reasons. First, the spectral resolution of a dispersive spectrometer is better at longer wavelengths. This results in bands being defined by more data points, which improves the reliability of fit results especially for narrow bands. Second, with visible excitation, zircon Raman bands are likely to be affected by simultaneously excited laser-induced luminescence emissions. In test measurements with He–Ne 632.8 nm excitation it turned out that the (comparably weak) Raman spectrum of zircon was fully obscured by Cr^{3+} sidebands. Note that in the emission spectrum of Cr^{3+} in corundum, the main R_1 and R_2 lines (emissions of single Cr^{3+} ions) are accompanied by N_1 and N_2 lines (emissions of pairs of closely neighbored Cr^{3+} ions, at 704.1 and 700.9 nm; Powell 1967) and extended sidebands (main emissions modulated by vibrations which have strong intensity in the range 645–740 nm; Rothamel et al. 1983). Even though sidebands are much less intense than R lines, they are still several orders of magnitude higher in intensity than Raman bands. Test measurements with Ar^+ excitation (488 and 514.5 nm) showed significant problems with luminescence phenomena in the case of natural zircon samples. These emissions are assigned to rare earth element (Gaft et al. 2000; Nasdala and Hanchar 2005) and unknown broad-band emission centers in the zircon structure (Gaft et al. 2002).

It should be mentioned that hypothetical problems to excite the red ruby luminescence with the NIR laser did not occur. Direct (i.e., single-photon) excitation of the R_1 emission (photon energy ~ 1.79 eV) was of course impossible, because of the too low photon energy of 785 nm laser light (~ 1.46 eV). Nevertheless, the R lines were excited, and obtained, with sufficient intensity. This may possibly be assigned to a two-photon excitation process.

Natural zircon shows in general comparably weak luminescence in the NIR. However, in spite of the fact that 785 nm excitation was used, the (low-intensity) Raman spectra of all four natural samples were notably affected by luminescence, especially in the range below 834 nm (corresponding to Raman shifts smaller than 750 cm^{-1}; Fig. 1). Nevertheless, the two main Raman bands of zircon at about 1,000 cm^{-1} could be obtained in all cases. These bands are assigned to symmetric stretching (ν_1; A_{1g} mode at ~ 974 cm^{-1}) and antisymmetric stretching (ν_3; B_{1g} mode at $\sim 1{,}008$ cm^{-1}) of SiO_4 tetrahedra in the zircon structure (Dawson et al. 1971; Syme et al. 1977; Mazhenov et al. 1979). Reliable background correction was possible in spite of the significant background intensity, because of the nearly linear (slightly concave) background shape in our spectra (Fig. 1). In contrast, correction for background luminescence consisting of a multitude of narrow emissions (as for instance occurring when Ar^+ 514.5 nm excitation is used; Nasdala and Hanchar 2005) would have introduced clearly more uncertainty. In Fig. 1, background correction and band fitting results are demonstrated for the example of the 5.1 GPa spectrum of zircon OR1.

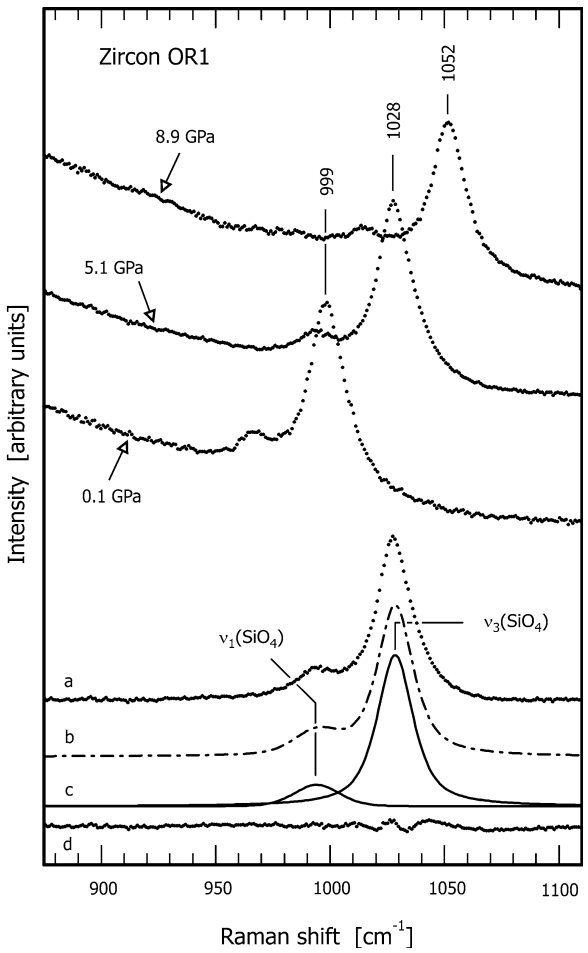

Fig. 1 Raman spectra (785 nm excitation) of zircon OR1 from Sri Lanka, obtained at different pressures. To demonstrate band deconvolution, background-corrected spectrum (**a**), fit result (**b**), fitted single bands (**c**), and difference plot (**d**) are shown below for the example of the 5.1 GPa spectrum

Calculated difference graphs indicated that obtained Raman bands were not affected by significant band asymmetry. This observation is important insofar as it supports quasi-hydrostatic conditions as expected for the pressure medium (argon) used. In contrast, lattices affected by strain due to deviatoric stress under non-hydrostatic conditions typically yield notably asymmetric Raman bands (heterogeneous band broadening; see for example Figs. 1 and 3 in Sharma et al. 1985, Fig. 2b in Nasdala et al. 2002a), which was not observed in the present study over the whole range of experimentally achieved pressures.

Results are shown in Fig. 2. As expected, bands of SiO_4 stretching modes were found to shift towards higher relative wavenumbers (i.e., higher Raman shifts) with increasing pressure. Only for synthetic $ZrSiO_4$ Raman bands in the spectral range below 750 cm^{-1} could be measured (see above). Here, we found that SiO_4 bending and most external modes (including the translational E_g band at 225 cm^{-1}) are up-shifted with pressure, whereas the E_g band at 202 cm^{-1} shows a marked down-shift (to 196 cm^{-1} at 9.0 GPa). All band shifts seemed to occur nearly linearly with pressure, i.e., there was no any clear indication of a hypothetical phase transformation. For the main $\nu_3(SiO_4)$ zircon band, pressure-induced upshifts ($d\tilde{\nu}/dP$) of 5.4–5.9 cm^{-1} GPa^{-1} were calculated for the five samples. These values are slightly higher than the vibrational mode shift of 4.8 ± 0.2 cm^{-1} GPa^{-1} determined by Knittle and Williams (1993).

More importantly, we found that the FWHM of the $\nu_3(SiO_4)$ zircon band does not change significantly with pressure. There is an indication for slight FWHM increase in the case of non- or mildly radiation-damaged zircon (i.e., synthetic $ZrSiO_4$, perhaps also M144), whereas the FWHM seems to decrease at elevated pressures in the case of strongly radiation-damaged samples (G168, OR1). Note that different trends for pressure increase and pressure release were not observed; samples yielded the same Raman parameters within analytical uncertainties before and after having been subjected to high pressures. This is in apparent contrast to the high-pressure study of Knittle and Williams (1993), who detected notable band broadening of zircon after their experiments. However, they applied much higher pressures up to 37 GPa, which seem to have caused some permanent structural damage. Further, our observations do not seem to be consistent with results of a recent study of Trachenko et al. (2007), who reported a final ~5% volume reduction of radiation-amorphized zircon after being compressed to 9 GPa and subsequent pressure release, and that a phase transformation had occurred in the 4.5–9 GPa range. The apparently different observations, however, may be due to the different materials, as Trachenko et al. (2007) studied fully amorphized $ZrSiO_4$, whereas our samples showed much lower levels of radiation damage.

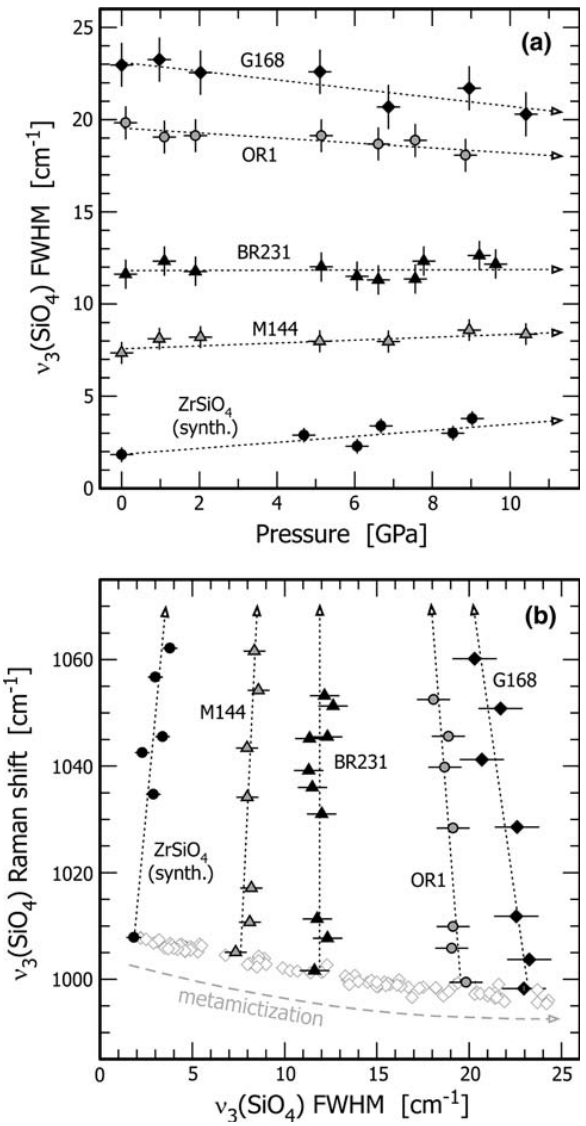

Fig. 2 Raman spectral changes of zircon as induced by pressure: **a** Plot of the width of the $\nu_3(SiO_4)$ Raman band against pressure, **b** Plot of the spectral position of this band against width. Trends of changes with pressure (*dotted lines are visual guides*) deviate significantly from the trend of spectral changes as caused by the accumulation of radiation damage (*gray square symbols and dashed arrow*)

The slight band broadening observed from synthetic $ZrSiO_4$ might perhaps be assigned to a potential effect of quasi-hydrostaticity as originating from the solid argon medium for pressures above 0.9 GPa. However, the reason of the slight FWHM decrease of G168 and OR1 still remains unclear. One possible explanation might be given by considering the different molar volumes and differential compressibilities of the radiation-damaged domains in comparison to the non-damaged host lattice. Assuming the amorphous domains to exhibit a large molar volume and a

smaller bulk modulus for volume compression, the volume strain at the interface between radiation-damaged areas and the host lattice must get reduced on increasing pressures due to smaller volume differences at higher pressures. Accordingly, the FWHM of any spectroscopic signal that is sensitive to strain must get reduced. Increasing non-hydrostaticity at quasi-hydrostatic conditions and this sort of volume–strain reduction at increasing pressure appear to be two competitive effects for the development of the FWHMs related to the radiation damage in zircon. Any consideration of pressure-induced recovery of the radiation damage appears unlikely, in view of the fact that FWHMs decreased non-permanently and recovered to initial values after pressure release. Reliable interpretation of the observed slight FWHM changes with pressure will require further studies. Such studies should also attempt to address the question as to which degree compressive strain acting on included zircon grains (most likely up to a few GPa, or below) might have affected their self-irradiation and, with that, the long-term processes of damage generation and recovery.

All FWHM changes of natural zircon samples, however, are mainly within errors. This is also demonstrated in Fig. 2b: accumulation of alpha-event damage results in substantial FWHM increase, accompanied by rather moderate down-shift of this band, whereas pressure increase results in considerably different trends of spectral changes. These observations suggest that the FWHM of the $\nu_3(SiO_4)$ Raman band is indicative of the degree of self-irradiation but insignificantly affected by pressure acting on the zircon.

This result has important implications. It has been speculated (Wang et al. 2006; Wanthanachaisaeng et al. 2006) as to which degree the radiation damage present in zircon inclusions in high-pressure metamorphic minerals can be evaluated based on FWHMs determined from in situ Raman measurements, or whether elevated pressure acting on inclusions needs to be considered as potential cause of further FWHM changes. The latter suspicion was based on the well-known fact that heterogeneous pressure release of high-pressure host-inclusion couples upon sample uplift may result in significant compressive strain (also referred to as "fossilized pressure" or "overpressure") acting on the inclusion, which may be as high as 2–3 GPa (Parkinson and Katayama 1999; Sobolev et al. 2000; Glinnemann et al. 2003). Our results suggest that such pressures have very minor effect on the widths of internal SiO_4 Raman modes. This makes it possible to estimate the degree of radiation damage from the FWHM of the $\nu_3(SiO_4)$ zircon band, almost independent from whether or not analyzed inclusions are affected by pressure. It is clear, however, that such estimates of the radiation damage of zircon inclusions will be affected with slightly higher uncertainty compared to analogous estimates for unstressed bulk samples. The only major restriction is that such estimates should not be made if strongly asymmetric Raman bands, or even overlapping pairs of bands, are observed (see above). The latter would be indicative for lattice strain due to strongly non-hydrostatic stress conditions, perhaps along with some strain gradient within the analyzed material volume, which is likely to result in apparently too broad bands. In contrast, broadened symmetric Raman bands are a reliable indicator of accumulated radiation damage in zircon.

This result will, for instance, allow gemmologists to use zircon inclusions in evaluating specimens with regard to the common practice of heat treatment to enhance color and clarity. It is well known that radiation damage in zircon is annealed after heat-treatment at 1,000–1,200°C partly or completely, depending on the degree of damage and the duration of the treatment (Zhang et al. 2000; Nasdala et al. 2002b). The detection of radiation damage in zircon inclusions, indicated by strong band broadening, therefore allows one to exclude any heat treatment above this temperature range.

Acknowledgments Zircon samples were kindly made available by J. M. Hanchar (synthetic $ZrSiO_4$), W. Hofmeister (M144), and A. K. Kennedy (BR231, OR1, G168). Thoughtful comments of M. Gaft and an anonymous reviewer are gratefully acknowledged. Partial funding of this research was provided by the European Commission, contract no. MEXC-CT-2005-024878, and the FWF Austrian Science Fund, grant P20028-N10.

References

Balan E, Neuville DR, Trocellier P, Fritsch E, Muller J-P, Calas G (2001) Metamictization and chemical durability of detrital zircon. Am Mineral 86:1025–1033

Dawson P, Hargreave MM, Wilkinson GF (1971) The vibrational spectrum of zircon ($ZrSiO_4$). J Phys C Solid State Phys 4:240–256. doi:10.1088/0022-3719/4/2/014

Ewing RC, Meldrum A, Wang LM, Weber WJ, Corrales LR (2003) Radiation effects in zircon. In: Hanchar JM, Hoskin PWO (eds) Zircon. Reviews in mineralogy and geochemistry, vol 41. Mineralogical Society of America, Washington DC, pp 387–425

Gaft M, Panczer G, Reisfeld R, Shinno I (2000) Laser-induced luminescence of rare-earth elements in natural zircon. J Alloys Com 300–301:267–274

Gaft M, Shinno I, Panczer G, Reisfeld R (2002) Laser-induced time-resolved spectroscopy of visible broad luminescence bands in zircon. Mineral Petrol 76:235–246. doi:10.1007/s007100200043

Glasmacher UA, Lang M, Keppler H, Langenhorst F, Neumann R, Schardt D, Trautmann C, Wagner GA (2006) Phase transitions in solids stimulated by simultaneous exposure to high pressure and relativistic heavy ions. Phys Rev Lett 96:195701-1–195071-4

Glinnemann J, Kusaka K, Harris JW (2003) Oriented graphite single-crystal inclusions in diamond. Z Kristallogr 218:733–739. doi:10.1524/zkri.218.11.733.20302

Hanchar JM, Finch RJ, Hoskin PWO, Watson EB, Cherniak DJ, Mariano AN (2001) Rare earth elements in synthetic zircon: part 1. Synthesis, and rare earth element and phosphorus doping. Am Mineral 86:667–680

Hoskin PWO, Black LP (2000) Metamorphic zircon formation by solid-state recrystallization of protolith igneous zircon. J Metamorph Geol 18:423–439. doi:10.1046/j.1525-1314.2000.00266.x

Knittle E, Williams Q (1993) High-pressure Raman spectroscopy of $ZrSiO_4$: observation of the zircon to scheelite transition at 300 K. Am Mineral 78:245–252

Lang M, Glasmacher UA, Neumann R, Schardt D, Trautmann C, Wagner GA (2005) Energy loss of 50-GeV uranium ions in natural diamond. Appl Phys A 80:691–694. doi:10.1007/s00339-004-3104-1

Lang M, Zhang F, Lian J, Trautmann C, Neumann R, Ewing RC (2008) Irradiation-induced stabilization of zircon ($ZrSiO_4$) at high pressure. Earth Planet Sci Lett 269:291–295. doi:10.1016/j.epsl.2008.02.027

Lide DR (2003) CRC handbook of chemistry and physics, 84th edn. CRC Press, Boca Raton

Mao HK, Xu J, Bell PM (1986) Calibration of the ruby pressure gauge to 800 kbar under quasi-hydrostatic conditions. J Geophys Res 91:4673–4676. doi:10.1029/JB091iB05p04673

Mazhenov NA, Murgorodskij AP, Lazarev AN (1979) Resonance-splitting of inner vibrational frequencies of heavy anions in zircon ($ZrSiO_4$) crystals. Inorg Mater 15:495–503 in Russian

Meldrum A, Zinkle SJ, Boatner LA, Ewing RC (1999) Amorphization, recrystallization, and phase decomposition in the ABO_4 orthosilicates. Phys Rev B 59:3981–3992. doi:10.1103/PhysRevB.59.3981

Miletich R, Allan DR, Kuhs WF (2000) High-pressure single-crystal techniques. In: Hazen RM, Downs RT (eds) High-temperature and high-pressure crystal chemistry. Reviews in mineralogy and geochemistry, vol 41. Mineralogical Society of America, Washington DC, pp 445–519

Nasdala L, Hanchar JM (2005) Comment on: application of Raman spectroscopy to distinguish metamorphic and igneous zircon (Xian et al., Anal Lett (2004) vol. 37, p. 119). Anal Lett 38:727–734

Nasdala L, Irmer G, Wolf D (1995) The degree of metamictization in zircons: a Raman spectroscopic study. Eur J Mineral 7:471–478

Nasdala L, Irmer G, Jonckheere R (2002a) Radiation damage ages: practical concept or impractical vision?—reply to two comments on "Metamictisation of natural zircon: Accumulation versus thermal annealing of radioactivity-induced damage", and further discussion. Contrib Mineral Petrol 143:758–765

Nasdala L, Lengauer CL, Hanchar JM, Kronz A, Wirth R, Blanc P et al (2002b) Annealing radiation damage and the recovery of cathodoluminescence. Chem Geol 191:121–140. doi:10.1016/S0009-2541(02)00152-3

Nasdala L, Reiners PW, Garver JI, Kennedy AK, Stern RA, Balan E et al (2004) Incomplete retention of radiation damage in zircon from Sri Lanka. Am Mineral 89:219–231

Nelson DF, Sturge MD (1965) Relation between absorption and emission in the region of the R lines of ruby. Phys Rev 137:A1117–A1130. doi:10.1103/PhysRev.137.A1117

Parkinson CD, Katayama I (1999) Present-day ultrahigh-pressure conditions of coesite inclusions in zircon and garnet: evidence from laser Raman microspectroscopy. Geology 27:979–982. doi:10.1130/0091-7613(1999)027≤0979:PDUPCO≥2.3.CO;2

Pidgeon RT, Nemchin AA, van Bronswijk W, Geisler T, Meyer C, Compston W et al (2007) Complex history of a zircon aggregate from lunar breccia 73235. Geochim Cosmochim Acta 71:1370–1381. doi:10.1016/j.gca.2006.11.021

Piermarini GJ, Block S, Barnett JD, Forman RA (1975) Calibration of the pressure dependence of the R_1 ruby fluorescence line to 195 kbar. J Appl Phys 46:2774–2780. doi:10.1063/1.321957

Powell RC (1967) Fluorescence studies of energy transfer between single and pair Cr^{3+} systems in Al_2O_3. Phys Rev 155:296–308. doi:10.1103/PhysRev.155.296

Rothamel U, Heber J, Grill W (1983) Vibronic sidebands in ruby. J Phys B Condens Matter 50:297–304. doi:10.1007/BF01470041

Sharma SK, Mao HK, Bell PM, Xu JA (1985) Measurement of stress in diamond anvils with micro-Raman spectroscopy. J Raman Spectrosc 16:350–352. doi:10.1002/jrs.1250160513

Sobolev NV, Fursenko BA, Goryainov SV, Shu JF, Hemley RJ, Mao HK et al (2000) Fossilized high pressure from the Earth's deep interior: the coesite-in-diamond barometer. Proc Natl Acad Sci USA 97:11875–11879. doi:10.1073/pnas.220408697

Syme RWG, Lockwood DJ, Kerr J (1977) Raman spectrum of synthetic zircon ($ZrSiO_4$) and thorite ($ThSiO_4$). J Phys C Solid State Phys 10:1335–1348. doi:10.1088/0022-3719/10/8/036

Trachenko K, Brazhkin VV, Tsiok OB, Dove MT, Salje EKH (2007) Pressure-induced structural transformation in radiation-amorphized zircon. Phys Rev Lett 98:135502-1–135502-4

Verma P, Abbi SC, Jain KP (1995) Raman-scattering probe of anharmonic effects in GaAs. Phys Rev B 51:16660–16667. doi:10.1103/PhysRevB.51.16660

Wang W, Scarratt K, Emmett J, Breeding C, Douthit T (2006) The effects of heat treatment on zircon inclusions in Madagascar sapphires. Gems Gemol 42:134–150

Wanthanachaisaeng B, Häger T, Hofmeister W, Nasdala L (2006) Raman- und fluoreszenz-spektroskopische Eigenschaften von Zirkon-Einschlüssen in chrom-haltigen Korunden aus Ilakaka und deren Veränderung durch Hitzebehandlung. Gemmologie 55:119–132

Wopenka B, Jolliff BL, Zinner E, Kremser DT (1996) Trace element zoning and incipient metamictization in a lunar zircon: application of three microprobe techniques. Am Mineral 81:902–912

Zhang M, Salje EKH, Capitani GC, Leroux H, Clark AM, Schlüter J et al (2000) Annealing of α-decay damage in zircon: a Raman spectroscopic study. J Phys Condens Matter 12:3131–3148. doi:10.1088/0953-8984/12/13/321

2.2 Metamict fergusonite–(Y) in a spessartine-bearing granitic pegmatite from Adamello, Italy

(2009)
Gieré, R., Williams, C.T., Wirth, R. & Ruschel, K.
Chemical Geology, 261:333–345

Chemical Geology 261 (2009) 333–345

Contents lists available at ScienceDirect

Chemical Geology

journal homepage: www.elsevier.com/locate/chemgeo

Metamict fergusonite-(Y) in a spessartine-bearing granitic pegmatite from Adamello, Italy

Reto Gieré [a,*], C. Terry Williams [b], Richard Wirth [c], Katja Ruschel [d]

[a] Mineralogisch-Geochemisches Institut, Albert-Ludwigs-Universität, Albertstrasse 23b, 79104 Freiburg, Germany
[b] Department of Mineralogy, The Natural History Museum, Cromwell Road, London, SW7 5BD, Great Britain, United Kingdom
[c] GeoForschungsZentrum Potsdam, Section 4.1, Telegrafenberg C120, 14473 Potsdam, Germany
[d] Institut für Mineralogie und Kristallographie, Universität Wien, Althanstrasse 14, 1090 Wien, Austria

ARTICLE INFO

Article history:
Accepted 28 May 2008

Keywords:
Fergusonite-(Y)
Metamict
Amorphous
Pyrophanite
Uraninite
Nanopores
Helium bubble
Adamello

ABSTRACT

A granitic pegmatite associated with the Monte Bruffione granodiorite in the Tertiary Adamello Massif, Italy, consists primarily of albite, potassium feldspar, muscovite, quartz, and spessartine (graphic intergrowths with quartz). As accessory minerals, the pegmatite contains magnetite, pyrophanite, monazite-(Ce), uraninite, xenotime-(Y), zircon, and fergusonite-(Y). This yttrium niobate mineral contains inclusions of Th-rich uraninite, and is itself rich in UO_2 (average 7.1 ± 1.1 wt.%, $n = 34$) and ThO_2 (average 3.5 ± 1.0 wt.%). Many fergusonite crystals display growth zoning, characterized by a general increase towards the rim in the contents of Y and rare earth elements at the expense of U and Th. Irregular or patchy zoning as well as sector zoning are also observed in some of the crystals. Due to the alpha-decay of the U and Th fergusonite is metamict, as documented by transmission electron microscopy (TEM) and micro-Raman spectroscopy. Nevertheless, the mineral could be identified as fergusonite-(Y) on the basis of a canonical discriminant analysis of its chemical composition and on the basis of the close similarity of its Raman spectrum with that of a reference β-fergusonite. The crystalline-to-metamict transformation was associated with macroscopic swelling, as indicated by microfractures that are arranged radially around fergusonite inclusions in pyrophanite. The TEM data revealed that the amorphous fergusonite contains U-rich nanocrystals (5–15 nm across), which in most cases are distributed randomly and which probably nucleated after metamictization. The TEM investigations further revealed the ubiquitous presence of nano-sized (typically 5–25 nm across), nearly circular features, which exhibit a low diffraction contrast and which we interpret as nanopores. We propose that these nanopores represent former bubbles of radiogenic helium. The data presented here allowed us to determine that the critical amorphization dose of fergusonite is $\leq 0.97 \times 10^{16}$ alphas/mg, i.e., lower than that of other actinide-rich oxide minerals (e.g., pyrochlore). The presence of the U-rich nanocrystals indicates that fergusonite is able to retain actinides even when it is entirely metamict and even if it is surrounded by microfractures, which represent potential fluid pathways. This result suggests that fergusonite could be a phase suitable to be included in ceramics designed for the immobilization of high-level nuclear waste.

1. Introduction

Fergusonite, ideally $YNbO_4$, was first reported by Haidinger (1826) as a new mineral species, associated with quartz from Kikertaursak, near Cape Farewell, South Greenland. The report is purely descriptive and based on crystal morphology. A chemical analysis of this material was given by Hartwell (1828), and with the assumption that the ZrO_2 reported is from an included Zr-phase, the analysis yields a stoichiometry of $Y_{1.06}Nb_{0.95}O_4$, i.e., remarkably close to ideal $YNbO_4$. Fergusonite occurs as an accessory mineral in granitic pegmatites, mostly in rare earth element (REE)-enriched pegmatites (Ervanne, 2004; Ercit, 2005), and often in combination with one or more Y, Th, Nb, Ta, Ti oxide accessory minerals (Lumpkin, 1998). Among other reported occurrences, fergusonite has also been described as a hydrothermal mineral from the Pilansberg nepheline syenite (Olivo and Williams-Jones, 1999). Recently, fergusonite has been discovered in a porphyritic biotite granite of the Xihuashan complex, Southern China, where it occurs as discrete crystals and as inclusions in Y-bearing spessartine, in both cases associated with uraninite (Wang et al., 2003).

Two structures have been reported for fergusonite: a scheelite-type tetragonal fergusonite (α-fergusonite, $I4_1/a$); and at high temperatures, a monoclinic polymorph (β-fergusonite, I2/c) (see recent review by Tomašić et al., 2006). Fergusonite can, however,

* Corresponding author. Tel.: +49 761 203 6409; fax: +49 761 203 6407.
E-mail address: giere@uni-freiburg.de (R. Gieré).

0009-2541/$ – see front matter © 2008 Elsevier B.V. All rights reserved.
doi:10.1016/j.chemgeo.2008.05.017

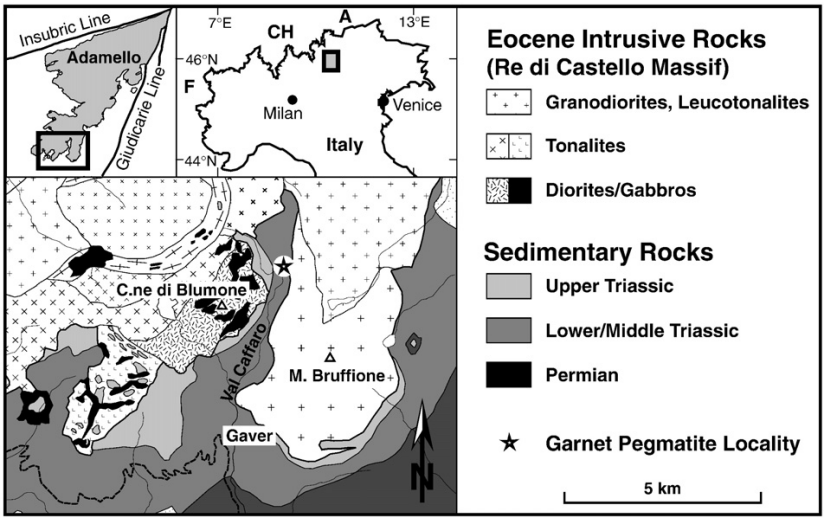

Fig. 1. Tectonic map of the southern Adamello region, Italy. Modified after Zhang et al. (2001).

contain significant quantities of U and Th, and thus is commonly metamict (Ervanne, 2004; Tomašić et al., 2006; Ruschel et al., 2007). Therefore, the structure is usually established only after heating the metamict mineral, provided that sufficient material is available. Structural characterization after annealing metamict minerals, however, can lead to a mis-identification; for example, in a systematic study of samarskite (Warner and Ewing, 1993), one of the 19 samarskite samples annealed recrystallized with a fergusonite structure. Additionally, for crystals less than 100 μm in size, this procedure is not technically feasible and therefore, identification requires to be founded on chemical composition. A recent study by Ercit (2005), based on statistical analyses of chemical compositions, provides the best opportunity to distinguish fergusonite from a range of (Y,REE,U,Th)–(Nb,Ta,Ti) oxide accessory minerals commonly associated with REE-enriched granitic pegmatites.

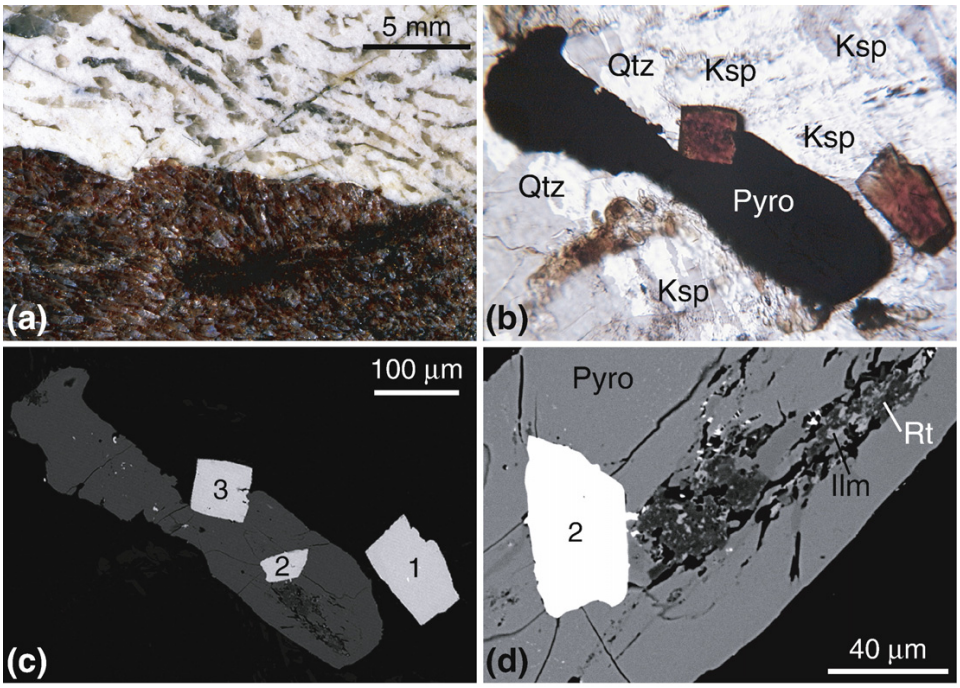

Fig. 2. Hand specimen and thin section images of the garnet-bearing granitic pegmatite from Val Caffaro, Adamello (Italy). (a) Polished slab of sample 269a. (b) Photomicrograph of Adamello thin section AU18B (plane polarized light), showing two brown fergusonite-(Y) grains (crystals #1 and #3) together with pyrophanite (opaque), potassium feldspar, and quartz. (c) BSE image of the area displayed in (b) revealing an additional fergusonite-(Y) grain (crystal #2) as well as many tiny fergusonite crystals (white blebs in left part of the pyrophanite crystal) as inclusions in pyrophanite. (d) Detail of (c) showing radial cracks in pyrophanite around fergusonite crystal #2. The small bright spots are fergusonite-(Y) inclusions in pyrophanite, whereas the fine-grained assemblage in the center of the image consists of rutile (darker than pyrophanite) and ilmenite (brighter than pyrophanite). Numbers refer to crystal numbers. *Abbreviations*: Ksp = potassium feldspar; Pyro = pyrophanite; Qtz = quartz; Rt = rutile; Ilm = ilmenite.

The aim of the present investigation is to report petrographic, compositional, and structural data for an actinide-bearing yttrium niobate accessory mineral in a spessartine-bearing granitic pegmatite from Adamello, Italy. This mineral was originally observed during a detailed investigation of garnet–quartz intergrowths in pegmatites (Zhang et al., 2001), and was tentatively identified as yttrocolumbite-(Y). Here, we reinvestigate this sample using a combination of compositional and structural techniques. The small grain size (typically less than 100 μm) precluded the employment of traditional bulk sample X-ray diffraction (XRD) techniques to determine structure. Therefore, microbeam XRD, micro-Raman spectroscopy, and transmission electron microscopy (TEM) were used to attempt structural characterization. The results show the mineral to be metamict, and it is identified as fergusonite-(Y) on the basis of its Raman characteristics as well as its chemical composition when the statistical approach of Ercit (2005) is used.

The compositional variations and the micro- and nano-textures observed in this study provide information on changes to fluid and/or melt composition during growth of fergusonite, and its response to the effects of radioactive decay of the actinide elements present. Additionally, observations from the TEM study provide new information into the effects of metamictization.

2. Geologic setting

The Tertiary Adamello Massif is composed of several major granitoid plutons and numerous subsidiary mafic intrusions (Bianchi et al., 1970; Brack, 1984; Callegari, 1985). These plutons were intruded into schists and gneisses of the Southern Alpine basement and their Permian and Mesozoic sedimentary cover (Fig. 1). Del Moro et al. (1985) documented a systematic progression of emplacement cooling ages from the oldest plutons in the South (42 Ma) to the youngest plutons in the North (29 Ma). The Adamello massif shows many of the characteristic features of calc-alkaline Cordilleran intrusions, which are dominated by hornblende-biotite-bearing metaluminous tonalites and granodiorites (Brack, 1984, 1985; Ulmer et al., 1985; Kagami et al., 1991). The southernmost and oldest pluton (Callegari and Dal Piaz, 1973; Hansmann and Oberli, 1991), the Re di Castello massif, forms itself a composite intrusion of predominantly gabbroic, tonalitic, and granodioritic rocks, and is bordered by small mafic and ultramafic bodies (Blundy and Sparks, 1992; Ulmer et al., 1985). At the time of emplacement of the southern Adamello batholith, the confining pressure was 2–3 kbar (Riklin, 1985; and unpublished data from L. Matile, pers. communication).

The data presented here were obtained from a sample (AU18) of a garnet-bearing granitic pegmatite dike. This dike occurs in an outcrop located approximately 250 m to the East of Casinetto di Blumone, Alta Val Caffaro (Fig. 1; Italian coordinate grid: 614.630/5090.950, corresponding to a longitude of 10°28′45″ E and a latitude of 45°57′43″ N; 2340 m above sea level). At the locality sampled, the pegmatite has a distinct appearance because of the presence of garnet–quartz intergrowths, which form nodules several centimeters across and which have been previously described (Zhang et al., 2001). The dike originates in the Monte Bruffione granodiorite (Fig. 1), gradually changes into a pegmatite containing quartz, alkali feldspar, albite and some biotite, and finally becomes a biotite-free rock. This biotite-free pegmatite crosscuts the Calcare di Angolo formation, a characteristic sequence of metamorphosed, alternating limestones and marls of

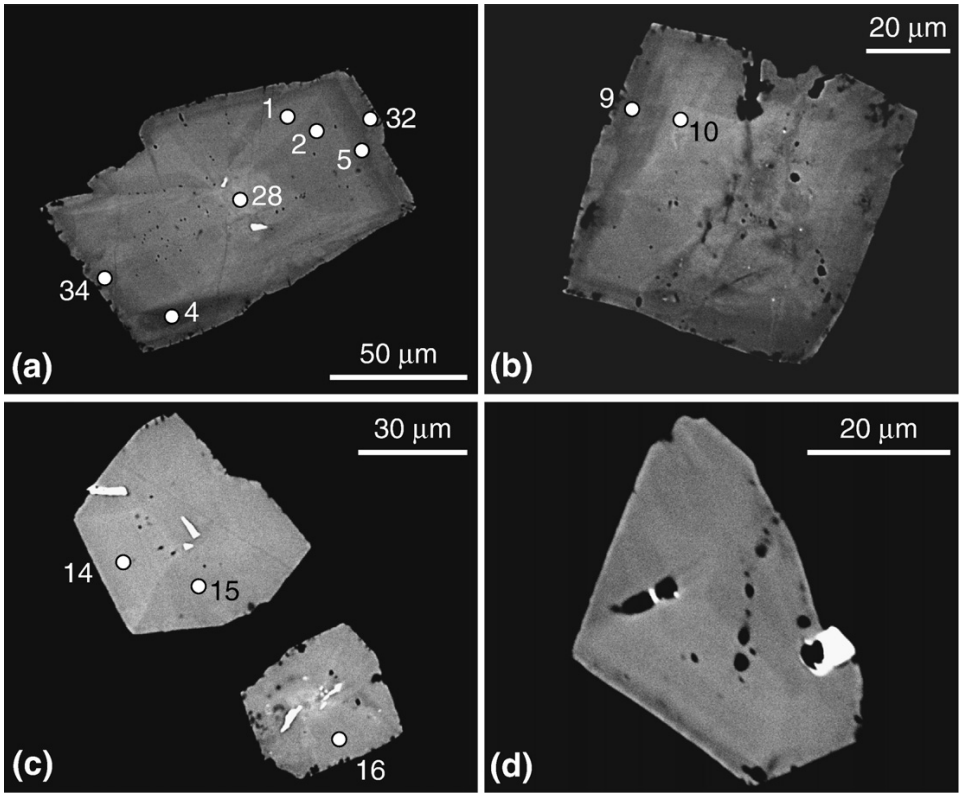

Fig. 3. BSE images of fergusonite-(Y) crystals from sample AU18B. (a) Crystal #1 (see Fig. 2c), displaying sector and growth zoning, small holes (black), and two uraninite inclusions (bright). (b) Crystal #3 (see Fig. 2c), displaying growth zoning with a bright core area surrounded by a lower-contrast rim. (c) Crystals #5 (left) and #6, both containing uraninite inclusions and displaying characteristic round to elliptic holes. Note sector zoning in crystal #5. (d) Crystal #12, with uraninite inclusions and holes. Numbers (next to white dots) refer to analysis numbers in Table 2.

Middle Triassic age. The most recent age obtained for the Bruffione granodiorite is 40.4 ± 0.2 Ma (J. Hanchar, pers. communication), which is in good agreement with earlier ages (Del Moro et al., 1985; Hansmann and Oberli, 1991).

3. Analytical techniques

The fergusonite-(Y) crystals and associated minerals were first characterized and imaged in back-scattered electron (BSE) mode with a JEOL JSM-5900LV analytical scanning electron microscope at the Natural History Museum, London. Quantitative electron probe microanalyses (EPMA) were done at the Department of Mineralogy of the Natural History Museum, London using a CAMECA SX-50 equipped with four wavelength-dispersive crystal spectrometers. Conditions used were 20 kV accelerating voltage, with a beam current of 25 nA, measured on a Faraday cup, and a beam diameter of approximately 1 μm. The thin section studied (AU18B) and standards were coated with 20 nm of carbon. Standards used were a combination of synthetic and natural materials. The counting time on the peak was typically 20 s for major elements, and 30 s for minor elements. Counting time on the background positions on either side of the peak was typically half of that on the corresponding peak. Where appropriate, only one side of the background was counted and an experimentally determined slope was adopted to calculate the background on the other side. Care was taken to ensure that the backgrounds were located in positions free of spectral interferences, particularly for determination of the REEs. The raw data were corrected using the PAP correction procedure (Pouchou and Pichoir, 1984). Inter-element interferences were corrected by applying experimentally determined correction factors. The element distribution maps were obtained on a CAMECA SX100 electron microprobe at the Department of Mineralogy of the Natural History Museum, London. All maps were acquired at 15 kV and 60 nA.

The focused ion beam (FIB) technique was used to cut a foil suitable for subsequent TEM investigations. The TEM foil was cut from fergusonite crystal #1 by sputtering it with Ga ions accelerated to 30 kV under ultrahigh-vacuum conditions in an FEI FIB200 instrument at GeoForschungsZentrum (GFZ), Potsdam (for details, see Wirth, 2004). The TEM foil was protected from abrasion by the Ga ion beam via a 1 μm thick Pt layer. The cuts were made perpendicular to the surface of the carbon-coated thin section and yielded a TEM-ready foil of ~15 × 10 × 0.15 μm, which was then placed onto a lacy carbon Cu grid.

The TEM investigations were carried out with the FEI Tecnai F20 X-Twin instrument at GFZ Potsdam, operating at 200 kV. The instrument is equipped with a high-angle annular dark-field (HAADF) detector, which is used in the scanning transmission electron microscopy (STEM) mode. This system enabled us to generate HAADF-STEM images; in such an image, the contrast strongly correlates with diffraction contrast and specimen thickness, and is proportional to the square of the atomic number Z (see, e.g., Utsunomiya and Ewing, 2003). The microscope is also equipped with an energy-dispersive X-ray (EDX) spectrometer, which allowed for the collection of EDX line-scans and EDX-STEM element distribution maps. To minimize drift, a drift-correction procedure was applied during the acquisition of EDX line-scans and elemental maps.

Raman microprobe analysis was done using an edge filter-based Renishaw RM 1000 spectroscopy system equipped with a Leica DMLM series optical microscope, a grating with 1200 grooves per millimeter, and a Si-based, Peltier-cooled charge-coupled device (CCD) detector. Spectra were excited with the Ar^+ 488.0 nm line. The laser power was 8 mW (measured behind the objective), which was low enough to avoid any local sample heating due to absorption of the laser light. A Leica 50x objective (numerical aperture 0.75) was used. Quasi-confocal measurements were carried out with an estimated lateral resolution of 4–5 μm. Spectra were obtained in the so-called "continuous extended scan" data collection mode (Nasdala and Massonne, 2000). The wavenumber accuracy was better than 1 cm^{-1}, and the spectral resolution was ~2.5 cm^{-1}.

4. Petrographic features

The granitic pegmatite contains as major phases plagioclase (albite), potassium feldspar (microperthite), muscovite, garnet (spessartine), and quartz (Zhang et al., 2001). Spessartine occurs as thin lamellae, which are intergrown with quartz in a regular fashion (Fig. 2a). Most of the individual garnet lamellae are compositionally zoned, whereby the highest spessartine contents (up to 78 mol%) are observed in the center. The garnet also contains relatively high amounts of Y_2O_3 (up to ~1.2 wt.%; average content 0.6 ± 0.3 wt.% Y_2O_3), and the distribution of Y is similar to that of Mn with concentrations decreasing from the center to the edges of the lamellae. Accessory minerals include magnetite, pyrophanite, uraninite, monazite-(Ce), xenotime-(Y), zircon, and the actinide-bearing yttrium niobate mineral fergusonite-(Y). Both monazite and xenotime are rare. Monazite-(Ce) occurs as sector-zoned crystals and is Th-rich (~15 wt.% ThO_2), whereas xenotime-(Y) is much poorer in Th and was observed only as small (3–5 μm across) inclusions in zircon. Zircon is present as subhedral crystals, which may be up to 50 μm across.

Fergusonite-(Y) exhibits a brown absorption color in transmitted light (Fig. 2b) and is isotropic when viewed with crossed polarizing filters. Its size ranges typically between 40 and 150 μm (Figs. 2, 3). Most crystals are subhedral to euhedral, but some display corroded grain boundaries (Fig. 3b, c). In many cases, the crystals are present as inclusions in potassium feldspar. Fergusonite-(Y), however, may also be in contact with, or enclosed by, pyrophanite. Within pyrophanite, it occurs either as large euhedral crystals or as tiny (0.5–4 μm across) rounded blebs (Fig. 2c, d). Pyrophanite may also contain fine-grained assemblages of ilmenite plus Nb–Fe-bearing rutile, in some places in association with fergusonite (Fig. 2d).

BSE images document that fergusonite-(Y) is not chemically homogeneous (Fig. 3). Many crystals display growth zoning, with a

Table 1
Average composition (EPMA data, $n = 34$) for fergusonite-(Y) in sample AU18B, standard deviation (1 sigma), minimum and maximum values.

	Mean	SD	Min.	Max.
SiO_2	0.1	0.1	<0.03	0.41
CaO	0.15	0.05	0.06	0.25
TiO_2	2.5	0.5	1.73	3.61
MnO	0.12	0.05	0.02	0.31
FeO	0.1	0.2	<0.04	0.85
Y_2O_3	25.2	0.9	23.3	27.6
Nb_2O_5	42.8	1	40.0	44.9
Ce_2O_3	0.34	0.06	0.23	0.50
Nd_2O_3	0.9	0.1	0.63	1.18
Sm_2O_3	1.0	0.1	0.79	1.24
Gd_2O_3	2.1	0.1	1.84	2.35
Tb_2O_3	0.42	0.06	0.27	0.55
Dy_2O_3	4.1	0.1	3.82	4.35
Ho_2O_3	0.93	0.09	0.77	1.13
Er_2O_3	3.0	0.1	2.81	3.41
Tm_2O_3	0.36	0.06	0.24	0.52
Yb_2O_3	3.0	0.5	2.54	4.93
Lu_2O_3	0.4	0.1	0.28	0.82
Ta_2O_5	1.1	0.3	0.61	2.06
PbO	0.17	0.07	<0.12	0.24
ThO_2	3.5	1.0	1.26	5.03
UO_2	7.1	1.1	5.04	9.70
Total	99.5		97.8	101.6
$Y_2O_3 + REE_2O_3$	42.0	1.3	39.4	45.3
$ThO_2 + UO_2$	10.6	1.9	6.5	14.2

Note: the following components were sought, but not found: Na_2O<0.03, MgO<0.02, Al_2O_3<0.02, La_2O_3<0.09 wt.%.

core that is brighter than the rim, which itself may consist of two separate zones (Fig. 3a, b). Irregular or patchy zoning as well as sector zoning are also observed in some of the crystals (Fig. 3), whereby these various types of zoning may be present in a single crystal (crystal #1, Fig. 3a). In many cases, fergusonite-(Y) contains inclusions of Th-bearing uraninite, which appear as bright grains in the BSE images and whose longest dimension ranges from 1 to 10 μm. The BSE images further reveal the presence in fergusonite of small, round to elliptical features (Fig. 3), which appear dark in the BSE images and which are depressions on the polished surface of the crystals. The diameter of these depressions ranges mostly between 0.4 and 1 μm, but occasionally reaches nearly 3 μm. The depressions are characteristic of the mineral in the sample studied.

5. Characterization by EPMA

EPMA data reveal that the mineral is composed predominantly of Y_2O_3 (~25 wt.%), REE_2O_3 (~17 wt.%), and Nb_2O_5 (~43 wt.%), with substantial amounts of TiO_2, Ta_2O_5, UO_2, and ThO_2 (Table 1). The analytical total of 99.5 wt.% for the mean of 34 analyses from 10 separate grains might point to the presence of water at low concentrations. A detailed assessment of the whole analytical dataset

Table 2
Selected EPMA data for fergusonite-(Y) crystals in sample AU18B.

Analysis #	1	2	4	5	28	32	34	9	10	14	15	16
SiO_2	0.02	0.06	<0.03	<0.03	0.41	0.32	0.06	0.13	0.12	0.08	0.06	0.20
CaO	0.22	0.24	0.11	0.17	0.20	0.16	0.06	0.18	0.17	0.16	0.13	0.19
TiO_2	2.61	2.49	2.12	2.31	3.61	2.02	1.73	2.20	3.37	3.08	2.52	2.35
MnO	0.17	0.12	0.13	0.08	0.08	0.06	0.12	0.11	0.11	0.11	0.02	0.11
FeO	0.04	0.07	0.15	0.04	<0.04	<0.04	<0.04	<0.04	0.13	0.07	<0.04	0.05
Y_2O_3	24.3	24.4	26.3	25.0	23.5	26.0	25.7	25.6	23.3	24.5	25.3	24.4
Nb_2O_5	42.6	42.5	44.5	43.6	40.8	44.5	44.5	43.7	40.8	41.8	42.7	42.8
Ce_2O_3	0.34	0.32	0.27	0.35	0.35	0.40	0.37	0.35	0.32	0.35	0.44	0.36
Nd_2O_3	1.05	1.01	0.70	0.92	0.83	0.96	1.14	1.02	1.01	1.07	1.11	1.05
Sm_2O_3	1.05	1.03	0.93	0.96	0.98	1.24	1.15	1.10	1.05	1.00	1.08	1.07
Gd_2O_3	2.20	2.31	2.28	2.16	1.90	2.14	1.95	2.29	2.10	2.17	2.21	2.26
Tb_2O_3	0.47	0.55	0.43	0.35	0.48	0.38	0.43	0.40	0.43	0.34	0.51	0.48
Dy_2O_3	4.33	4.35	4.33	4.33	3.82	3.95	3.89	4.20	4.12	4.25	4.21	4.16
Ho_2O_3	0.94	0.96	0.89	1.11	0.83	0.82	0.96	0.86	0.88	1.13	0.97	0.94
Er_2O_3	2.94	3.12	3.24	2.90	3.02	3.21	3.39	3.07	2.87	2.93	3.00	2.94
Tm_2O_3	0.30	0.37	0.35	0.40	0.35	0.43	0.52	0.34	0.33	0.49	0.34	0.31
Yb_2O_3	2.71	2.72	3.08	2.69	2.90	3.78	4.93	2.90	2.74	2.86	2.65	2.71
Lu_2O_3	0.28	0.42	0.54	0.35	0.39	0.44	0.82	0.39	0.41	0.45	0.44	0.32
Ta_2O_5	0.61	0.74	1.01	1.14	0.76	1.64	2.06	1.17	0.91	1.06	0.93	0.76
PbO	<0.12	<0.12	<0.12	<0.12	<0.12	0.23	0.24	<0.12	<0.12	<0.12	<0.12	<0.12
ThO_2	4.91	4.19	1.91	3.50	4.62	2.40	1.26	3.39	4.75	3.50	3.69	4.44
UO_2	7.23	7.23	6.41	6.91	9.58	6.14	5.23	6.84	9.05	8.61	7.36	7.04
Total	99.3	99.2	99.7	99.4	99.6	101.2	100.6	100.3	98.9	100.0	99.6	98.9
$Y_2O_3 + REE_2O_3$	40.88	41.57	43.33	41.57	39.38	43.74	45.30	42.53	39.54	41.51	42.25	40.98
ThO_2+UO_2	12.13	11.42	8.33	10.41	14.20	8.54	6.49	10.24	13.80	12.11	11.05	11.48
Number of cations normalized to 4 oxygens												
Si	0.001	0.003			0.019	0.015	0.003	0.006	0.006	0.004	0.003	0.009
Ca	0.011	0.012	0.005	0.008	0.010	0.008	0.003	0.009	0.009	0.008	0.007	0.009
Ti	0.091	0.087	0.073	0.080	0.126	0.069	0.059	0.076	0.119	0.107	0.088	0.082
Mn	0.007	0.005	0.005	0.003	0.003	0.002	0.005	0.004	0.004	0.004	0.001	0.004
Fe	0.002	0.003	0.006	0.002					0.005	0.003	0.001	0.002
Y	0.602	0.606	0.639	0.616	0.582	0.625	0.626	0.625	0.583	0.604	0.624	0.605
Nb	0.897	0.896	0.920	0.912	0.858	0.908	0.919	0.906	0.867	0.876	0.894	0.901
Ce	0.006	0.005	0.004	0.006	0.006	0.007	0.006	0.006	0.005	0.006	0.007	0.006
Nd	0.017	0.017	0.011	0.015	0.014	0.016	0.019	0.017	0.017	0.018	0.018	0.018
Sm	0.017	0.017	0.015	0.015	0.016	0.019	0.018	0.017	0.017	0.016	0.017	0.017
Gd	0.034	0.036	0.034	0.033	0.029	0.032	0.029	0.035	0.033	0.033	0.034	0.035
Tb	0.007	0.008	0.007	0.005	0.007	0.006	0.006	0.006	0.007	0.005	0.008	0.007
Dy	0.065	0.065	0.064	0.065	0.057	0.058	0.057	0.062	0.062	0.064	0.063	0.063
Ho	0.014	0.014	0.013	0.016	0.012	0.012	0.014	0.012	0.013	0.017	0.014	0.014
Er	0.043	0.046	0.047	0.042	0.044	0.046	0.049	0.044	0.042	0.043	0.044	0.043
Tm	0.004	0.005	0.005	0.006	0.005	0.006	0.007	0.005	0.005	0.007	0.005	0.005
Yb	0.038	0.039	0.043	0.038	0.041	0.052	0.069	0.040	0.039	0.040	0.038	0.039
Lu	0.004	0.006	0.007	0.005	0.005	0.006	0.011	0.005	0.006	0.006	0.006	0.004
Ta	0.008	0.009	0.013	0.014	0.010	0.020	0.026	0.015	0.012	0.013	0.012	0.010
Pb						0.003	0.003					
Th	0.052	0.045	0.020	0.037	0.049	0.025	0.013	0.035	0.051	0.037	0.039	0.047
U	0.075	0.075	0.065	0.071	0.099	0.062	0.053	0.070	0.095	0.089	0.076	0.073
Total cations	1.996	1.999	1.996	1.990	1.995	1.995	1.997	1.995	1.996	2.000	1.997	1.994
Y + REE	0.852	0.864	0.889	0.863	0.820	0.884	0.913	0.875	0.829	0.858	0.878	0.855
Th + U	0.127	0.120	0.085	0.108	0.148	0.086	0.066	0.105	0.145	0.126	0.115	0.120
Total A-site	0.979	0.984	0.975	0.970	0.968	0.970	0.980	0.980	0.975	0.984	0.993	0.976
Other cations	1.017	1.015	1.021	1.020	1.027	1.025	1.018	1.015	1.021	1.016	1.004	1.018

All analyses are single-spots, and their locations are shown in Fig. 3.
Note: the following components were sought, but not found: Na_2O<0.03, MgO<0.02, Al_2O_3<0.02, La_2O_3<0.09 wt.%.

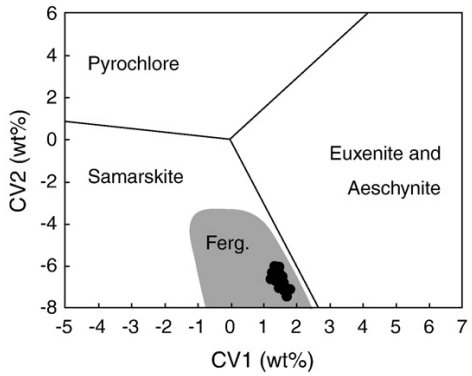

Fig. 4. Plot of the composition of the Adamello fergusonite-(Y) in the classification diagram of Ercit (2005). CV1 and CV2 are the canonical variables 1 and 2 of Ercit's three-group model chemical discriminant analysis.

and corresponding analysis positions on each grain indicated a more complex picture. No significant correlations were observed between specific element concentrations and analytical totals, implying no systematic analytical errors were present. However, there appears to be a correlation between analytical total and textural appearance of individual grains. Of the 10 grains analyzed, 3 had analytical totals close to 100 wt.% (99.81 wt.%, 99.82 wt.% and 99.89 wt.%). In BSE images, these grains appeared to be relatively unaltered, i.e., embayment textures were minimal (Fig. 3a and c, upper grain). In contrast, 6 grains had analytical totals significantly less than 100 wt.% (averaging 99.06 ± 0.11), and these grains displayed more corroded grain boundaries than those with higher analytical totals (Fig. 3b and c, lower grain). These observations indicate that water may indeed be present, and that its presence is a function of variable alteration. The tenth grain had a high analytical total (100.41 wt.%, average of 3 analyses) but the average values for FeO for this grain (0.19 wt.%) is significantly higher than the mean of the other 31 analyses (0.09 wt.%). For this grain, these data strongly suggest a sub-micrometer intergrowth between fergusonite-(Y) and an Fe-bearing phase.

The calculated cation:oxygen molar ratios of all crystals analyzed are close to 1:2 (Table 2). If Y and the REE are grouped with Th and U as A-site cations, and Nb, Ta, Ti, and Si as B-site cations, the ratio of group-A cations to group-B cations is nearly 1:1, consistent with an ABO_4 stoichiometry. Using the statistical approach of Ercit (2005) indicates that, based on its chemical composition, the mineral belongs to the fergusonite group (Fig. 4).

The A-site is predominantly populated by Y + REE, with relatively minor amounts of U and Th (Fig. 5a). The B-site composition also forms a tight cluster, near the Nb corner in the Ti–Nb–Ta ternary diagram (Fig. 5b). These figures illustrate that the compositional range is fairly limited. Of the main components, TiO_2, Ta_2O_5, ThO_2 and UO_2

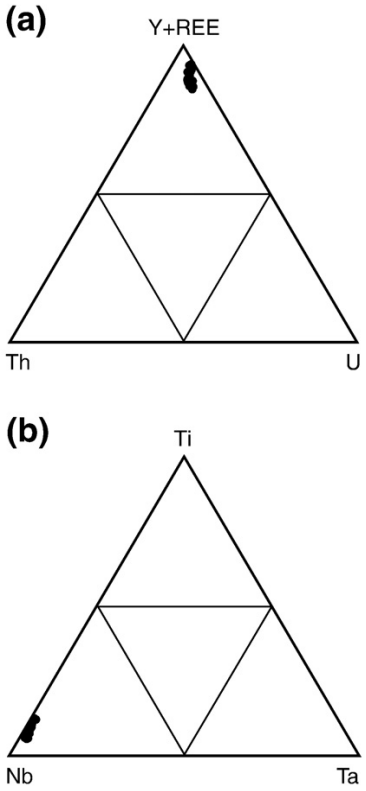

Fig. 5. Ternary diagrams (in mol%) showing the compositional variation in the Adamello fergusonite. (a) A-site composition. (b) B-site composition.

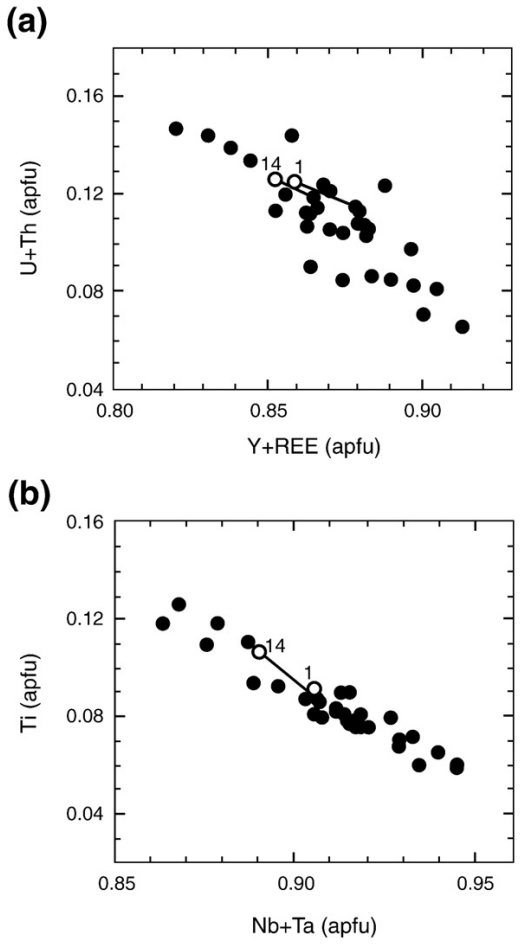

Fig. 6. Variation diagrams for the Adamello fergusonite-(Y). (a) U + Th *vs.* Y+REE. (b) Ti *vs.* Nb + Ta. Open symbols show analyses in the sectors appearing bright in BSE images (numbers correspond to those listed in Table 2). These sectors are enriched in both U + Th and Ti relative to the corresponding darker sectors (connected by tie-lines). The analysis locations of the two sector pairs are shown in Fig. 3. Error bars are smaller than symbols.

show the largest variations (Table 1), but their ranges are <0.1 atoms per formula unit (apfu).

The compositional variation correlates with the zoning observed in BSE images and displays a systematic core-to-rim trend (Table 2). In general, the core areas are richer in Ti and U + Th, and poorer in Nb + Ta and Y + REE than the zones near the rims (Fig. 6). Similarly, the sectors appearing bright in BSE images (Fig. 3) are richer in Ti and U + Th than the corresponding darker sectors (Fig. 6, Table 2). These differences between various zones are illustrated for two different crystals as element distribution maps. Fig. 7 reveals that crystal #1 exhibits an U-rich core and a complex distribution of Ta in the rim areas, where Ta_2O_5 concentrations reach their highest levels (~ 2 wt.%, Table 2). Near the rim, Ta correlates antipathetically with Th and U, mimicking in detail the Th- and U-poor embayments at the left edge of the crystal as well as the Th- and U-poor outermost rim on the other sides of the crystal. The Th and U maps further display two inclusions of Th-rich uraninite, which is distinctly depleted in Y relative to the enclosing fergusonite. Inclusions of Th-rich uraninite are also seen in Fig. 8, which reveals that crystal #5 displays sector zoning. The sector appearing brighter in the BSE image (Figs. 3c, 8a) is enriched in Ti and U relative to the adjacent lower-Z sector, but there is little difference in the Th content of the two sectors, as also documented by analyses 14 and 15 (Table 2, Fig. 6).

The REE pattern of fergusonite-(Y) is characterized by a distinct HREE enrichment (Fig. 9), with HREE contents more than 100,000 times richer than those of chondrite values reported by Anders and Grevesse (1989). Lanthanum has not been detected in any of the analyses (Table 2). The shaded area in Fig. 9 represents σ_{n-1} of the mean of all 34 available fergusonite analyses. The analysis with the lowest concentrations of $Y_2O_3 + REE_2O_3$ (analysis #28) is from the core of crystal #1 and plots within the shaded range in Fig. 9, thus representing a typical composition. In contrast, the analysis with the highest contents of $Y_2O_3 + REE_2O_3$ (analysis #34), a rim analysis in the same crystal, is significantly enriched in all REE heavier than Er relative to the core analysis. The two highlighted analyses are at the same time those with the highest (core) and lowest (rim) contents of $UO_2 + ThO_2$ found during this study.

6. Characterization using TEM

The TEM investigation revealed that the FIB-prepared slice of fergusonite-(Y) crystal #1 is amorphous, as documented by the lack of bright spots in selected area electron diffraction patterns (SAEDP). Only the typical broad scattering intensity distribution of non-crystalline material is observed (2–3 rings are visible). This result is consistent with the Raman spectra (see below) as well as with the XRD patterns, which were obtained from two crystals (using a Bede microfocus source) and which lack peaks that could be assigned to fergusonite. Because the FIB-prepared slice of fergusonite had a thickness of ~ 150 nm, it was not possible to collect high-resolution images. However, HAADF-STEM imaging revealed the presence of two types of sub-micrometer-sized features, which are distinct in terms of their HAADF-STEM contrast and which were observed in all areas of the fergusonite foil that was studied.

6.1. Low-contrast spots

Most of these dark spots are sub-circular in shape and typically 5–25 nm across. These spots were observed either isolated in the fergusonite matrix or aligned along linear trends (Figs. 10a, 11). EDX analyses did not reveal any compositional differences between the dark spots and the matrix. Many trails of dark spots are parallel to each other, thus indicating a preferred alignment. Some of these trails are additionally characterized by a darker HAADF contrast than the

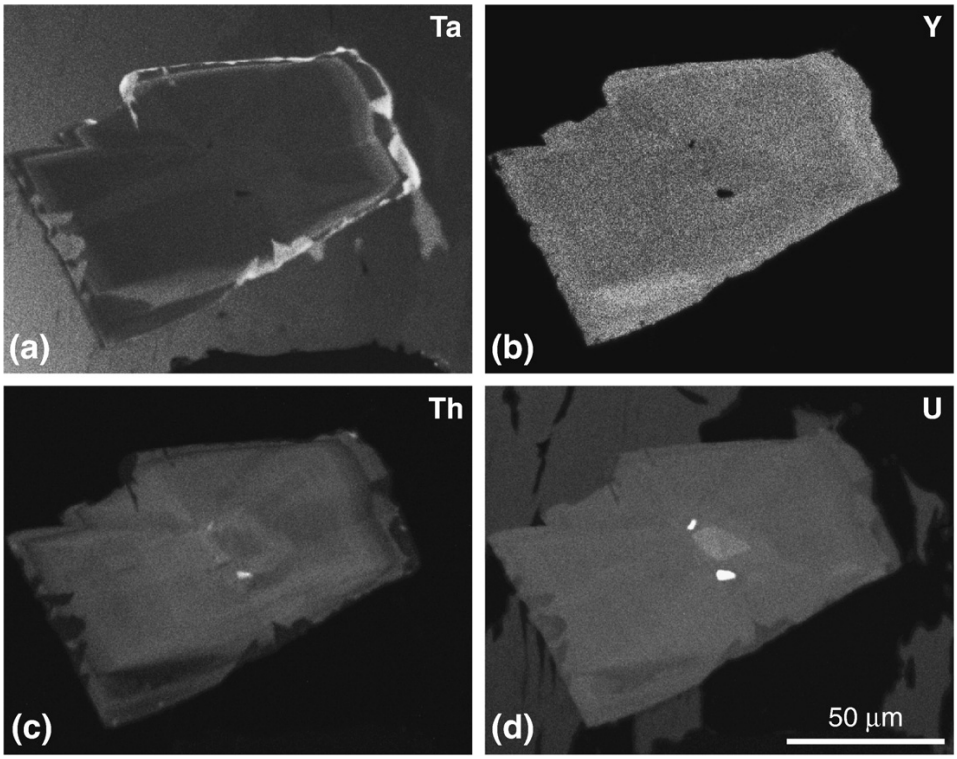

Fig. 7. X-ray maps showing the distribution of (a) Ta, (b) Y, (c) Th, and (d) U in crystal #1, which is displayed as BSE image in Fig. 3a. Quantitative EPMA data listed in Table 2.

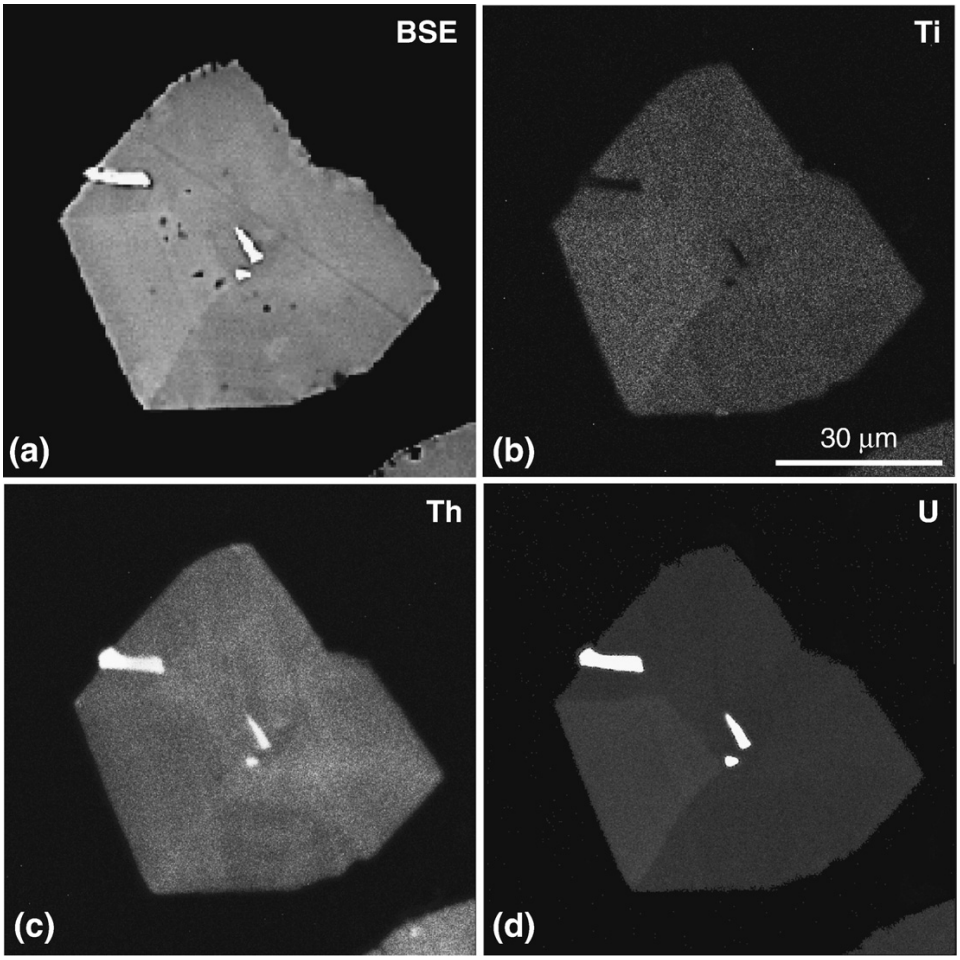

Fig. 8. BSE image (a) and X-ray maps showing the distribution of (b) Ti, (c) Th, and (d) U in crystal #5, which is also displayed as BSE image in Fig. 3c. Quantitative EPMA data listed in Table 2.

surrounding fergusonite matrix (Figs. 10a, 11). Other trails, however, are characterized by a HAADF contrast that is brighter than the surrounding fergusonite (Fig. 11). Element mapping in STEM mode revealed that the brighter areas around the dark spots are enriched in U and Th, and slightly depleted in Y relative to the surrounding matrix (Fig. 11).

In one area of the FIB section studied, numerous dark spots, some with larger diameters (90–130 nm across), form a cluster with an overall elliptical shape (Fig. 10a). This cluster measures approximately 1×1.5 μm in size, and thus has dimensions that are very similar to those of the depressions observed in BSE images (Fig. 3).

6.2. Bright-contrast nanoparticles

The HAADF-STEM images further document the presence of small, typically rounded particles, which are characterized by a markedly brighter contrast than the fergusonite matrix (Fig. 10b). These particles thus consist of relatively heavier elements than fergusonite. They are generally 5–15 nm across and distributed randomly throughout the matrix. In several areas of the section studied, however, these heavy-element nanoparticles occur accumulated along trails (Figs. 10b, 11) that are typically parallel to each other, and which in some cases intersect the trails of dark spots (Fig. 11).

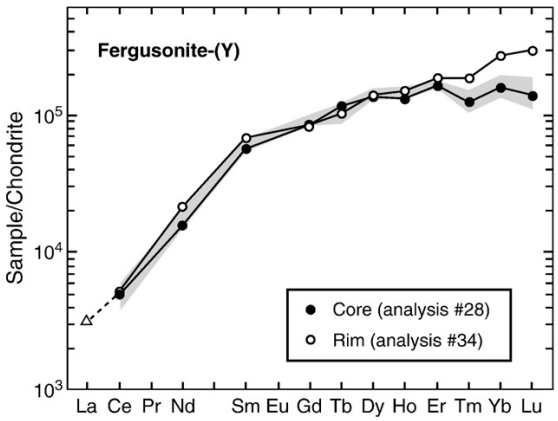

Fig. 9. Chondrite-normalized REE pattern for fergusonite-(Y) from Adamello, Italy. Shaded area represents the standard deviation (σ_{n-1}) of the average of all 34 analyses (data from Table 1). Core analysis (#28) is virtually identical to the average of all available EPMA data. Analyses #28 and #34 are both from crystal #1 (see Fig. 3a and text). Lanthanum concentrations are below EPMA detection limit, which is shown as triangle. Chondrite values are from Anders and Grevesse (1989).

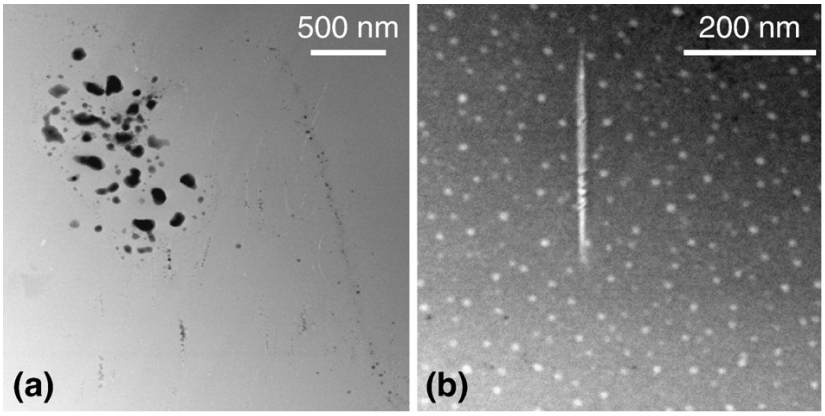

Fig. 10. HAADF-STEM images of fergusonite (FIB-prepared foil from crystal #1). a) Detail of area containing dark contrast spots, interpreted as nanopores. The nanopores are typically aligned in trails. Also shown is a cluster of nanopores with an overall shape of an ellipse, whose size is similar to the depressions seen in the BSE images (Figs. 2, 3). b) typical image showing the statistically distributed bright nanoparticles as well as one trail of nanoparticles (see also bright-field and dark-field TEM images in Fig. 13).

Because these trails consist of individual, very bright nanoparticles, they form prominent features in the HAADF-STEM images, that are different in appearance compared to the more diffuse, bright areas surrounding some of the trails of dark spots (Fig. 11). The individual nanoparticles are relatively enriched in U, but more depleted in O and Y than the surrounding matrix. These compositional differences are statistically significant, as documented by the EDX line-scans across the largest bright particle found (Fig. 12). Fig. 12 further shows that the nanoparticle is slightly enriched in Th and depleted in Ti relative to the matrix.

The nanoparticle trail seen in Fig. 10b is displayed as a bright-field TEM image in Fig. 13a, where it appears dark relative to the surrounding matrix. The bright-field image further shows the presence of some of the isolated U-rich nanoparticles in the vicinity of the trail. These isolated particles also appear darker than the matrix. The SAEDP obtained from this area shows a distinctive diffuse ring as well as two bright symmetric positioned spots. The presence of a diffuse ring ($d = 3.06$ Å) and of the two diffraction spots ($d = 1.98$ Å) indicates that the U-rich nanoparticles are crystalline. The diffraction pattern, however, did not allow us to identify the phase. An attempt to identify the U-rich nanocrystals using the Raman microprobe was also unsuccessful. The dark-field image shown in Fig. 13b was generated with a diffraction spot in the SAEDP (inset in Fig. 13a) and reveals the location of both the nanoparticle trail and the isolated particles in the matrix.

7. Characterization using micro-Raman spectroscopy

The Raman spectra of the Y–Nb oxide crystals from Adamello are very similar to reference spectra of a metamict fergusonite sample from Madagascar (Fig. 14). The same reference material from Madagascar yielded, after recrystallization through dry annealing at 1300 °C for 100 h, the XRD pattern of β-fergusonite (Ruschel et al., 2007). All spectra obtained for the Adamello fergusonite display a broad spectral pattern that is typical of highly damaged, nearly amorphized materials (for zircon shown by Nasdala et al., 2001), and they do not show remnants of Raman bands of crystalline fergusonite. From the striking similarity between the Raman spectra of the Adamello niobate and of the metamict fergusonite from Madagascar we conclude that the Adamello mineral is a strongly radiation-damaged, very probably "X-ray amorphous" fergusonite, consistent with the results obtained following the chemical characterization procedure of Ercit (2005).

8. Discussion

This study demonstrates that fergusonite, along with spessartine, is an important Y repository in the granitic pegmatite that was investigated. Fergusonite is more abundant that xenotime, and is present as relatively large crystals. Fergusonite has not been observed

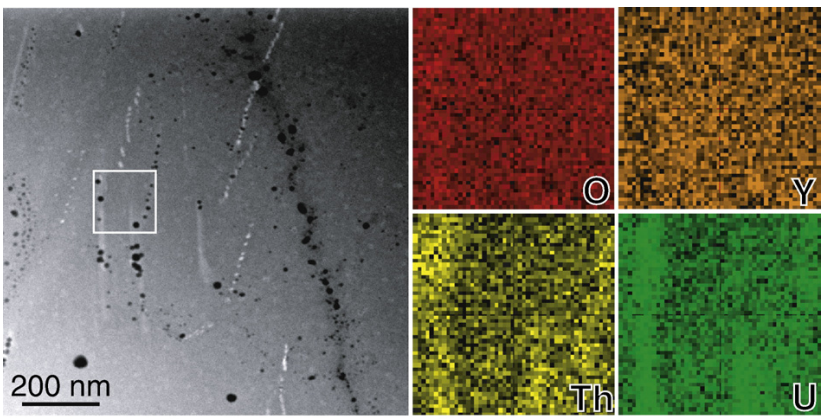

Fig. 11. The HAADF-STEM image on the left shows a typical view of fergusonite (crystal #1) with trails of nanoparticles and trails of nanopores as well as isolated nanopores. White box in HAADF-STEM image delineates area mapped by EDX; the maps reveal an enrichment in Th and U in the brighter areas surrounding the nanopores in HAADF-STEM image. Mapped area is 160 × 160 nm.

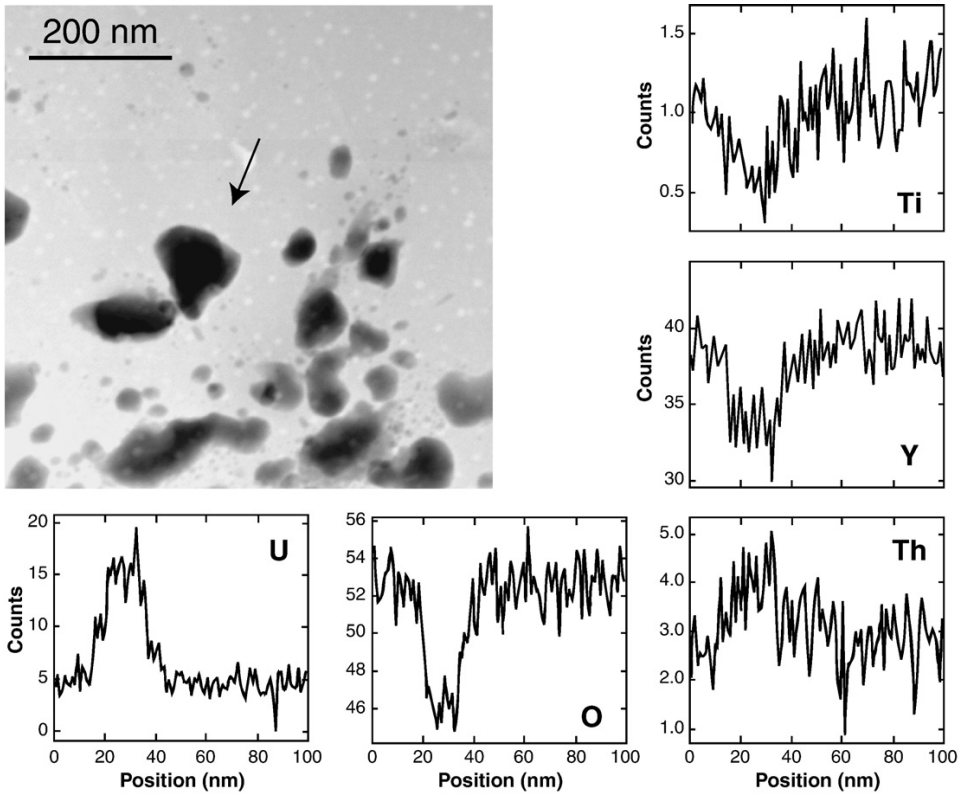

Fig. 12. HAADF-STEM image showing a detail of an area rich in dark spots (interpreted as nanopores) and bright spots. Black line (with arrow) across white nanoparticle shows profile trace for the line-scans, which show that the nanoparticle is enriched in U and, to a lesser extent, in Th, but depleted in O and Y relative to the surrounding fergusonite matrix.

within the garnet–quartz intergrowths nor as inclusions within garnet, and thus most likely started to crystallize later than spessartine. This conclusion is consistent with the decrease observed in the Y content from center to rim of individual garnet lamellae (Zhang et al., 2001). Spessartine also exhibits a pronounced decrease in the Mn concentration from the center to the rim of individual lamellae (Zhang et al., 2001). This decrease in Mn content probably reflects competition for Mn by the growth of pyrophanite. The occurrence of fergusonite as inclusions in pyrophanite (Fig. 2) suggests that fergusonite crystallization must have started before that of pyrophanite. We thus conclude that fergusonite crystallization took place between those of spessartine and pyrophanite.

The chemical zoning observed in fergusonite documents a general increase in Y+REE and a decrease in U + Th content towards the rim (Fig. 6). At the same time, the rim analysis in crystal #1 is significantly enriched in all REE heavier than Er relative to the core analysis, documenting fractionation towards heavier REE during crystal growth (Fig. 9).

Radioactive decay of the actinides and their daughter products is responsible for atomic-scale structural damage, which can transform a

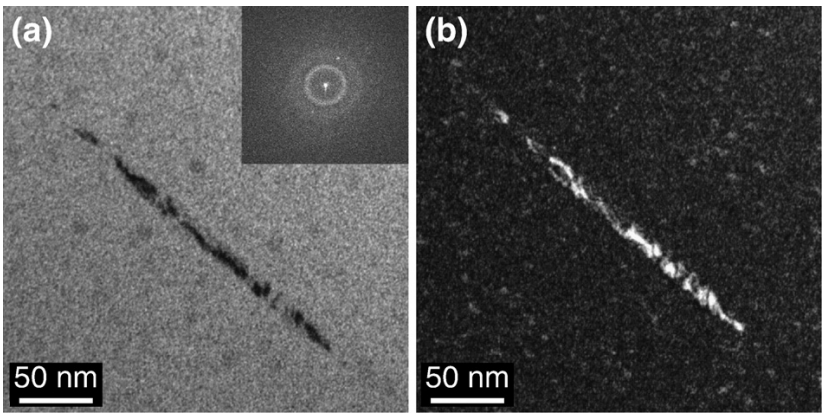

Fig. 13. High-magnification TEM images of the nanoparticle trail and the surrounding matrix shown in Fig. 10b. a) bright-field TEM image with selected area electron diffraction pattern (inset), b) dark-field TEM image, generated with the bright spot in upper right of the SAEDP inset in (a).

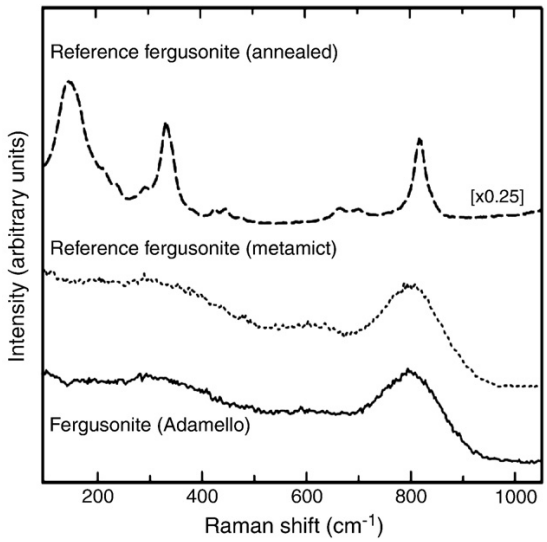

Fig. 14. Representative Raman spectrum of highly radiation-damaged fergusonite from Adamello (bottom; solid line) compared to a metamict reference fergusonite from Madagascar (dotted line) and the same reference material after annealing (dashed line).

mineral such as fergusonite from its crystalline to an amorphous, or metamict, state (Ewing et al., 1987; Ewing et al., 2000). This radiation-induced amorphization of crystalline compounds results from two simultaneous processes associated with the alpha-decay event (Ewing et al., 1988; Ewing et al., 1995): the ejected alpha-particles (He nuclei) dissipate most of their energy by ionization along their paths (range 10–20 μm), but near the end of their tracks they displace several hundred atoms, creating Frenkel defect pairs. The remaining alpha-recoil atom travels in the opposite direction and causes, along its track of 10–20 nm, collision cascades consisting of several thousand atomic displacements. These collision cascades, produced through the alpha-recoil nuclei, are the main cause of radiation-induced amorphization (Ewing et al., 2000). The transition from the crystalline to the metamict state is associated with changes in physical and chemical properties. Macroscopic swelling, for example, has been observed for various oxides and silicates, with volume increases of up to ~ 18% (Weber et al., 1998).

Fig. 2d shows that the fergusonite crystal is the point of origin of several distinct, radially arranged cracks in the enclosing pyrophanite. Such cracks are typically found around minerals that have undergone an increase in volume as a result of polymorphic transitions (e.g., coesite–quartz transition due to decompression, see Perrillat et al., 2003) or as a result of radiation-induced amorphization (e.g., Lumpkin, 2001; Lumpkin et al., 2004; Rajesh et al., 2006). As fergusonite contains substantial amounts of actinides (Tables 1, 2), we conclude that the radial cracks are the result of a volume increase associated with its transition from the crystalline to the metamict state. The TEM investigations clearly reveal that the fergusonite crystal #1 is entirely amorphous, as no electron diffraction spots were visible. Similarly, the Raman spectra of two separate crystals display the characteristics of amorphous materials (one shown in Fig. 14).

The alpha-decay dose of fergusonite can be calculated, assuming a closed system with respect to the daughter nuclides, from the Th and U contents determined by EPMA using the equation

$$D = 6N_{232}\left(e^{\lambda_{232}t} - 1\right) + 8N_{238}\left(e^{\lambda_{238}t} - 1\right) + 7N_{235}\left(e^{\lambda_{235}t} - 1\right) \quad (1)$$

where D is the dose in alphas/mg; t is the geologic age; N_{232}, N_{238} and N_{235} are the present number of atoms per milligram of ^{232}Th, ^{238}U and ^{235}U (using the present U composition of 99.275% ^{238}U and 0.72% ^{235}U); and λ_{232}, λ_{238} and λ_{235} are the respective decay constants (Murakami et al., 1991). Assuming an age of 40.4 Ma for the pegmatite formation, i.e., the same age as the Bruffione granodiorite (J. Hanchar, *pers. communication*), the calculation yields a cumulative dose of 0.92×10^{16} alphas/mg for the average fergusonite composition (Table 1). For analysis #28 (core of crystal #1), Eq. (1) yields a dose of 1.24×10^{16} alphas/mg, whereas for the analysis with the lowest content of UO_2 + ThO_2 (analysis #34), it yields a dose of 0.64×10^{16} alphas/mg. The FIB-prepared slice of fergusonite investigated by us corresponds to an area whose composition is represented by analysis #1 (Table 2). For this area, Eq. (1) yields a cumulative dose of 0.97×10^{16} alphas/mg. As our TEM observations for this area have shown it to be amorphous (see above), this result indicates that the critical amorphization dose for fergusonite, i.e., the alpha-dose above which the mineral is entirely amorphous, must be $\leq 0.97\times10^{16}$ alphas/mg. This dose compares with the critical dose of other actinide-bearing minerals (Lumpkin et al., 1994a, 1998; Lumpkin, 2001): the value for fergusonite may be higher than the critical amorphization dose for zircon ($\sim 0.4\times10^{16}$ alphas/mg) and similar to that of zirconolite ($\sim 0.9\times10^{16}$ alphas/mg), but it is lower than that of pyrochlore ($\sim 1.4\times10^{16}$ alphas/mg).

The amount of radiogenic PbO calculated from the average U and Th contents (Table 1) and the age of fergusonite is only 0.04 wt.%. This result documents that most of the average PbO content determined by EPMA (0.17 wt.%) is common Pb and thus was incorporated during crystal growth.

The EDX analyses did not reveal any compositional differences between the dark, predominantly round spots and the metamict fergusonite matrix in the HAADF-STEM images and therefore, we conclude that the spots are nanopores (ignoring the possible presence of a light element that is not detectable using EDX). We propose further that these rounded nanopores represent bubbles, which nucleated and grew as a result of the accumulation of radiogenic He. In a mineral that undergoes metamictization, capture of two electrons by the alpha-particles will result in the formation of He atoms. Helium will either be released at the surface of the mineral or it will accumulate in the mineral itself. In the latter case, He will be accommodated interstitially, trapped at internal defects, or aggregate to form bubbles (Ewing et al., 1995; Weber et al., 1998). Because He has a limited solubility in most minerals, at elevated concentrations it may form bubbles, which can cause swelling and affect many of the physical properties of the host phase (Weber et al., 1998). Helium concentrations of ~0.5 wt.% have been reported for natural uraninite and thorianite (Weber et al., 1998). In fergusonite, the presence of He has already been noted by Ramsay (1896) and Ramsay and Travers (1898), who also observed that He was released from the mineral upon heating. Assuming conversion of all alpha-particles into He, the average alpha-dose calculated for the Adamello fergusonite corresponds to ~0.006 wt.% He, with a range from 0.004 to 0.008 wt.% He. This He content is considerably lower than the 0.03 wt.% He measured by Ramsay and Travers (1898) for a Norwegian fergusonite that contains similar amounts of UO_2, but that sample is much older.

Even though we do not have direct chemical evidence for the near-spherical dark spots in the HAADF-STEM images being He bubbles, we suspect that they contain, or did contain at one time, radiogenic He. The presence of near-spherical microvoids, or bubbles, with diameters ranging from 100 to 400 nm has been observed in highly damaged natural zirconolite, where nucleation and growth of the bubbles have been attributed to the accumulation of He from the alpha-decay of U and Th after the mineral had become metamict (Ewing and Headley, 1983; Lumpkin et al., 1986). Bubbles assumed to contain He have also been reported for other metamict minerals (Lumpkin et al., 2000), including Nb-oxides like euxenite (Headley et al., 1981). Chkuaseli and Matzke (1993, 1995) concluded from their studies of irradiated uraninite that the evolution of fission gas bubbles comprises three stages, namely nucleation, growth, and mobility. They described that in uraninite the volatile fission products are transported to the grain boundaries, where the bubbles coalesce, eventually forming a network of interconnected

bubbles, from which the fission gases vent. A similar mechanism could be invoked for the formation of the trails of nanopores observed in the metamict fergusonite (Fig. 11). These trails, therefore, might represent former subgrain boundaries or defect-rich areas within the original fergusonite crystal. Coalescence of bubbles may also be the cause of the elliptical cluster of nanopores shown in Fig. 10a. Consequently, we conclude that the depressions visible in BSE images of all fergusonite crystals (Fig. 3) represent such clusters of nanopores, which formed through coalescence of He bubbles.

The U-rich nanocrystals (uraninite?) observed are for the most part distributed randomly within the metamict fergusonite matrix, but in several places occur aligned in trails (Figs. 10b, 11). We interpret these nanocrystals as having formed through spontaneous nucleation within the metamict fergusonite after its radiation-induced amorphization. These nanocrystals may have nucleated more easily along former subgrain boundaries or areas with high defect density and therefore occur as strings in some places. The diffuse U-rich areas around some of the nanopores (see maps in Fig. 11) may represent precursors to the nanocrystals. Occurrence of small inclusions of crystalline UO_2 (5–100 nm across) has been described previously in metamict brannerite (Lumpkin et al., 2000; Lumpkin, 2001). Crystallization of new minerals within metamict hosts has also been reported for other natural phases. Uranium-rich microlite from Alto Ligonha, Mozambique, for example, reacted with a low-temperature fluid during tropical weathering, leading to localized redistribution of radiogenic Pb and formation of plumbomicrolite near microcracks (Gieré et al., 2000, 2001). Similarly, altered areas of metamict zirconolite from Phalaborwa, South Africa, contain galena microcrystals, which must have been formed during interaction between the radiogenic Pb in the metamict host and a S-bearing fluid introduced along microcracks (Gieré et al., 1994; Lumpkin et al., 1994b). In the fergusonite studied, however, a fluid does not need to be invoked, since the U-rich nanocrystals appear to consist only of components that were originally present in fergusonite.

Interaction of the metamict fergusonite with a fluid, however, cannot be excluded. The radial cracks around fergusonite enclosed by pyrophanite (Fig. 2d) represent potential pathways for a fluid, which may have reacted with the metamict mineral. Even though the fergusonite from Adamello does not show signs of severe alteration in the BSE images (Fig. 3), there are three lines of evidence indicating that a fluid might have interacted with the metamict mineral:

1) The EPMA data include analytical totals that are in many cases lower than 100 wt.%, with an average of 99.5 wt.% (Table 1). This observation perhaps indicates that small amounts of water might be present. If water were indeed present, it appears that its concentration may be a function of the degree of alteration, as suggested by embayed grain boundaries of some crystals (Fig. 3). Metamict fergusonite can contain substantial amounts of water (Tomašić et al., 2006), as also known from other metamict minerals, especially when they have been altered (Lumpkin and Ewing, 1992, 1995, 1996; Lumpkin et al., 1999; Gieré et al., 2000, 2001; Lumpkin, 2001; Lumpkin et al., 2004).

2) Lead has not been detected in many of the EPMA analyses (Table 2), suggesting that Pb may have left the mineral in some areas of the metamict fergusonite. It should be noted, however, that the maximum PbO content observed (0.24 wt.%) is only two times the detection limit, suggesting that there are large uncertainties in the PbO values at these concentration levels.

3) Some of the nanopore trails are associated with a darker contrast in the HAADF-STEM images (Fig. 11), thus pointing to a possible removal of a heavy element, possibly Pb. These trails of nanopores could represent preferential fluid pathways through the metamict fergusonite.

Fergusonite appears to retain actinides even when it is entirely metamict, as indicated by the presence of the U-rich nanocrystals. This result suggests that fergusonite might be a phase suitable to be included in ceramics designed for the immobilization of high-level nuclear waste. To be a potential actinide host in nuclear waste ceramics, however, a phase should have additional characteristics: it should also (1) exhibit crystal chemical flexibility allowing to accommodate variations in waste composition; (2) be able to incorporate reasonably high waste loadings; (3) be highly durable in aqueous fluids; (4) possess acceptable physical and mechanical properties (e.g., radiation damage-induced swelling and cracking, thermal behavior, hardness); and (5) be producible using reliable and cost effective technology (Lumpkin et al., 2004). It is the overall balance of these characteristics that determines the suitability of a phase as candidate waste form. In the case of fergusonite, only a few of these five points can be addressed so far. We note that the phase can accommodate a wide variety of elements, including Gd (an important neutron absorber in waste forms). On the other hand, natural fergusonite accommodates relatively low amounts UO_2 and ThO_2 compared to other waste form phases (pyrochlore and zirconolite, see e.g., Lumpkin et al., 2004). Moreover, some alteration by late-stage fluids has been reported for fergusonite crystals occurring the Rutherford #2 granitic pegmatite, Virginia (Lumpkin, 1998). Therefore, additional experimental and natural analogue studies are needed to test the potential of fergusonite as a candidate nuclear waste form phase.

9. Conclusions

From the results obtained during this study we conclude that the Y–Nb–oxide in the Adamello pegmatite is metamict fergusonite-(Y). It started to crystallize from a granitic melt after spessartine, but before pyrophanite. Due to alpha-decay of the actinides present in the original fergusonite, the mineral has been transformed into an amorphous material. This crystalline-to-metamict transformation was associated with a considerable volume increase, as documented by microfractures that are arranged radially around fergusonite inclusions in pyrophanite. TEM data show that the amorphous fergusonite contains abundant inclusions of U-rich nanocrystals, which we interpret as products of nucleation after metamictization. We conclude further that the abundant, nearly circular dark features observed in HAADF-STEM images represent nanopores, which resulted from the accumulation of radiogenic He as bubbles.

Acknowledgments

The authors wish to thank Peter Ulmer for providing the sample and Peter Brack for providing the hand specimen picture of sample 269a (Fig. 2a). We thank Caroline Kirk for performing the micro-XRD analyses at the Natural History Museum in London. Katherine Smith (ANSTO) is thanked for stimulating discussions. The manuscript was improved through the critical reading and detailed comments of two anonymous reviewers, and through excellent suggestions by John Hanchar. The Rinne Stiftung (Freiburg) is gratefully acknowledged for providing travel funds.

References

Anders, E., Grevesse, N., 1989. Abundances of the elements: meteoric and solar. Geochimica et Cosmochimica Acta 53, 197–214.

Bianchi, A., Callegari, E., Jobstraibizer, G., 1970. I tipi petrografici fondamentali del plutone dell'Adamello. Tonaliti, quarzodioriti e loro varietà leucocrate. . Memorie degli Istituti di Geologia e Mineralogia, vol. 27. Università di Padova, Padova, Italy. 148 pp.

Blundy, J.D., Sparks, R.S.J., 1992. Petrogenesis of mafic inclusions in granitoids of the Adamello Massif, Italy. Journal of Petrology 33, 1039–1104.

Brack, P., 1984. Geologie der Intrusiva und Rahmengesteine des Südwest-Adamello. Ph.D. Thesis, ETH, Zürich, 253 pp.

Brack, P., 1985. Multiple intrusions—examples from the Adamello Batholith (Italy) and their significance on the mechanisms of intrusion. Il Magmatismo Tardo Alpino nelle Alpi. Padova, Italy, pp. 145–157.

Callegari, E., 1985. Geological and petrological aspects of the magmatic activity at Adamello (Northern Italy). Il Magmatismo Tardo Alpino nelle Alpi. Padova, Italy, pp. 83–103.
Callegari, E., Dal Piaz, G.B., 1973. Field relationships between the main igneous masses of the Adamello intrusive massif (Northern Italy). Memorie dell'Istituto di Geologia e Mineralogia, 31. Università di Padova, pp. 1–34 pp.
Chkuaseli, V.F., Matzke, H., 1993. Fission gas bubble behaviour in uranium dioxide. Journal of Nuclear Materials 201, 92–96.
Chkuaseli, V.F., Matzke, H., 1995. Volatile fission product bubble behaviour in uranium dioxide. Journal of Nuclear Materials 223, 61–66.
Del Moro, A., Pardini, G.C., Quercioli, C., Villa, I.M., Callegari, E., 1985. Rb/Sr and K/Ar chronology of Adamello granitoids, Southern Alps. Il Magmatismo Tardo Alpino nelle Alpi. Padova, Italy, pp. 285–299.
Ercit, T.S., 2005. Identification and alteration trends of granitic-pegmatite-hosted (Y, REE,U,Th)–(Nb,Ta,Ti) oxide minerals: a statistical approach. The Canadian Mineralogist 43, 1291–1303.
Ervanne, H., 2004. Uranium oxidation states in allanite, fergusonite and monazite of pegmatites from Finland. Neues Jahrbuch für Mineralogie Monatshefte 7, 289–301.
Ewing, R.C., Chakoumakos, B.C., Lumpkin, G.R., Murakami, T., 1987. The metamict state. Materials Research Society Bulletin 12, 58–66.
Ewing, R.C., Chakoumakos, B.C., Lumpkin, G.R., Murakami, T., Greegor, R.B., Lytle, F.W., 1988. Metamict minerals: natural analogues for radiation damage effects in ceramic nuclear waste forms. Nuclear Instruments and Methods in Physics Research B32, 487–497.
Ewing, R.C., Headley, T.J., 1983. Alpha-recoil damage in natural zirconolite ($CaZrTi_2O_7$). Journal of Nuclear Materials 119, 102–109.
Ewing, R.C., Weber, W.J., Clinard, F.W., 1995. Radiation effects in nuclear waste forms for high-level radioactive waste. Progress in Nuclear Energy 29 (2), 63–127.
Ewing, R.C., Meldrum, A., Wang, L.M., Wang, S.X., 2000. Radiation-induced amorphisation. In: Ribbe, P.H. (Ed.), Reviews in Mineralogy and Geochemistry. Mineralogical Society of America, Washington, D.C., pp. 319–361.
Gieré, R., Guggenheim, R., Düggelin, M., Mathys, D., Williams, C.T., Lumpkin, G.R., Smith, K.L., Blackford, M.G., Hart, K.P., McGlinn, P., 1994. Retention of Actinides during Alteration of Aperiodic Zirconolite, 13th International Congress on Electron Microscopy, Paris, pp. 1269–1270.
Gieré, R., Swope, R.J., Buck, E.C., Guggenheim, R., Mathys, D., Reusser, E., 2000. Growth and alteration of uranium-rich microlite. In: Smith, R., Shoesmith, D. (Eds.), Scientific Basis for Nuclear Waste Management XXIII. Materials Research Society, Boston, MA, pp. 519–524.
Gieré, R., Buck, E.C., Guggenheim, R., Mathys, D., Reusser, E., Marques, J., 2001. Alteration of Uranium-rich microlite. In: Hart, K.P., Lumpkin, G.R. (Eds.), Scientific Basis for Nuclear Waste Management XXIV. Materials Research Society, Sydney, pp. 935–944.
Haidinger, W., 1826. Description of fergusonite, a new mineral species. Transactions of the Royal Society of Edinburgh 10, 271–278.
Hansmann, W., Oberli, F., 1991. Zircon inheritance in an igneous rock suite from the southern Adamello batholith (Italian Alps). Contributions to Mineralogy and Petrology 107, 501–518.
Hartwell, V., 1828. Undersökning af några mineralier. Kongliga Svenska Vetenskaps-Akademiens Handlingar, pp. 167–173.
Headley, T.J., Ewing, R.C., Haaker, R.F., 1981. Amorphous structure of metamict minerals observed by TEM. Nature 293, 449–450.
Kagami, H., Ulmer, P., Hansmann, W., Dietrich, V., Steiger, R.H., 1991. Nd–Sr isotopic and geochemical characteristics of the southern Adamello (Northern Italy) intrusives: implications for crustal versus mantle origin. Journal of Geophysical Research 96, 14331–14346.
Lumpkin, G.R., 1998. Rare-element mineralogy and internal evolution of the Rutherford #2 pegmatite, Amelia County, Virginia: a classic locality revisited. Canadian Mineralogist 36, 339–353.
Lumpkin, G.R., 2001. Alpha-decay damage and aqueous durability of actinite host phases in natural systems. Journal of Nuclear Materials 289, 136–166.
Lumpkin, G.R., Ewing, R.C., 1992. Geochemical alteration of pyrochlore group minerals: microlite subgroup. American Mineralogist 77, 179–188.
Lumpkin, G.R., Ewing, R.C., 1995. Geochemical alteration of pyrochlore group minerals: pyrochlore subgroup. American Mineralogist 80, 732–743.
Lumpkin, G.R., Ewing, R.C., 1996. Geochemical alteration of pyrochlore group minerals: betafite subgroup. American Mineralogist 81, 1237–1248.
Lumpkin, G.R., Ewing, R.C., Chakoumakos, C.C., Greegor, R.B., Lytle, F.W., Foltyn, E.M., Clinard, F.W., Boatner, L.A., Abraham, M.M., 1986. Alpha-recoil damage in zirconolite ($CaZrTi_2O_7$). Journal of Materials Research 1, 564–576.
Lumpkin, G.R., Hart, K.P., McGlinn, P.J., Payne, T.E., Gieré, R., Williams, C.T., 1994a. Retention of actinides in natural pyrochlores and zirconolites. Radiochimica Acta 66/67, 469–474.
Lumpkin, G.R., Smith, K.L., Blackford, M.G., Hart, K.P., McGlinn, P.J., Gieré, R., Williams, C.T., 1994b. Prediction of the long-term performance of crystalline nuclear waste form phases from studies of mineral analogues. In: McDonald, N.R. (Ed.), 9th Pacific Basin Nuclear Conference. The Institution of Engineers, Sydney, Australia, pp. 879–885.
Lumpkin, G.R., Smith, K.L., Blackford, M.G., Gieré, R., Williams, C.T., 1998. The crystalline-amorphous transformation in natural zirconolite: evidence for long-term annealing. In: McKinley, I.G., McCombie, C. (Eds.), Scientific Basis for Nuclear Waste Management XXI. Materials Research Society, Davos, Switzerland, pp. 215–222.
Lumpkin, G.R., Day, R.A., McGlinn, P.J., Payne, T.E., Gieré, R., Williams, C.T., 1999. Investigation of the long-term performance of betafite and zirconolite in hydrothermal veins from Adamello, Italy. In: Wronkiewicz, D.J., L.J.H. (Eds.), Scientific Basis for Nuclear Waste Management XXII. Materials Research Society, Boston, MA, pp. 793–800.
Lumpkin, G.R., Leung, S.H.F., Colella, M., 2000. Composition, geochemical alteration, and alpha-decay damage effects of natural brannerite. In: Smith, R.W., Shoesmith, D.W. (Eds.), Scientific Basis for Nuclear Waste Management XXIII. Materials Research Society, Boston, pp. 359–365.
Lumpkin, G.R., Smith, K.L., Gieré, R., Williams, C.T., 2004. Geochemical behaviour of host phases for actinides and fission products in crystalline ceramic nuclear waste forms. In: Gieré, R., Stille, P. (Eds.), Energy, Waste and the Environment: A Geochemical Perspective. The Geological Society, London, pp. 89–111. Special Publications.
Murakami, T., Chakoumakos, B.C., Ewing, R.C., Lumpkin, G.R., Weber, W.J., 1991. Alpha-decay event damage in zircon. American Mineralogist 76, 1510–1532.
Nasdala, L., Massonne, H.-J., 2000. Microdiamonds from the Saxonian Erzgebirge, Germany: in-situ micro-Raman characterisation. European Journal of Mineralogy 12, 495–498.
Nasdala, L., Wenzel, M., Vavra, G., Irmer, G., Wenzel, T., Kober, B., 2001. Metamictisation of natural zircon: accumulation versus thermal annealing of radioactivity-induced damage. Contributions to Mineralogy and Petrology 141, 125–144.
Olivo, G.R., Williams-Jones, A.E., 1999. Hydrothermal REE-rich eudialyte from the Pilanesberg Complex, South Africa. The Canadian Mineralogist 37, 653–663.
Perrillat, J.P., Daniel, I., Lardeaux, J.M., Cardon, H., 2003. Kinetics of the coesite–quartz transition: application to the exhumation of ultrahigh-pressure rocks. Journal of Petrology 44, 773–788.
Pouchou, J.L., Pichoir, F., 1984. Un nouveau modèle de calcul pour la microanalyse quantitative par spectrométrie de rayons X. Partie I: Application à l'analyse d'échantillons homogènes. Recherches Aérospatiales 3, 167–192.
Rajesh, V.J., Yokoyama, K., Santosh, M., Arai, S., Oh, C.W., Kim, S.W., 2006. Zirconolite and baddeleyite in an ultramafic suite from Southern India: Early Ordovician carbonatite-type melts associated with extensional collapse of the Gondwana crust. The Journal of Geology 114, 171–188.
Ramsay, W., 1896. Helium, a gaseous constituent of certain minerals. Part II—density. Proceedings of the Royal Society, London 59, 325–330.
Ramsay, W., Travers, M.W., 1898. Fergusonite, an endothermic mineral. Proceedings of the Royal Society, London 62, 325–329.
Riklin, K., 1985. Contact metamorphism of the Permian "Red Sandstones" in the Adamello area. Il Magmatismo Tardo Alpino nelle Alpi. Padova, Italy, pp. 159–169.
Ruschel, K., Nasdala, L., Gaft, M., Schnier, C., Schlüter, J., 2007. Photoluminescence recovery upon annealing of fergusonite (Abstract), Goldschmidt Conference 2007. Goldschmidt Conference Abstracts, Köln, p. A861.
Tomašić, N., Gajovi, ć, A., Bermanec, V., Su, D.S., Rajić Linarić, M., Ntaflos, T., Schlögl, R., 2006. Recrystallization mechanisms of fergusonite from metamict mineral precursors. Physics and Chemistry of Minerals 33, 145–159.
Ulmer, P., Callegari, E., Sonderegger, U.C., 1985. Genesis of the mafic and ultramafic rocks and their genetical relations to the tonalitic trondhjemitic granitoids of the southern part of the Adamello batholith (Northern Italy). Il Magmatismo Tardo Alpino nelle Alpi. Padova, Italy, pp. 171–222.
Utsunomiya, S., Ewing, R.C., 2003. Application of high-angle annular dark field scanning transmission electron microscopy, scanning transmission electron microscopy-energy dispersive X-ray spectrometry, and energy-filtered transmission electron microscopy to the characterization of nanoparticles in the environment. Environmental Science and Technology 37, 786–791.
Wang, R.C., Fontan, F., Chen, X.M., Hu, H., Liu, C.S., Xu, S.J., De Parseval, P., 2003. Accessory minerals in the Xihuashan Y-enriched granitic complex, Southern China: a record of magmatic and hydrothermal stages of evolution. The Canadian Mineralogist 41, 727–748.
Warner, J.K., Ewing, R.K., 1993. Crystal chemistry of samarskite. American Mineralogist 78, 419–424.
Weber, W.J., Ewing, R.C., Catlow, C.R.A., Diaz de la Rubia, T., Hobbs, L.W., Kinoshita, C., Matzke, H.j., Motta, A.T., Nastasi, M., Salje, E.K.H., Vance, E.R., Zinkle, S.J., 1998. Radiation effects in crystalline ceramics for the immobilization of high-level nuclear waste and plutonium. Journal of Materials Research 13 (6), 1434–1484.
Wirth, R., 2004. Focused ion beam (FIB): a novel technology for advanced application of micro- and nanoanalysis in geosciences and applied mineralogy. European Journal of Mineralogy 16, 863–876.
Zhang, Z., Gieré, R., Stünitz, H., Brack, P., Ulmer, P., 2001. Garnet–quartz intergrowths in granitic pegmatites from Bergell and Adamello, Italy. Schweizerische Mineralogische und Petrographische Mitteilungen 81, 89–113.

2.3 Chemical alteration patterns in metamict fergusonite

(2010)

Ruschel, K., Nasdala, L., Rhede, D., Wirth, R., Lengauer, C.L. & Libowitzky, E.

European Journal of Mineralogy, 22:425–433

Eur. J. Mineral.
2010, **22**, 425–433
Published online April 2010

Chemical alteration patterns in metamict fergusonite

KATJA RUSCHEL[1,*], LUTZ NASDALA[1], DIETER RHEDE[2], RICHARD WIRTH[3], CHRISTIAN L. LENGAUER[1] and EUGEN LIBOWITZKY[1]

[1] Institut für Mineralogie und Kristallographie, Universität Wien, 1090 Wien, Austria
*Corresponding author, e-mail: katja.ruschel@univie.ac.at
[2] Sektion 4.2, Anorganische und Isotopengeochemie, Helmholtz-Zentrum Potsdam, Deutsches GeoForschungsZentrum GFZ, 14473 Potsdam, Germany
[3] Sektion 3.3, Chemie und Physik der Geomaterialien, Helmholtz-Zentrum Potsdam, Deutsches GeoForschungsZentrum GFZ, 14473 Potsdam, Germany

Abstract: A fergusonite sample from the Berere region in Madagascar was studied in detail with a wide range of analytical methods, including optical and scanning electron microscopy, transmission electron microscopy techniques, electron probe microanalysis and mapping, powder X-ray diffraction, and Raman, photoluminescence and infrared spectroscopy. The specimen contains high concentrations of actinide elements (U up to 6.9 wt%, Th up to 3.0 wt% as oxides) and, as a consequence, it is highly radiation-damaged. The sample has experienced intense, low-*T* chemical alteration through fluid-driven replacement reactions. The altered areas have sharp boundaries to their neighbouring host and are mainly located adjacent to large fractures. High-resolution element distribution maps show the complexity of the compositional changes. Altered areas are generally enriched in Si and Ca, and depleted in Y; however, most elements show variable trends and heterogeneous distribution patterns pointing to a non-uniform, presumably multi-step alteration history. Most remarkably, the actinides U and Th were comparably immobile; their concentrations having remained almost constant, being only mildly affected by the alteration reaction. This appears to support the potential suitability of the fergusonite-group minerals as host phases for the long-term immobilisation of nuclear waste.

Key-words: fergusonite-(Y), radiation damage, chemical alteration, element mapping.

1. Introduction

Similar to other (Y,REE,U,Th)–(Nb,Ta,Ti) oxides, fergusonite (ideal formula: $YNbO_4$), occurs typically as an accessory component in granites (Poitrasson *et al*., 1998; Wang *et al*., 2003) and granitic pegmatites (Ercit, 2005; Gieré *et al*., 2009). Due to its actinide content of several weight percent, fergusonite is commonly found in a highly radiation-damaged state (Ervanne, 2004; Janeczek, 2004; Gieré *et al*., 2009), which is accompanied by major changes of physical properties and generally lowered chemical resistance. Correspondingly, fergusonite and other Nb–Ta–Ti oxide minerals are often affected by post-growth chemical alteration (Ewing, 1975; Ercit, 2005). Alteration processes are commonly subdivided into primary and secondary (Van Wambeke, 1970; Ewing, 1975; Lumpkin & Ewing, 1992). Primary alteration may take place shortly after crystal growth (and hence prior to significant accumulation of radiation damage), for instance during subsequent cooling in a late magmatic, pegmatitic, or hydrothermal environment (Gieré *et al*., 2001). In contrast, secondary alteration occurs in the post-growth history (*i.e.*, normally after the accumulation of radiation damage) at low temperatures due to hydrothermal overprinting or near-surface weathering processes. Primary alteration is mostly dominated by intracrystalline diffusion, while secondary alteration is controlled by fluid transport through cracks and voids (Lumpkin & Ewing, 1995).

Most studies addressing the alteration of (Y,REE,U,Th)–(Nb,Ta,Ti) oxides have dealt with the more common pyrochlore-group minerals (Lumpkin & Ewing, 1992, 1995, 1996; Lumpkin *et al*., 2001, 2004). In contrast, alteration of fergusonite has rarely been described (*e.g.*, Lumpkin, 1998; Ervanne, 2004; Janeczek, 2004). Ercit (2005) provided a summary of alteration trends of (Y,REE,U,Th)–(Nb,Ta,Ti) oxide minerals based on their chemical composition and distinguished six compositional effects of alteration, including (i) hydration, (ii) gain of high field strength elements (HFSE), (iii) gain of large ion lithophile elements (LILE), (iv) addition of Ca, (v) exchange of heavy rare earth elements (HREE) and Y for light rare earth elements (LREE) other than Y, and (vi) loss of A-cations. Studies of alteration processes in fergusonite are of petrological interest because complex Nb–Ta–Ti–REE oxide minerals can act as monitors for the evolution of their host rocks and in particular of low-*T* geochemical processes in them (Tomašić *et al*., 2004).

DOI: 10.1127/0935-1221/2010/0022-2031
0935-1221/10/0022-2031 $ 4.05

Additionally, knowledge of the chemical alteration behaviour of actinide-bearing minerals is crucial to predict their suitability and performance as ceramic host material for the long-term immobilisation of radioactive waste. Gieré *et al*. (2009) discussed fergusonite as a potential phase to be included in ceramics for the immobilisation of nuclear waste, however, they noticed that more reliable information on the alteration characteristics of this mineral is needed. In the present case study, we have investigated in detail a metamict fergusonite sample from Madagascar that suffered intense chemical and physical alteration.

2. Sample and experimental details

The sample studied is a large (*i.e.*, >1 cm size) fergusonite specimen from the Berere region, Madagascar. Note, however, that the chemical composition of some of the heavily altered areas does not correspond to that of fergusonite anymore; nevertheless the terms ''fergusonite'' and ''altered fergusonite'' will be used throughout the paper. The sample's precise origin is unknown. In spite of this, it appears likely that it was derived from one of the *ca*. 550 Ma old (Mücke & Strunz, 1978) pegmatites in the Berere region. The specimen is for the most part dark brownish in colour. Its alteration is obvious already in the unprepared stage: The surface is cross-cut by several cracks filled with a yellowish material.

The sample was cut, and a fraction was, after homogeneity checks under the binocular microscope, subjected to a total of twelve heating experiments. For this, chips (sizes $\sim$0.3–1.0 mm) were individually placed in a platinum crucible and annealed in air at temperatures between 300 °C and 1400 °C (heating rate 10 °C/min) for four days.

Doubly polished thin sections (thicknesses of $\sim$30 μm) attached to glass slides were produced from the untreated sample as well as from annealed chips. These sections were used for electron probe microanalyser (EPMA), Raman, and photoluminescence (PL) spectroscopy measurements. Prior to EPMA analysis, thin sections were coated with carbon. For infrared (IR) absorption spectroscopy, a doubly polished platelet (100 μm thickness) of the untreated material was prepared. For X-ray diffraction analysis, about 8 mg of untreated and annealed sample material were ground in an agate mortar and fixed with grease on low-background silicon sample carriers (front loading). For transmission electron microscope (TEM) studies, electron-transparent foils (typical dimensions of $\sim 10 \times 15$ μm and $\sim$0.15 μm thickness) were cut out of a thin section of an untreated chip, by the focused ion beam (FIB) technique using a FEI FIB200 (see Wirth, 2004 for details).

The thin sections were first examined under an optical microscope. Subsequently back-scattered electron (BSE) and secondary electron (SE) images were obtained using a JEOL JSM–6400 scanning electron microscope (SEM) at an accelerating voltage of 20 kV.

Powder X-ray diffraction data were collected on a Bruker AXS D8 Advance system with θ–θ geometry ($r =$ 250 mm), using Cu $K\alpha$ radiation at 40 kV and 40 mA. The diffractometer was equipped with a sample spinner and an energy-dispersive Sol-X detector. A receiving slit of 0.1 mm (0.033° 2θ), two 2.3° (0.04 rad) soller slits on each side of the sample stage and the variable mode for divergence and antiscatter slits (8 mm) were used. The measurements were performed at 28 °C and 1 bar over a range of 15 to 95° 2θ (–60° 2θ displayed) with a step interval of 0.01° 2θ. The counting time was set to 9 s per step, and the spinner speed was 0.33 rps.

Raman and laser-induced PL spectra were obtained in quasi back-scattering geometry using an edge-filter based Renishaw RM1000 system equipped with a Leica DMLM optical microscope (50× objective, numerical aperture 0.75) and Peltier-cooled, Si-based charge-coupled device (CCD) detector. Spectra were excited with the 488 nm emission line of an Ar^+ laser (17 mW). The lateral resolution was $\sim$4–5 μm. Band positions were calibrated using the Rayleigh line and neon lamp emission lines; the resulting wavenumber accuracy was better than 1 cm^{-1}. The spectral resolution was $\sim$5–6 cm^{-1} (which corresponds to <0.2 nm). Infrared absorption spectroscopy was done with a Bruker Tensor 27 Fourier-transform infrared (FTIR) system equipped with a Hyperion IR microscope. Spectra were recorded in transmission mode in the range 500 to 7500 cm^{-1}. The spectral resolution was 4 cm^{-1}.

Electron microprobe analysis and high-resolution element mapping, along with additional BSE imaging, was performed by means of a JEOL JXA–8500F thermal field emission-type EPMA. Point analyses were obtained using a focused electron beam (diameter $\leq$1 μm), an acceleration voltage of 15 kV, and a beam current of 30–40 nA. The following natural and synthetic reference materials were used (respective element and peak counting time listed in parentheses): wollastonite (Si and Ca; 20 s), rutile (Ti; 20 s), Fe_2O_3 (Fe; 20 s), Ta_2O_5 (Ta; 30 s), Al_2O_3 (Al; 20 s), $ZrSiO_4$ (Zr; 50 s), Th-metal (Th; 100 s), U-metal (U; 100 s), vanadinite (Pb; 100 s), $MnNb_2O_5$ (Mn and Nb; 20 s), and rare earth element phosphates (REE and P; 50 s). The background counting times were always set to one half of the respective peak counting times. The CITZAF routine in the JEOL software, which is based on the $\Phi(\rho Z)$ method (Armstrong, 1995), was used for data processing. Where applicable, the results were corrected for REE peak overlaps. The element distribution maps were obtained in wavelength-dispersive X-ray spectroscopy (WDS) mode with an acceleration voltage of 15 kV, a probe current of 15–20 nA, and a dwell time of 0.25–0.60 s per step (stage step intervals 0.4–0.5 μm).

Transmission electron microscope investigations were performed with a FEI Tecnai G2 F20 X–Twin system operated at a voltage of 200 kV. Images in the scanning transmission electron microscopy (STEM) mode were generated with a high-angle annular dark field (HAADF) detector (Fishione Model 3000). Element line scans were obtained with an energy-dispersive X-ray (EDX) spectrometer.

3. Results and discussion

3.1. General sample description

Images of the fergusonite sample visualising its internal texture are presented in Fig. 1. The sample reveals two textural types. The first type covers approximately 80 % of the thin section area. In plane-polarised light it can be seen as various shades of brown, with a rather ''turbulent'' appearance (Fig. 1a). In the BSE images this textural type appears bright and shows weak zoning, which resembles primary growth zoning in some areas (see arrows in Fig. 3c) whereas it has a rather patchy appearance in other areas. Interestingly, there is an apparent contradiction between details seen in the transmitted light and BSE images. The ''turbulent'' appearance is not seen in the BSE whereas the weak primary zoning cannot be recognised in the transmitted light (compare Fig. 1a, b). It remains questionable (especially because of the ''turbulent'' textures observed in transmitted light) whether this material is unaltered. These doubts seem to be further supported by numerous dark spots with sizes up to several μm in the BSE images. Nevertheless, we will refer to the first textural type as the (apparently unaltered) host phase in the following. The second textural type, covering approximately 20 % of the thin section area, appears considerably less intensely coloured in the plane-polarised transmitted light (Fig. 1a). It is mostly located along large fractures or cracks and often has a finger-like appearance (Fig. 1b). This second type, which consists of distinct altered patches, is characterised by much lower BSE intensities when compared to the host material.

The boundary between the two textural types is always sharp. Both of them may occasionally contain scattered mineral inclusions of a few μm or smaller size, which are characterised by a much higher BSE intensity than the host fergusonite. Energy-dispersive X-ray scans in the SEM (not shown) revealed the presence of high concentrations of U and Th in these inclusions. This is consistent with the observations of Ewing & Ehlmann (1973), Janeczek (2004), and Gieré *et al*. (2009) who found uraninite and other U-bearing phases as common inclusions in fergusonite.

3.2. Structural characterisation

The sample does not show notable interference colours in cross-polarised light. This indicates a high level of structural radiation damage. The X-ray diffraction pattern as well as Raman and PL spectra of the sample (Fig. 2) confirm its metamict state, as they display only the typical ''amorphous hump'' (X-ray), the absence of well-defined vibrational bands (Raman), and REE emissions without notable fine structure (PL), respectively.

Hence the structural characterisation of the material was only possible after recrystallisation through thermal annealing. However, it should be noted that heat-treatment of a radiation-amorphised sample does not necessarily result in the recovery of its original structural state. The formation of another crystalline phase or decomposition into several (crystalline and/or amorphous) phases is also possible (Nasdala *et al*., 2002; Váczi *et al*., 2009). This uncertainty increases if, due to chemical alteration, the chemical composition of the material to be annealed differs from its primary composition (Ewing, 1975; Ewing & Ehlmann, 1975; Tomašić *et al*., 2008). The X-ray diffraction patterns of the annealed samples (only one of them is presented in Fig. 2a) indicate recrystallisation of tetragonal α-fergusonite at about 600 °C and its transition to monoclinic β-fergusonite between 800 and 1000 °C. This α–β transition has been described in more detail by Tomašić *et al*. (2006) who, however, reported the recrystallisation to start at about 400 °C. Raman and PL analyses of the annealed samples further verified the annealing process. The Raman spectrum taken after annealing at 1400 °C

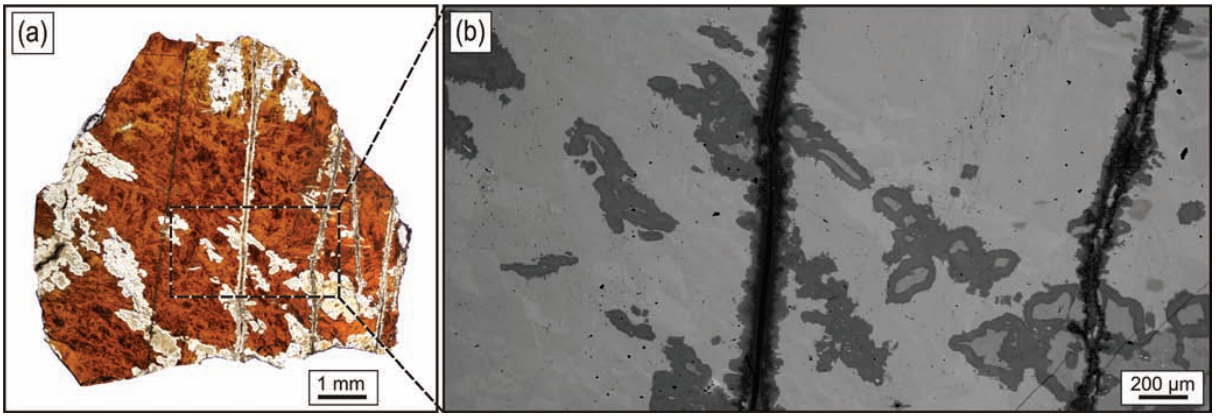

Fig. 1. Images of the fergusonite sample from Madagascar. (a) Photomicrograph, plane-polarised transmitted light. (b) BSE image. The two textural types are easily distinguished: The host fergusonite is brown and has a ''turbulent'' appearance in the transmitted light, and it shows high intensity in the BSE image. Altered areas, which are often located close to large fractures, are nearly colourless in transmitted light and show low BSE intensity.

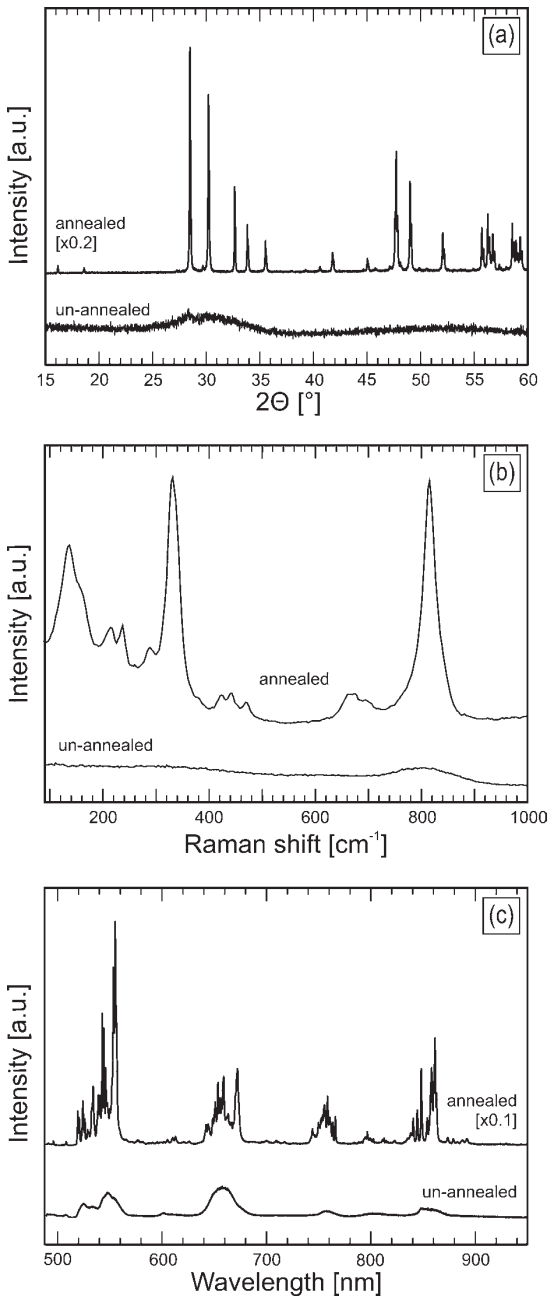

Fig. 2. Comparison of analytical results obtained from the amorphous fergusonite sample and its crystalline analogue produced by dry annealing at 1400 °C: (a) X-ray diffraction patterns (Cu $K\alpha$ radiation), (b) Raman spectra (488 nm excitation), and (c) PL spectra (488 nm excitation). Diffraction patterns and spectra, respectively, are shown with a vertical offset for more clarity. Note that the heat-treatment resulted in the formation of monoclinic β-fergusonite.

(Fig. 2b) corresponds reasonably well to a spectrum of a synthetic, fergusonite-type $YNbO_4$ phase (Yashima *et al.*, 1997). In the PL spectrum of the annealed sample (Fig. 2c), all REE emission bands (Ruschel *et al.*, 2007) have notable fine structures which are assigned to crystal-field effects in the recrystallised fergusonite.

3.3. Chemical composition

Results of electron microprobe analyses are presented in Table 1. Note that all values reported are means of multiple point analyses. The chemical composition of the host material corresponds to fergusonite [classified according to the statistical method of Ercit (2005) for the identification of (Y,REE,U,Th)–(Nb,Ta,Ti) oxide minerals based on their chemical composition]. The host material consists mainly of ~29 wt% Y_2O_3, ~35–36 wt% Nb_2O_5 and ~14–15 wt% Ta_2O_5. In addition, a relatively wide range of other elements (including Ti, Gd, Dy, Er, Yb, Th, and U) are present at variable concentrations and with individual oxides up to the wt% range (Table 1). Calcium, REE other than Y, Th, and U, are likely to substitute for Y (the A-site in the fergusonite structure) whereas Si, Ti, and Ta are assumed to substitute for Nb (B-site; Tomašić *et al.*, 2004; Gieré *et al.*, 2009). Based on this structural assignment, the A:B ratio as obtained in our analyses is approximately 1:1, which agrees very well with the ABO_4 stoichiometry of fergusonite. The simplified chemical formula, normalised to 4 oxygen atoms per formula unit, was calculated as $(Y_{0.7}Dy_{0.1}M_{0.2})(Nb_{0.8}Ta_{0.2})O_4$ (with M = Ca, Nd, Sm, Gd, Ho, Er, Yb, Th and U in the range 0.005–0.05). Our observation that a large number of non-formula elements are present in notable quantity (Table 1) is consistent with previous studies on fergusonite, in which extensive chemical variability has been reported for this mineral (*e.g.*, Ervanne, 2004; Janeczek, 2004; Gieré *et al.*, 2009).

As expected, the chemical compositions of the altered areas were found to be heterogeneous and to deviate appreciably from the composition of the host material, as discussed in more detail below. All altered areas yield deficient analytical totals (down to mean values of ~93 wt%), which is a typical feature of minerals that have undergone fluid-driven alteration (Smith *et al.*, 1991; Förster, 1998; Mathieu *et al.*, 2001). Possible causes of low analytical totals include the presence of hydrous or other elemental species that are not detected in the EPMA, and in particular X-ray intensity losses at grain boundaries or sub-micrometre pores of the altered material (see Nasdala *et al.*, 2009, and references therein).

To check for the hypothetical incorporation of hydrous species, IR spectroscopy was used. All IR spectra (not shown) are characterised by a broad and strongly asymmetric band in the range 2600–3600 cm^{-1} (maximum near 3400 cm^{-1}); its intensity is notably higher in altered areas, compared to the host fergusonite. This band indicates strongly the presence of a hydrous species, as it resembles the O–H signal of other highly metamict minerals such as zircon (Caruba *et al.*, 1985; Nasdala *et al.*, 2001, 2009). An unambiguous assignment to hydroxyl groups and/or water molecules, however, cannot be given. Also, we do not attempt to calculate concentrations of the hydrous species from the O–H band integrals, because the calculation

Table 1. Results of EPMA chemical analyses (all concentrations in wt%).

Region	Textural type	No.[a]	Al_2O_3	SiO_2	P_2O_5	CaO	TiO_2	MnO	FeO	Y_2O_3	ZrO_2	Nb_2O_5	Ce_2O_3	Nd_2O_3	Sm_2O_3	Gd_2O_3	Tb_2O_3	Dy_2O_3	Ho_2O_3	Er_2O_3	Yb_2O_3	Lu_2O_3	Ta_2O_5	PbO	ThO_2	UO_2	Total
Areas marked in the BSE image in Fig. 3a:																											
1	Host	4	bdl	0.06	bdl	0.25	1.39	bdl	bdl	29.29	bdl	35.30	0.19	0.55	0.78	2.22	0.58	3.56	0.44	1.51	1.40	0.22	14.76	0.28	2.36	4.67	99.82
2	Altered	4	0.87	9.38	bdl	7.72	1.29	0.29	1.24	6.39	bdl	33.06	0.38	0.61	0.56	0.95	bdl	1.45	bdl	0.51	0.58	bdl	19.49	0.27	2.35	5.56	93.35
3	Altered	4	1.17	7.37	bdl	0.06	1.48	bdl	2.73	3.19	1.08	29.82	0.40	0.54	0.47	0.84	bdl	1.09	bdl	0.34	0.44	bdl	31.48	3.35	2.66	6.90	95.65
4	Fracture-filling	4	bdl	5.18	23.66	1.29	bdl	bdl	0.96	45.49	bdl	1.44	bdl	0.27	0.27	1.53	0.43	3.72	0.53	2.37	3.14	0.47	0.83	0.04	0.51	0.54	92.67
Average detection limit [b]			0.04	0.05	0.09	0.03	0.07	0.06	0.07	0.03	0.13	0.10	0.09	0.14	0.15	0.16	0.17	0.18	0.20	0.21	0.10	0.11	0.17	0.02	0.01	0.02	
Areas marked in the BSE image in Fig. 3c:																											
5	Host	3	bdl	0.09	bdl	0.27	1.35	bdl	bdl	29.31	bdl	35.72	0.22	0.65	0.79	2.15	0.57	3.65	0.48	1.54	1.32	0.21	14.29	0.27	2.60	4.55	100.03
6	Host	3	bdl	0.07	bdl	0.27	1.25	bdl	bdl	29.21	bdl	35.82	0.26	0.59	0.88	2.32	0.49	3.60	0.33	1.54	1.38	0.21	14.11	0.28	2.68	4.59	99.89
7	Altered	3	bdl	0.31	bdl	2.19	1.71	bdl	bdl	28.25	bdl	32.33	0.15	0.54	0.84	2.21	0.59	3.36	0.36	1.36	1.17	0.18	15.02	0.07	3.01	4.12	97.77
8	Altered	3	bdl	0.20	bdl	2.02	1.61	bdl	bdl	27.74	bdl	32.97	0.13	0.54	0.76	2.14	0.53	3.32	0.45	1.41	1.26	0.20	15.32	0.11	2.94	4.57	98.22
Average detection limit [b]			0.03	0.05	0.09	0.03	0.07	0.06	0.07	0.04	0.13	0.11	0.10	0.15	0.16	0.17	0.18	0.20	0.21	0.22	0.11	0.12	0.19	0.02	0.01	0.02	

bdl = not detected, or average below detection limit.
[a]Number of single analyses per interior region.
[b]Average detection limit (wt% oxide, 2 σ error by counting statistics of the background signal).

procedures (see Libowitzky & Rossman, 1996, 1997) were found to be uncertain for metamict samples. For instance, Nasdala *et al*. (2001; see Fig. 8 in that paper) reported systematic deviations of hydrous contents calculated from O–H band integrals from the actual contents that exceeded one order of magnitude. Nevertheless, IR spectra indicate that hydrous species are present, and that their content is notably enhanced in altered areas.

3.4. Study and discussion of alteration textures

To obtain more precise information about the element distribution patterns, EPMA element mapping was applied. A selection of results is presented in Fig. 3. The altered areas are much more heterogeneous in composition than the host phase. Occasionally, element distribution maps correlate with the internal ''primary'' zoning of the host material as seen in BSE images (*e.g.*, compare BSE image and Y map in Fig. 3c). However, within the altered material, there are notable lateral variations in the degree of chemical heterogeneity. For instance, the finger-like alteration areas that protrude into the host material show a rather moderate zoning of their chemical composition (Fig. 3c), whereas altered areas close to large fractures (Fig. 3a) may be extremely heterogeneous, in some cases on a micrometre-scale.

The alteration-induced chemical changes in the fergusonite sample studied appear to correspond well with general observations discussed by Janeczek (2004). However, only a few elements show a clear trend in their alteration behaviour: Silicon is generally enriched, Y is significantly depleted, and other REEs are moderately depleted in the altered areas. Most elements, however, appear to be distributed less systematically. The Ca content is in general enriched in the altered patches, but it can be also depleted locally (see Fig. 3a). Niobium tends to be somewhat depleted in areas several tens of μm away from large fractures, whereas it is notably enriched in close proximity to these fractures (Fig. 3a). The distribution patterns of Ta, Pb, Th, and U in the altered patches are rather irregular and can vary from map to map. These elements tend to be slightly depleted in the finger-like alteration areas, whereas in areas close to large fractures they may either be depleted and/or enriched locally (Fig. 3a, b). The large fractures, which have clearly served as pathways for the alteration fluids, are often filled with secondary phases that differ appreciably in composition from the neighbouring altered material. The fracture fillings consist mainly of phases rich in P and Y and, to a lesser extent, Si (Fig. 3a, b). In contrast, most major elements of the fergusonite show insignificant concentrations in the secondary fracture fillings (Table 1). Our observations correspond very well to recent findings of Nasdala *et al*. (2010) who applied EPMA element mapping to study fluid-driven alteration in heavily radiation-damaged zircon. These authors also observed a strong Ca enrichment and Y depletion in altered patches whereas fracture fillings showed particularly high Y contents (which, however, were not combined with detectable P contents).

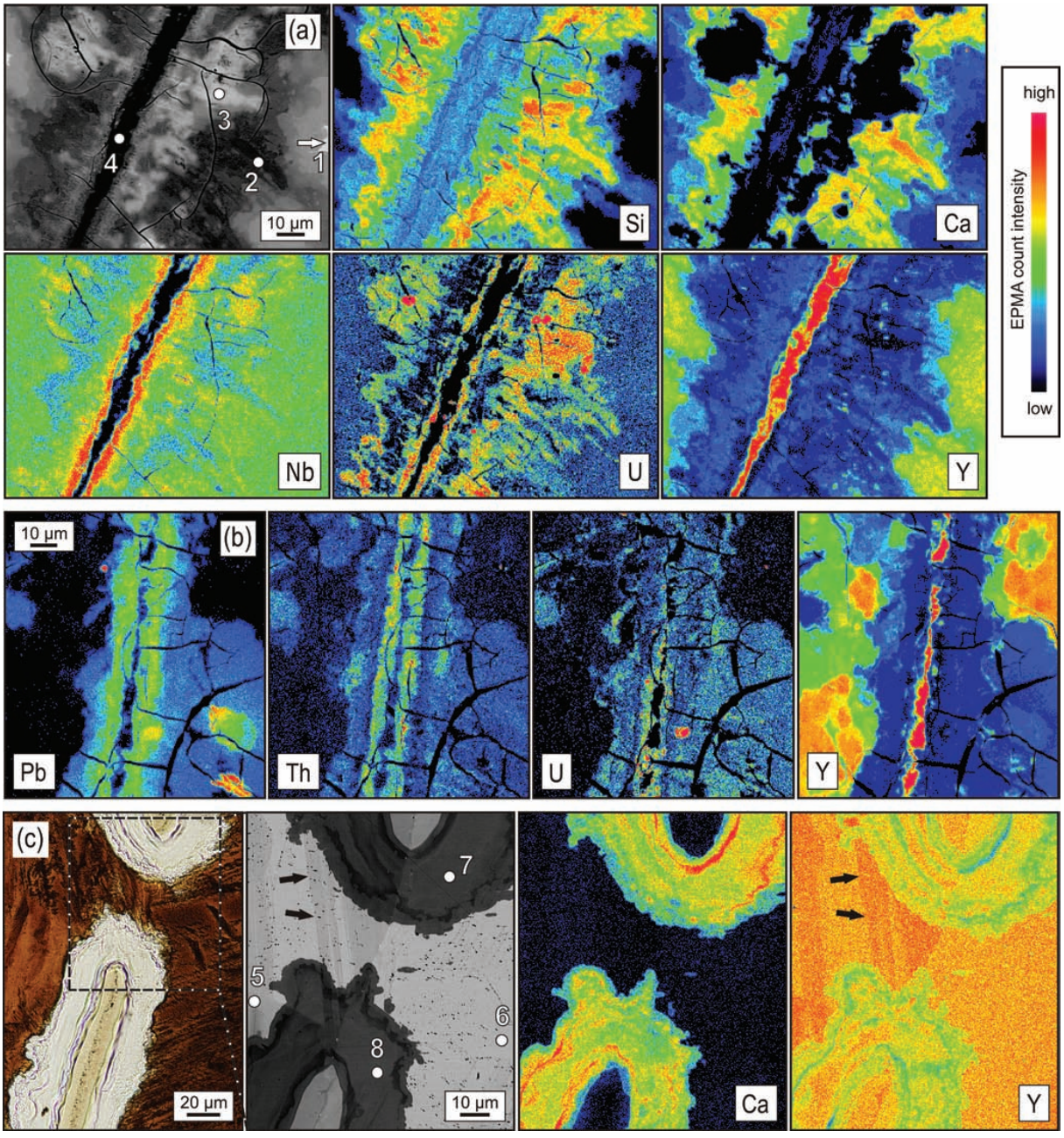

Fig. 3. Three series of images documenting results of the EPMA element mapping. (a) Area within an altered zone adjacent to a large, secondary filled fracture (from left to right: BSE image; and five element distribution patterns obtained with a current of 1.5×10^{-8} A and a dwell time of 0.3 s). Colour-coded intensity ranges (given in counts) are 19–692 (Si), 51–1401 (Ca), 4–171 (Nb), 65–170 (U), and 20–1126 (Y). (b) Another area within an altered zone near a large fracture (four element distribution patterns, 2.0×10^{-8} A, dwell time 0.6 s). Colour-coded intensity ranges are 19–412 (Pb), 35–179 (Th), 66–165 (U), and 65–2256 (Y). (c) Area consisting of the host phase and two finger-like, altered zones (from left to right: plane-polarised transmitted light micrograph; BSE image; and two element distribution patterns, 1.5×10^{-8} A, dwell time 0.25 s). Colour-coded intensity ranges are 18–152 (Ca) and 327–677 (Y). Black arrows point toward weak primary zoning. Numbered spots 1–8 in the two BSE images correspond to the chemical analyses listed in Table 1. Analysis 1 was placed in the host phase (located slightly outside the rectangular area shown in the upper row).

Transmission electron microscopy was applied to study the interface between altered patches and the neighbouring host phase on a sub-micrometre scale. High-angle annular dark field images and EDX line scans verified the sharpness of the compositional interface. In the HAADF image presented in Fig. 4, the slightly darker band marked ''A'' represents the boundary of the chemical alteration where element line scans (in particular Ca and Y) indicated sharp compositional gradients. This sharpness suggests that the contribution of volume diffusion was insignificant. The reason for the significant HAADF brightness change along a vertical line (marked ''B'' in Fig. 4) that has a clear lateral offset relative to the chemical boundary (marked ''A'' in Fig. 4) remains unclear. Possible causes of the brightness variation include density variations or minor differences in concentrations of heavy elements that can not be quantified, but might strongly influence the contrast. Note, however, that line ''B'' does not correspond to any element distribution observed.

The HAADF image shows the occurrence of numerous dark, circular features with sizes of $\leq$ 200 nm in the host fergusonite (Fig. 4). Energy-dispersive X-ray analyses did not reveal systematic differences in chemical composition between the dark features and the surrounding unaltered material (a moderate drop in total X-ray counts was however noticed for measurements placed inside the dark circles). The dark contrast of the circular areas might be due to lower density or smaller total thickness of the material. In the TEM bright field images (not shown) they appear bright. This observation is complementary to the HAADF image because lower density and/or reduced sample thickness reduces electron absorption resulting in brighter contrast. Correspondingly, the features might be assigned to areas with lower average atomic number; most likely holes.

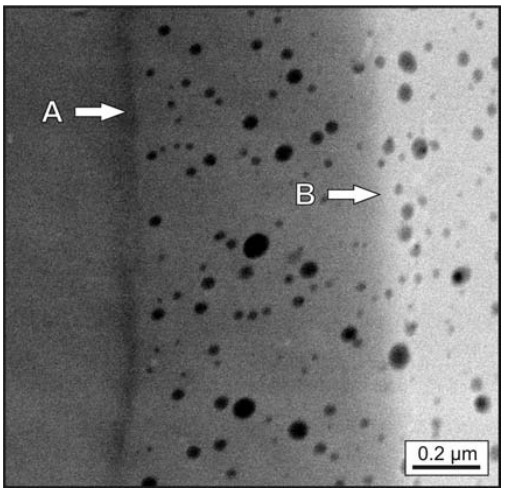

Fig. 4. High-angle annular dark field image showing the boundary between a finger-like alteration patch (left) and the adjacent host fergusonite (centre and right). The amorphous host fergusonite shows numerous dark features (circular pores?) whereas the altered area appears homogeneously dense and does not show this peculiarity. The slightly darker band on the left side, marked ''A'', represents the boundary of the chemical alteration (as detected by elemental line scans in the TEM). In contrast, the clear brightness change along the vertical line marked ''B'' does not correspond to any element distribution pattern observed.

The altered areas, in contrast, appear homogeneously dense and do not show this peculiarity. Gieré *et al.* (2009) attempted to interpret similar features as remnants of bubbles resulting from the accumulation of radiogenic helium. This hypothesis, however, does not seem to be supported by our observations as there are no such bubbles or holes, at least not on the observed scale, in the altered zones of our sample, even though these zones have undergone strong metamictisation and should therefore have accumulated high amounts of radiogenic helium. Of course there exists the possibility that the altered phase is much younger than the host material and therefore contains considerably less helium. Also, it cannot be excluded that the circular features may have formed in an earlier alteration process and were locally healed during a younger alteration. Nevertheless, the virtual absence of pores in the altered patches of the fergusonite sample is a most puzzling observation.

Micrometre-range porosity is a common phenomenon of minerals, or areas within minerals, that have experienced a fluid-driven alteration reaction, which typically has a somewhat negative mass balance (Putnis, 2002). Alteration-induced porosity is, in general, particularly extensive in cases where a radiation-damaged, and hence volume-expanded, mineral is replaced by its crystalline (non-expanded) analogue (Pointer *et al*., 1988; Nasdala *et al*., 2009). This was probably also the case in the sample studied, provided the alteration has not occurred immediately after primary fergusonite growth (*i.e.*, before significant accumulation of radiation damage). There exists the possibility that in our case, pores in the altered areas are too small to be seen in the HAADF images. Also, they may have been filled by some kind of re-sealing process (as for instance discussed by Putnis, 2002; Geisler *et al*., 2005). In summary however, both the assignment of the circular features in the host phase and the absence of pores in the altered phase remain unclear at the present state.

In spite of the puzzling observations above, the TEM images and line scans confirmed that the boundaries between altered areas and their neighbouring host are always sharp. This is strong evidence for an alteration reaction along a moving, fluid-driven reaction front. Such a process, where stoichiometric dissolution is coupled with the simultaneous growth of a thermodynamically more stable product phase, is often referred to as a dissolution-reprecipitation (Putnis, 2002, 2009) process. Solid-state diffusion is another alteration mechanism that can occur during interaction of a fluid with a solid host; however, this process is expected to result in gradual transitions of elemental compositions, which is not observed in our case. Nevertheless it appears likely that both, volume diffusion and fluid-driven alteration, have contributed at different stages, and to different degrees, to the complex alteration observed. The heterogeneous, partly zoned and partly

patchy, distributions of elements point to a non-uniform, most likely multi-stage alteration process, with dramatic variations of the fluid composition. For instance, the Ca distribution in Fig. 3a suggests that this element was enriched in early steps of the alteration but later leached-out. The fracture fillings are assumed to represent the youngest step of alteration.

Given the major chemical changes caused by the alteration reaction, it is remarkable that host and altered material show comparably small variations in the concentrations of the actinides U and Th (Table 1; Fig. 3a, b). The alteration has not resulted in preferential chemical leaching of U and Th. Gieré *et al*. (2001) discussed that U^{6+} tends to be much more mobile than U^{4+} and U^{5+}. Correspondingly, Ervanne (2004) postulated that if uranium was present as U^{6+} in fergusonite, hydrothermal alteration should result in its chemical removal. The clearly higher mobility and leachability of U^{6+} on the one hand, and the absence of notable U leaching on the other hand, suggest that the alteration of our sample cannot have occurred in a strongly oxidising environment. The comparably low mobility of U during a fluid-driven alteration in the strongly radiation-damaged fergusonite from Madagascar supports previous suggestions to consider fergusonite-type materials for the immobilisation of nuclear waste (Gieré *et al*., 2009).

4. Conclusions

The fergusonite specimen from Madagascar investigated in the present study was found to be highly radiation-damaged, which corresponds to its high actinide (U and Th) concentrations. To the best of our knowledge, this is the first study that addresses in detail elemental changes in natural fergusonite that was affected by low-*T* hydrothermal overprint. However, several of our observations seem to contradict each other or are difficult to interpret: the mismatch of textures of the host material observed in the optical microscope (a fibrous-knotty appearance) and the BSE images (mostly straight zones, less often patchy), the porosity of the apparently ''primary'' host material (seen in the BSE and the HAADF images), and the virtual absence of pores in the altered areas. Therefore, further investigation of a larger number of hydrothermally altered samples of ABO_4-type minerals in the future is important, particularly in view of the uncertainty that only one specimen with a complicated alteration texture was analysed in the present study. Nevertheless, the results obtained here add to our knowledge on the behaviour of radiation-damaged fergusonite in a low-*T*, ''wet'' environment. The fluid-driven alteration was apparently controlled by the accessibility of micro-areas to the alteration fluid through large fractures, which seem to have served as ''fast migration pathways''. One of the most important observations is that relative changes in the U and Th contents are much less extensive than those of some other major or minor elements, such as Si, Ca, and most REEs. This suggests that the radionuclides are not necessarily leached-out preferentially in a fluid-driven replacement reaction affecting radiation-damaged fergusonite.

Acknowledgements: The fergusonite sample was kindly made available by Jochen Schlüter (Mineralogisches Museum der Universität Hamburg) and Christian Schnier (GKSS, Geesthacht). Thanks are due to Andreas Wagner (Universität Wien) and Anja Schreiber (Helmholtz-Zentrum Potsdam) for sample preparation. Constructive reviews by Juan Jiménez Millán and an anonymous expert are gratefully acknowledged. We are indebted to Fernando Nieto García for his editorial handling and helpful comments. Financial support was provided by the European Commission through contract no. MEXC–CT–2005–024878, and the Austrian Science Fund (FWF), grant P20028–N10, to L.N.

References

Armstrong, J.T. (1995): CITZAF: a package of correction programs for the quantitative electron microbeam X-ray-analysis of thick polished materials, thin films, and particles. *Microbeam Anal.*, **4**, 177–200.

Caruba, R., Baumer, A., Ganteaume, M., Iacconi, P. (1985): An experimental study of hydroxyl groups and water in synthetic and natural zircons: a model of the metamict state. *Am. Mineral.*, **70**, 1224–1231.

Ercit, T.S. (2005): Identification and alteration trends of granitic-pegmatite-hosted (Y,REE,U,Th)–(Nb,Ta,Ti) oxide minerals: a statistical approach. *Can. Mineral.*, **43**, 1291–1303.

Ervanne, H. (2004): Uranium oxidation states in allanite, fergusonite and monazite of pegmatites from Finland. *N. Jb. Mineral. Mh.*, **7**, 289–301.

Ewing, R.C. (1975): Alteration of metamict, rare-earth, AB_2O_6-type Nb–Ta–Ti oxides. *Geochim. Cosmochim. Acta*, **39**, 521–530.

Ewing, R.C. & Ehlmann, A.J. (1973): Yttrialite and uraninite, additional minerals from Rode Ranch pegmatite, Central Mineral Region, Texas. *Am. Mineral.*, **58**, 545–547.

—, — (1975): Annealing study of metamict, orthorhombic, rare earth, AB_2O_6-type, Nb–Ta–Ti oxides. *Can. Mineral.*, **13**, 1–7.

Förster, H.-J. (1998): The chemical composition of REE–Y–Th–U-rich accessory minerals in peraluminous granites of the Erzgebirge-Fichtelgebirge region, Germany, Part I: the monazite-(Ce)–brabantite solid solution series. *Am. Mineral.*, **83**, 259–272.

Geisler, T., Pöml, P., Stephan, T., Janssen, A., Putnis, A. (2005): Experimental observation of an interface-controlled pseudomorphic replacement reaction in a natural crystalline pyrochlore. *Am. Mineral.*, **90**, 1683–1687.

Gieré, R., Buck, E.C., Guggenheim, R., Mathys, D., Reusser, E., Marques, J. (2001): Alteration of Uranium-rich microlite. *Mater. Res. Soc. Symp. P.*, **663**, 935–944.

Gieré, R., Williams, C.T., Wirth, R., Ruschel, K. (2009): Metamict fergusonite-(Y) in a spessartine-bearing granitic pegmatite from Adamello, Italy. *Chem. Geol.*, **261**, 333–345.

Janeczek, J. (2004): Re-examination of kochelite: a mixture of metamict fergusonite-(Y) and altered zircon. *N. Jb. Mineral. Mh.*, **2005/5**, 193–207.

Libowitzky, E. & Rossman, G.R. (1996): Principles of quantitative absorbance measurements in anisotropic crystals. *Phys. Chem. Minerals*, **23**, 319–327.

—, — (1997): An IR absorption calibration for water in minerals. *Am. Mineral.*, **82**, 1111–1115.

Lumpkin, G.R. (1998): Rare-element mineralogy and internal evolution of the Rutherford #2 pegmatite, Amelia County, Virginia: a classic locality revisited. *Can. Mineral.*, **36**, 339–353.

Lumpkin, G.R. & Ewing, R.C. (1992): Geochemical alteration of pyrochlore group minerals: microlite subgroup. *Am. Mineral.*, **77**, 179–188.

—, — (1995): Geochemical alteration of pyrochlore group minerals: pyrochlore subgroup. *Am. Mineral.*, **80**, 732–743.

—, — (1996): Geochemical alteration of pyrochlore group minerals: betafite subgroup. *Am. Mineral.*, **81**, 1237–1248.

Lumpkin, G.R., Ewing, R.C., Williams, C.T., Mariano, A.N. (2001): An overview of the crystal chemistry, durability, and radiation damage effects of natural pyrochlore. *Mater. Res. Soc. Symp. P.*, **663**, 921–934.

Lumpkin, G.R., Smith, K.L., Gieré, R., Williams, C.T. (2004): Geochemical behaviour of host phases for actinides and fission products in crystalline ceramic nuclear waste forms. *in* ''Energy, Waste, and the Environment: a Geochemical Perspective'', R. Gieré & P. Stille, eds. Geological Society, London, Special Publications, 89–111.

Mathieu, R., Zetterström, L., Cuney, M., Gauthier-Lafaye, F., Hidaka, H. (2001): Alteration of monazite and zircon and lead migration as geochemical tracers of fluid paleocirculations around the Oklo–Okélobondo and Bangombé natural nuclear reaction zones (Franceville basin, Gabon). *Chem. Geol.*, **171**, 147–171.

Mücke, A. & Strunz, H. (1978): Petscheckite and liandratite, two new pegmatite minerals from Madagascar. *Am. Mineral.*, **63**, 941–946.

Nasdala, L., Beran, A., Libowitzky, E., Wolf, D. (2001): The incorporation of hydroxyl groups and molecular water in natural zircon ($ZrSiO_4$). *Am. J. Sci.*, **301**, 831–857.

Nasdala, L., Lengauer, C.L., Hanchar, J.M., Kronz, A., Wirth, R., Blanc, P., Kennedy, A.K., Seydoux-Guillaume, A.-M. (2002): Annealing radiation damage and the recovery of cathodoluminescence. *Chem. Geol.*, **191**, 121–140.

Nasdala, L., Kronz, A., Wirth, R., Váczi, T., Pérez-Soba, C., Willner, A., Kennedy, A.K. (2009): The phenomenon of deficient electron microprobe totals in radiation-damaged and altered zircon. *Geochim. Cosmochim. Acta*, **73**, 1637–1650.

Nasdala, L., Hanchar, J.M., Rhede, D., Kennedy, A.K., Váczi, T. (2010): Retention of uranium in complexly altered zircon: an example from Bancroft, Ontario. *Chem. Geol.*, **269**, 290–300.

Pointer, C.M., Ashworth, J.R., Ixer, R.A. (1988): The zircon-thorite mineral group in metasomatized granite, Ririwai, Nigeria. 2. Zoning, alteration and exsolution in zircon. *Mineral. Petrol.*, **39**, 21–37.

Poitrasson, F., Paquette, J.-L., Montel, J.-M., Pin, C., Duthou, J.-L. (1998): Importance of late-magmatic and hydrothermal fluids on the Sm–Nd isotope mineral systematics of hypersolvus granites. *Chem. Geol.*, **146**, 187–203.

Putnis, A. (2002): Mineral replacement reactions: from macroscopic observations to microscopic mechanisms. *Mineral. Mag.*, **66**, 689–708.

Putnis, A. (2009): Mineral replacement reactions. *Rev. Mineral. Geochem.*, **70**, 87–124.

Ruschel, K., Nasdala, L., Gaft, M., Schnier, C., Schlüter, J. (2007): Photoluminescence recovery upon annealing of fergusonite. *Geochim. Cosmochim. Acta*, **71**, A861.

Smith, D.G.W., de St. Jorre, L., Reed, S.J.B., Long, J.V.P. (1991): Zonally metamictized and other zircons from Thor Lake, Northwest Territories. *Can. Mineral.*, **29**, 301–309.

Tomašić, N., Gajović, A., Bermanec, V., Rajić, M. (2004): Recrystallization of metamict Nb–Ta–Ti–REE complex oxides: a coupled X-ray-diffraction and Raman spectroscopy study of aeschynite-(Y) and polycrase-(Y). *Can. Mineral.*, **42**, 1847–1857.

Tomašić, N., Gajović, A., Bermanec, V., Su, D.S., Rajić Linarić, M., Ntaflos, T., Schlögl, R. (2006): Recrystallization mechanisms of fergusonite from metamict mineral precursors. *Phys. Chem. Minerals*, **33**, 145–159.

Tomašić, N., Bermanec, V., Gajović, A., Rajić Linarić, M. (2008): Metamict minerals: an insight into a relic crystal structure using XRD, Raman spectroscopy, SAED and HRTEM. *Croat. Chem. Acta*, **81**, 391–400.

Váczi, T., Nasdala, L., Wirth, R., Mehofer, M., Libowitzky, E., Häger, T. (2009): On the breakdown of zircon upon ''dry'' thermal annealing. *Mineral. Petrol.*, **97**, 129–138.

Van Wambeke, L. (1970): The alteration processes of the complex titano-niobo-tantalates and their consequences. *N. Jb. Mineral. Abh.*, **112**, 117–149.

Wang, R.C., Fontan, F., Chen, X.M., Hu, H., Liu, C.S., Xu, S.J., de Parseval, P. (2003): Accessory minerals in the Xihuashan Y-enriched granitic complex, southern China: a record of magmatic and hydrothermal stages of evolution. *Can. Mineral.*, **41**, 727–748.

Wirth, R. (2004): Focused ion beam (FIB): A novel technology for advanced application of micro- and nanoanalysis in geosciences and applied mineralogy. *Eur. J. Mineral.*, **16**, 863–876.

Yashima, M., Lee, J.-H., Kakihana, M., Yoshimura, M. (1997): Raman spectral characterization of existing phases in the Y_2O_3–Nb_2O_5 system. *J. Phys. Chem. Solids*, **58**, 1593–1597.

Received 27 October 2009
Modified version received 12 February 2010
Accepted 12 March 2010

2.4 Phase Decomposition upon Alteration of Radiation-Damaged Monazite–(Ce) from Moss, Østfold, Norway

(2010)

Nasdala, L., Ruschel, K., Rhede, D., Wirth, R., Kerschofer-Wallner, L., Kennedy, A.K., Kinny, P.D., Finger, F. & Groschopf, N.

Chimia, 64:705–711

doi:10.2533/chimia.2010.705 Chimia 64 (2010) 705–711

Phase Decomposition upon Alteration of Radiation-Damaged Monazite–(Ce) from Moss, Østfold, Norway

Lutz Nasdala*[a], Katja Ruschel[a], Dieter Rhede[b], Richard Wirth[b], Ljuba Kerschhofer-Wallner[c], Allen K. Kennedy[d], Peter D. Kinny[e], Friedrich Finger[f], and Nora Groschopf[g]

Abstract: The internal textures of crystals of moderately radiation-damaged monazite–(Ce) from Moss, Norway, indicate heavy, secondary chemical alteration. In fact, the cm-sized specimens are no longer mono-mineral monazite but rather a composite consisting of monazite–(Ce) and apatite pervaded by several generations of fractures filled with sulphides and a phase rich in Th, Y, and Si. This composite is virtually a 'pseudomorph' after primary euhedral monazite crystals whose faces are still well preserved. The chemical alteration has resulted in major reworking and decomposition of the primary crystals, with potentially uncontrolled elemental changes, including extensive release of Th from the primary monazite and local redeposition of radionuclides in fracture fillings. This seems to question the general alteration-resistance of orthophosphate phases in a low-temperature, 'wet' environment, and hence their suitability as potential host ceramics for the long-term immobilisation of radioactive waste.

Keywords: Chemical alteration · Monazite–(Ce) · Radiation damage · Thorium silicate

1. Introduction

The accumulation of structural damage generated by the corpuscular self-irradiation of minerals containing actinide elements has been studied widely in the last decades. The bulk radiation damage is caused mainly by alpha-decay events: Recoil of the heavy daughter nuclei upon emission of a ^{4}He core generate nm-sized damage clusters, whose overlapping inter-connection at high densities may lead eventually to the formation of a non-crystalline form.[1,2] Such normally crystalline, irradiation-amorphised minerals are commonly described by the term 'metamict'.[3] The metamictisation process is controlled strongly by the proportion of the rates of damage accumulation and damage annealing; the latter being strongly temperature-dependent.[4,5] Whether or not a certain mineral becomes metamict is consequently not only controlled by the mineral phase itself and the amount of radioactivity it experienced since the time of its growth, but also by its thermal history.

The metamictisation of minerals results in dramatic changes of their physical properties, including volume swelling and potentially subsequent fracturing,[6] a general decrease in elastic properties and hardness,[7] and a change in optical properties[8] (*i.e.* refraction and birefringence). Further, the chemical resistance of metamictised minerals is generally decreased, *i.e.* such materials show enhanced solubility for instance under conditions of near-surface weathering,[9] and enhanced susceptibility to secondary loss of radiogenic isotopes.[10] Knowledge of the self-irradiation behaviour of minerals and their associated property changes are hence of enormous relevance for the Earth sciences (*e.g.* petro-geochemistry and U–Pb geochronology) and the materials sciences (*e.g.* mineral-based matrices for conditioning radionuclides in radioactive waste repositories).[11] In view of the latter, key problems to be studied include i) the susceptibility of materials to undergo chemical alteration, and its increase with cumulative radiation damage, ii) how exactly chemical alteration processes take place, and iii) as to which degree these materials (*i.e.* unaltered and/or altered specimens) can resist the release of radionuclides. The investigation of chemically altered, radiation-damaged minerals is, therefore, motivated strongly by the question, how such materials perform in a low-temperature, 'wet' geological environment over extended periods of time.

2. Material and Methods

2.1 *Sample and Preparation*

We have investigated monazite crystals from a granite pegmatite located at the island of Dillingøya (lake Vannsjø), just east of the city of Moss, Østfold district, southeastern Norway.[12] The area of origin belongs to the Riphean[13] (which, according to recent timescales of the International Commission of Stratigraphy, corresponds to the Meso- to Neoproterozoic). The monazite crystals are 2–2.5 cm large. They are medium to dark brownish, of thick-tabular habit, and have well-shaped faces with slightly rounded edges.

The monazite crystals were cut through the middle, along their longest dimension, and polished thin sections (~30 µm thickness) attached to a glass slide were prepared. These sections were used for optical microscopy, electron probe micro-analyser (EPMA) investigation, and micro-Raman spectroscopy. Sections were coated with

*Correspondence: Prof. Dr. L. Nasdala[a]
Tel.: +43 1 4277 53220
Fax: +43 1 4277 9532
E-mail: lutz.nasdala@univie.ac.at
[a]Institut für Mineralogie und Kristallographie, Universität Wien
Althanstrasse 14, A–1090 Wien, Austria
[b]Helmholtz-Zentrum Potsdam, Deutsches GeoForschungsZentrum
Telegrafenberg, D–14473 Potsdam, Germany
[c]BWI Informationstechnik GmbH
Balanstr. 73, D–81541 München, Germany
[d]Department of Applied Physics, Curtin University of Technology
Building 301, Kent Street, Bentley, WA 6102, Australia
[e]Department of Applied Geology, Curtin University of Technology
Building 312, Kent Street, Bentley, WA 6102, Australia
[f]Fachbereich Materialforschung und Physik, Universität Salzburg
Hellbrunnerstrasse 34, A–5020 Salzburg, Austria
[g]Institut für Geowissenschaften, Universität Mainz
Johann-Joachim-Becher-Weg 21, D–55099 Mainz, Germany

carbon prior to EPMA imaging and analysis. For Sensitive High mass-Resolution Ion MicroProbe (SHRIMP) analysis, small chips of the sample were, together with the SHRIMP reference MAD–1, embedded in araldite epoxy, and flat polished sample mounts were prepared and coated with gold. For transmission electron microscopy (TEM), electron-transparent foils were prepared by conventional hand-polishing and Ar ion milling at 5 kV. The TEM foils were then coated with carbon.

2.2 *Experimental Details*

The thin sections were first examined and imaged under an optical binocular, in plane-polarised and cross-polarised transmitted light. Raman spectra were obtained in quasi-backscatter geometry using an edge filter-based Renishaw RM1000 system equipped with Leica DMLM optical microscope (50 objective, numerical aperture 0.75) and Peltier-cooled, Si-based charge-coupled device (CCD) detector. Spectra were excited with the 632.8 nm emission of a He–Ne laser. The laser power at the sample surface was ~8 mW, which is well below the threshold for any local sample changes due to intense light absorption. The system was operated in the quasi-confocal mode, resulting in a lateral resolution of ~4–5 µm. Band positions were calibrated using the Rayleigh line and neon lamp emission lines. The wavenumber accuracy was better than 1 cm^{-1}, and the spectral resolution was ~3–4 cm^{-1}.

The chemical composition was determined by means of wavelength-dispersive X-ray spectroscopy (WDS) analysis in a JEOL JXA 8900 RL EPMA. The accelerating voltage was 15 kV and the beam current was 50 nA. The focal spot area of the electron beam had a diameter of <1 µm. Calibration standards used were well-characterized natural and synthetic materials, including YAG (Al, Y), wollastonite (Si), monazite (P), Fe_2O_3 (Fe), $CeAl_2$ (Ce), REE silicate glasses (lanthanides except Ce), crocoite (Pb), Th metals (Th), and UO_2 (U). The CITZAF routine in the JEOL software, which is based on the Φ(ρZ) method,[14] was used for data processing. The results were corrected for rare-earth element (REE) peak overlaps. Back-scattered electron (BSE) imaging, and high-resolution element mapping, were done using a JEOL JXA–8500F thermal field emission-type EPMA. The element distribution maps[15] were obtained in WDS mode with an acceleration voltage of 6 kV, a probe current of 40–50 nA, and a dwell time of 0.25–0.40 s per step (stage step intervals 0.1–0.3 µm).

Transmission electron microscopy – including electron diffraction, bright field (BF) and dark field (DF) imaging, and high-resolution electron microscopy (HREM) imaging – was done using a JEOL 3010 system equipped with LaB6 cathode, and a PHILIPS CM200 system equipped with EDAX X-ray analyser and GATAN imaging filter. The systems were operated at a voltage of 300 kV (JEOL) and 200 kV (PHILIPS), respectively.

Analyses of the U–Th–Pb isotopic composition were done using a SHRIMP II at the Department of Applied Physics, Curtin University of Technology, Perth.[16] The monazite surface was sputtered with a primary, mass-filtered $(O_2)^-$ beam with ~1 nA current, focused to a ~7–10 µm spot. The SHRIMP was operated with a mass resolution (M/ΔM) better than 5000. The sensitivity for Pb isotopes was about 20 counts per second per ppm, per nA. A single analysis consisted of seven scans. Data for each spot were collected in sets of seven scans through the mass range of $^{202}LaPO_2$, $^{203}CePO_2$, ^{204}Pb, background near ^{204}Pb, ^{206}Pb, ^{207}Pb, ^{208}Pb, ^{232}Th, ^{238}U, $^{248}ThO_2$, and $^{270}UO_2$. The total analytical time was *ca.* 16 min per spot. Results were calibrated against MAD–1, a 514 Ma old reference monazite. The ^{204}Pb method was employed for the correction for non-radiogenic Pb.[17,18]

3. Results and Discussion

3.1 *Alteration Textures and Chemical Composition*

Transmitted light and BSE images reveal that the monazite crystals have a remarkably heterogeneous internal texture (Fig. 1). In contrast to the macroscopic appearance of a single-crystal, the material consists of several phases. The specimens are apparent 'pseudomorphs' after primary monazite crystals whose macroscopic crystal shapes are still well-preserved (Fig. 1a), even though they are actually a very heterogeneous composite of phases. The dominant monazite (transparent with pale brownish colour, medium BSE intensity) is inter-grown closely with patches of apatite

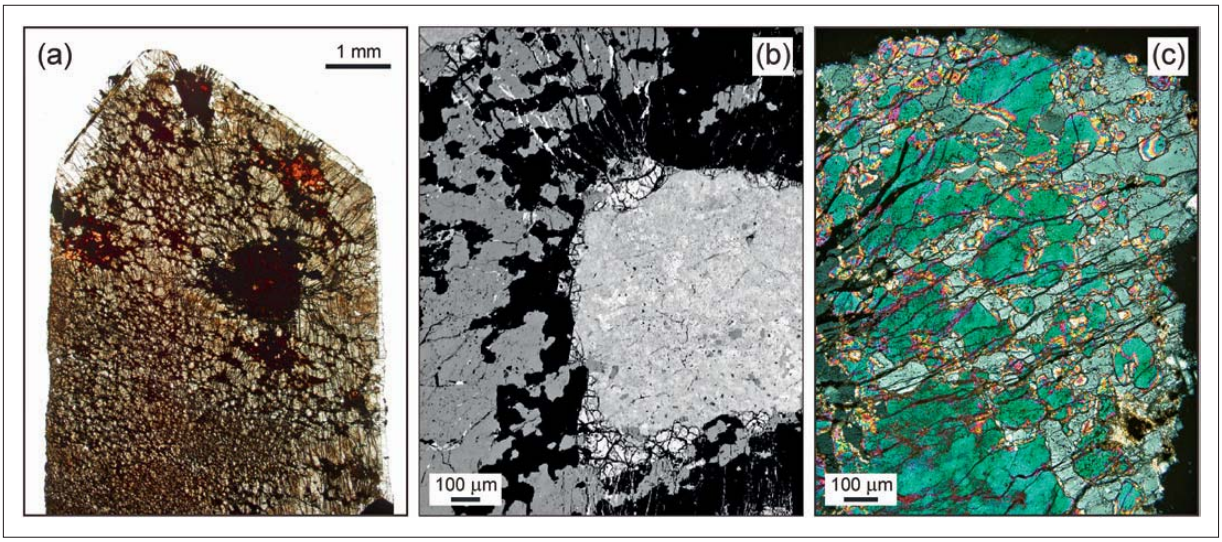

Fig. 1. (a) Photomicrograph of one of the monazite–(Ce) samples (30 µm thin section, transmitted plane-polarised light), revealing its secondary, multi-phase texture. The material is virtually a 'pseudomorph' of a multi-phase composite after a monazite crystal. Note the myriad of fractures emanating from 'nests' consisting of a Th- and Fe-rich material (dark reddish-brown). (b) BSE image, showing one of the 'nests' (centre, bright) that is surrounded by Ca apatite (black; the monazite appears medium gray). (c) Photomicrograph (transmitted cross-polarised light) of the patchy intergrowth of monazite–(Ce) (green interference colour) with apatite (grey interference colour).

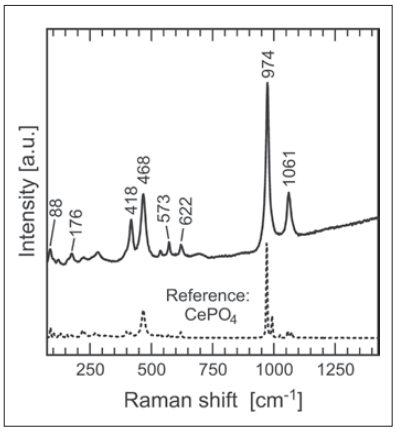

Fig. 2. Raman spectrum of the monazite–(Ce) compared to that of synthetic $CePO_4$.

(colourless, low BSE intensity; Fig. 1a), and a few scattered 'nest'-like patches of a heterogeneous, Th- and Fe-rich material (predominantly hematite; reddish brown, high BSE intensity; Fig. 1b). The phosphate–iron oxide assemblage is pervaded by a network of numerous cracks and fractures up to several tens of µm in thickness, with heterogeneous fracture fillings. The fractures have mostly random orientation but may show a radial pattern around the 'nests', pointing to volume expansion of the Th- and Fe-rich material. In some cases, crystals show a narrow apatite rim (Fig. 1a).

Table 1. Chemical composition of the monazite–(Ce). All values are quoted in wt%.

Oxide	Mean	Range
Al_2O_3	0.0	0.0–0.2
SiO2	1.0	0.7–1.5
P_2O_5	28.8	28.2–29.4
CaO	1.1	0.8–1.7
FeO	0.2	0.0–1.2
Y_2O_3	0.7	0.5–1.0
La_2O_3	8.7	7.6–9.4
Ce_2O_3	25.3	22.4–27.3
Pr_2O_3	3.4	2.9–3.8
Nd_2O_3	12.7	11.2–13.8
Sm_2O_3	6.9	6.3–7.4
Gd_2O_3	3.2	2.8–3.4
Dy_2O_3	0.5	0.2–0.6
Ho_2O_3	0.0	0.0–0.1
PbO	0.4	0.2–1.1
ThO2	6.1	3.7–10.8
UO_2	0.1	0.0–0.3
Σ	99.1	98.3–100.4

In cross-polarised light, the monazite shows high 2nd order to low 3rd order interference colours (Fig. 1c), which corresponds to birefringence in the range 0.028–0.045. The notable but still moderate birefringence depletion, compared to well-crystallised monazite, suggests moderate levels of accumulated radiation damage. The extinction behaviour of the monazite is uniform over large area ranges on the order of millimetres; the same is true for the apatite (*cf.* Fig. 1c). This suggests an oriented (*i.e.* topotaxial) inter-growth of the two phosphate phases.

The mineral phases were identified from their patterns of Raman-active bands. As expected, the vibrational bands of the monazite Raman spectrum correspond to monoclinic $REE[PO_4]$ (*cf.* Fig. 2); however, they show general but still moderate broadening. For instance, the $\nu_1(PO_4)$ band near 974 cm^{-1} has a full width at half maximum (FWHM) of ~13–14 cm^{-1}, which indicates a mildly to moderately radiation-damaged structure.[19] Further mineral phases identified from Raman spectra include fluorapatite $[Ca_5(PO_4)_3F]$, hematite (Fe_2O_3), pyrite (FeS_2), galena (PbS), xenotime (YPO_4), and huttonite ($ThSiO_4$).

The main monazite phase shows a relatively heterogeneous composition (*cf.* ranges quoted in Table 1; *cf.* also BSE image and Fe and Th maps in Fig. 3). The average composition corresponds to the formula $(REE_{0.88}\ Th_{0.05}\ Ca_{0.05}\ Fe_{0.01})\ (P_{0.97}\ Si_{0.04})\ O_4$ (with $REE_{0.88} = Ce_{0.37}\ Nd_{0.18}\ La_{0.13}\ Sm_{0.09}\ Pr_{0.05}\ Gd_{0.04}\ Y_{0.01}\ Dy_{0.01}$). Due to the dominance of Ce at the medium-sized cation position, this mineral is to be called monazite–(Ce). The apatite is relatively homogeneous, pure Ca-phosphate without any non-formula elements in the wt% range. In contrast, the fillings of fractures

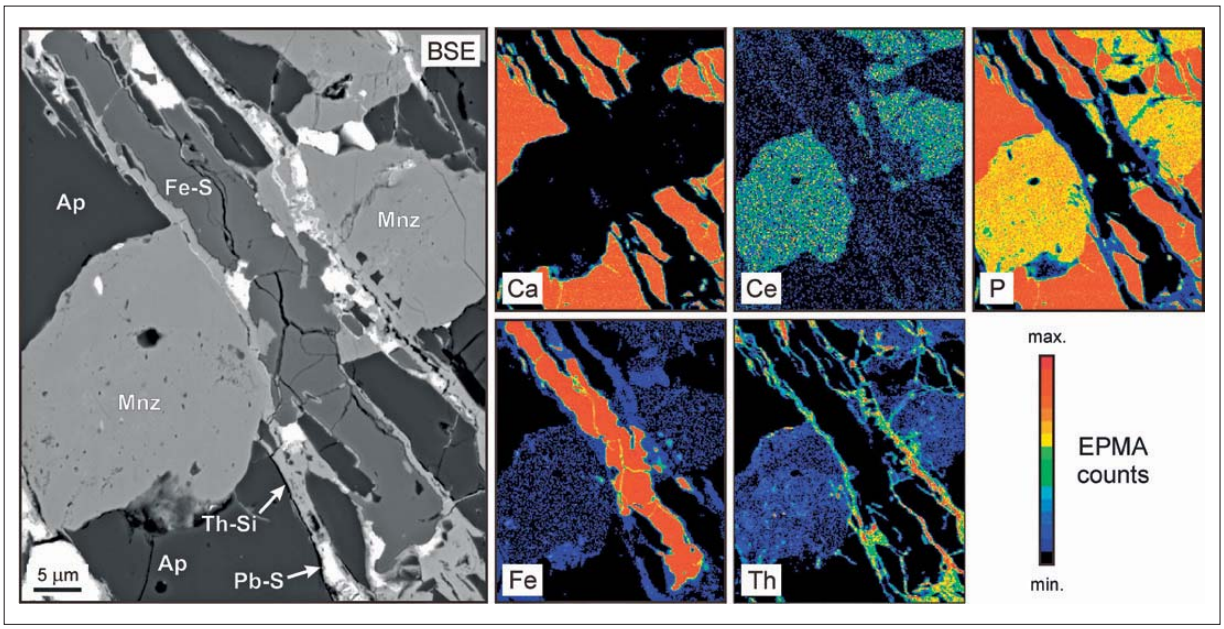

Fig. 3. BSE image, and series of five colour-coded EPMA element distribution maps (6 kV; 4×10^{-8} A; dwell time 0.4 s; step width 0.3 µm) obtained from the same area. In the BSE image, large areas of monazite–(Ce) (Mnz) and apatite (Ap) appear medium gray and nearly black, respectively. These two phosphate phases are inter-grown with veins consisting of Fe sulphide (Fe-S; dark grey), Pb-sulphide (Pb-S; nearly white), and Th-silicate (Th-Si; medium grey). Colour-coded EPMA intensity ranges (given in counts) are 8–339 (Ca), 1–16 (Ce), 12–516 (P), 63–1919 (Fe), 4–142 (Th).

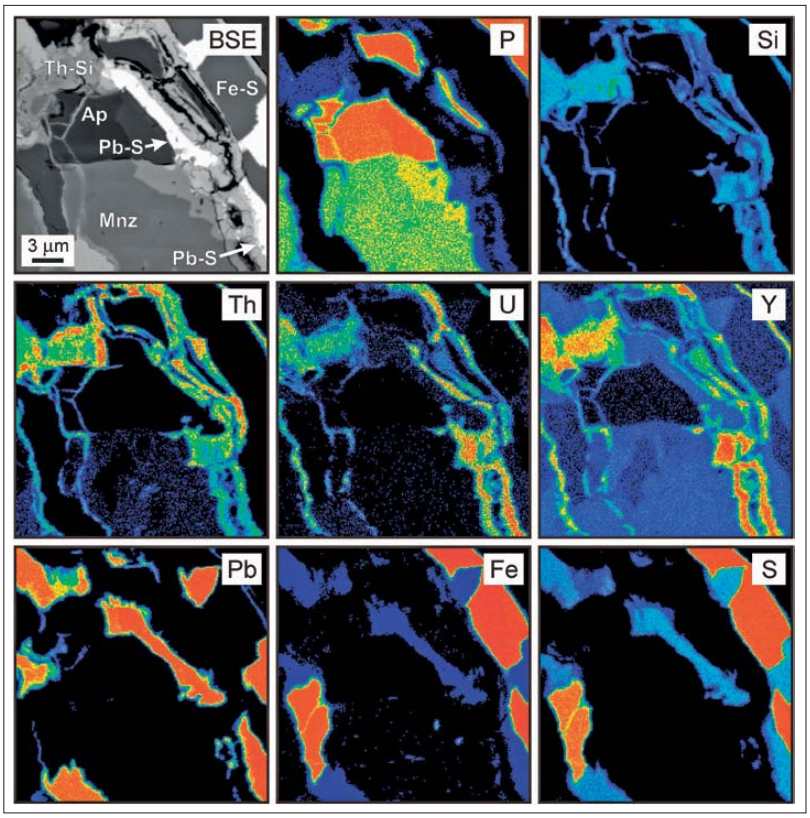

Fig. 4. BSE image showing a close-up of veins cross-cutting the two bulk phosphates, and corresponding series of eight colour-coded element distribution maps (6 kV; 5×10^{-8} A; dwell time 0.4 s; step width 0.1 µm). Colour-coded EPMA intensity ranges (given in counts) are 10–465 (P), 3–199 (Si), 5–168 (Th), 2–59 (U), 15–243 (Y), 13–592 (Pb), 83–1758 (Fe), 16–542 (S).

pervading the two bulk phosphates are most heterogeneous in composition (Fig. 3). Apparently there are several 'generations' of veinlets. The central fillings are dominated typically by Fe-sulphide (*i.e.* pyrite) whereas towards the rims of fractures there is Pb-sulphide (*i.e.* galena; bright BSE) associated with a Th-rich phase (*cf.* Fe and Th distribution maps in Fig. 3).

The distribution patterns of several elements discussed are shown at higher resolution in Fig. 4. In fractures there are large pyrite (red in the Fe and S maps) and galena grains (red in the Pb and pale blue in the S map). The Th-rich phase, which seems to be the youngest, may occupy much smaller fractures. Phosphorous and the REEs are depleted appreciably in these Th-rich veinlets, compared to the bulk monazite–(Ce) (Fig. 3). Apart from a clear enrichment in Th (which may exceed 50 wt% in single spots) and Si, there is also an enrichment in Fe, Y, and U. However, element ratios are non-uniform (note the clear differences between the Th map on the one hand and the U and Y maps on the other hand in Fig. 4). Obviously the Th-rich veinlets do not represent one mineral phase but consist of a heterogeneous assemblage of several phases with different compositions.

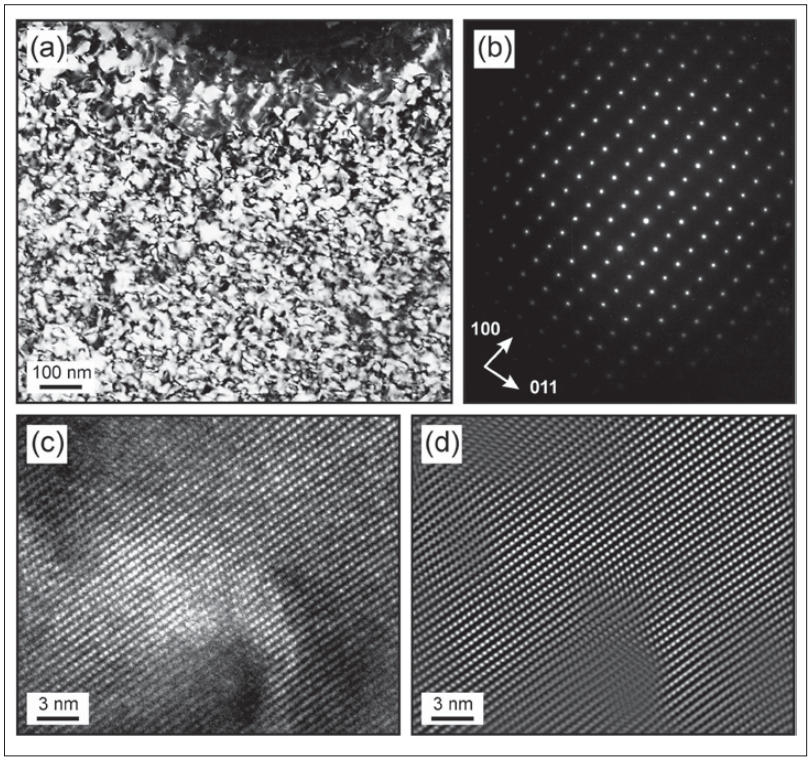

Fig. 5. TEM results for the bulk monazite. (a) Dark field image (diffracting vector g = 311) showing mottled contrast. (b) Electron diffraction pattern obtained along [0$\bar{1}$1]. (c) HREM lattice fringe image (viewed along [010]). (d) Fourier-filtered version of the same image. Note the absence of aperiodic regions.

3.2 *Transmission Electron Microscopy*

Dark-field images of the monazite show mottled contrast (Fig. 5a), which is assigned to a mosaic-like domain texture (*i.e.* volume regions with slightly varying orientation) resulting from self-irradiation damage.[19,20] The degree of misorientation and the volume fraction of distorted regions in our sample are not extensive, because sharp maxima were observed in the electron diffraction patterns (Fig. 5b). The domain texture is also recognised in high-resolution lattice-fringe images (Figs. 5c–d) showing well-ordered, periodic lattice regions up to a few tens of nanometres in size, bracketed by slightly confused boundary regions. These observations suggest that the monazite represents a moderate degree of accumulated self-irradiation damage,[21] which also corresponds well with the still high interference colours (Fig. 1c) and the moderate broadening of Raman bands (Fig. 2).

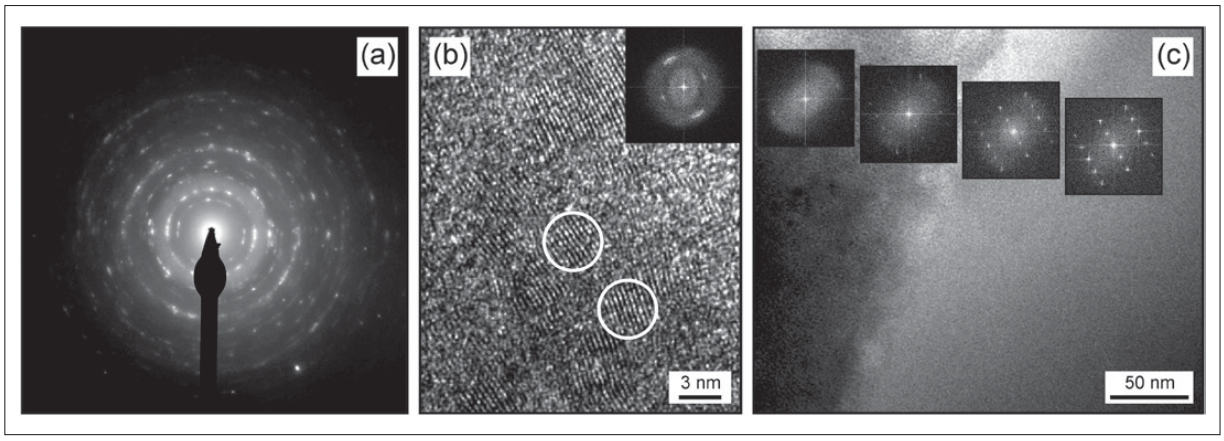

Fig. 6. TEM results (continued). (a) Electron diffraction pattern of a Th-rich veinlet, indicating the polycrystalline nature of the material. (b) HREM image of the Th-silicate phase. Two of the nanometre-sized 'crystalline islands' having different orientation are marked with white circles. The corresponding FFT electron-diffraction pattern (inset) shows strongly broadened maxima. (c) Bright-field image of the apatite in close proximity to a Th-silicate vein (located on the left, just outside the image area). The positions of the four insets correspond roughly to the locations where the FFT electron-diffraction patterns were obtained. Note the gradual loss of apatite crystallinity toward the Th-silicate.

The Th-rich phase, occurring as outer fracture filling in the veinlets (*cf.* BSE image and Th map in Fig. 3), shows a more diverse appearance in the TEM. Electron diffraction patterns obtained from sample volumes of more than a few nanometres in size are characterized by coarse rings of broadened diffraction maxima, which are overlaid by an always notable, diffuse 'amorphous ring' (Fig. 6a). This suggests that the Th-rich material is partially amorphous and partially crystalline, hence probably containing several phases. The crystalline volume fraction must be polycrystalline, consisting of a multitude of tiny crystals (or better, ordered volume regions) with slightly different orientations. The rotation of the crystalline volume regions can be observed in high-resolution lattice-fringe images (Fig. 6b); this phenomenon is due to local strain as induced by the amorphisation.[2]

In high-resolution electron-diffraction patterns of the Th-rich material, generated through fast Fourier-transformation (FFT) of HREM images, diffraction maxima show in some cases clear broadening (for instance, *cf.* inset in Fig. 6b). The d-spacings calculated from FFT electron-diffraction patterns point to a decidedly heterogeneous material. A set of d-values of ~0.47 and ~0.36 nm may be assigned to the (101) and (200) of zircon-structured $ThSiO_4$ (*i.e.* thorite), whereas ~0.42, ~0.33, ~0.31, and ~0.29 nm correspond to the $(\bar{1}11)$, (200), (120), and (012) of monazite-structured $ThSiO_4$ (*i.e.* huttonite). A set of d-values of ~0.33 and ~0.28 nm may perhaps even indicate the additional presence of cubic ThO_2 (*i.e.* thoriantite), as they correspond reasonably well with the (111) and (200) of this mineral; there is, however, some potential overlap with huttonite (*cf.* above). These observations suggest a moderate to high level of accumulated radiation damage in the Th-silicate veinlets, which has, however, remained well below the level of complete amorphisation. The notably heterogeneous phase composition of the Th-rich veinlets seems to agree well with their chemical heterogeneity discussed above and may point to a non-homogeneous (*i.e.* multi-step) formation process of the veinlet material.

An interesting observation was made for the Ca apatite. The bulk of this phase is in the crystalline state, without mottled contrast in BF images or any other indication of low levels of radiation damage. The situation is different, however, in the case of apatite that is located in close proximity to Th-rich veinlets (*i.e.* up to ~150 nm away from the veinlet–apatite boundary). Toward the Th-rich veinlets, the apatite is increasingly damaged, up to complete amorphisation (Fig. 6c). The damaged/amorphised zone is interpreted as alpha-recoil halo,[22,23] *i.e.* the damage in the apatite was generated mainly by recoils of heavy nuclei originating from the high Th content in the neighbouring veinlet material.

3.3 *Geo-Chronological Considerations*

An attempt was made to determine the age of the monazite–(Ce) formation and/or the time of its alteration using SHRIMP U–Th–Pb measurements. However, the material turned out to be virtually 'undatable': Even though all measurements were placed carefully in apparently crack-free material, the isotope ratios obtained show extensive scatter and are tainted with huge uncertainties, resulting in calculated $^{207}Pb/^{206}Pb$ ages for single measurements with 2σ errors as high as several hundred Ma (average 1027±221 Ma; Table 2). This may first be due to the hypothetical presence of scattered, sub-micrometre sized Pb-rich domains in radiation-damaged monazite.[24] Most importantly, our monazite–(Ce) sample contains varying but generally very high concentrations of common Pb (*cf.* f 206 values in Table 2), resulting in very large ^{204}Pb corrections to the isotopic ratios and hence increased uncertainties. In addition to the introduction of common Pb, the U–Th–Pb isotopic system also seems to be affected by secondary loss of the radiogenic Pb. This is indicated by significantly discordant isotope ratios (Table 2).

Following the method of Montel *et al.*,[25] we attempted also to calculate monazite U–Th–Pb ages from EPMA results. Measurements in carefully selected, apparently unaltered areas of the monazite–(Ce) yielded an average 'age' of 788±34 Ma (2σ).

Both of the above two age values are uncertain, and none of them is considered to be a realistic age, because of the isotopic ratios being biased notably by the disturbance of the U–Th–Pb system (in particular Pb loss and Pb gain) during the alteration. The high fraction of common Pb indicates that significant amounts of Pb were incorporated during the alteration. This conclusion agrees very well with elevated concentrations of Pb (partly occurring as PbS) in the secondary fracture fillings (*cf.* Pb and S maps in Fig. 4), which has been observed similarly by Poitrasson *et al.*[26] Even in view of the uncertainties, the U–Th–Pb elemental and isotopic ratios obtained point to a Proterozoic (*i.e.* Meso- to Neoproterozoic) age. It could either be assigned to the primary pegmatitic growth

Table 2. SHRIMP data for the monazite–(Ce) from Moss, Norway. All errors represent 2σ uncertainties

(a) Measured isotope ratios (not corrected for common Pb):

Spot	$^{204}Pb/^{206}Pb$	$^{207}Pb/^{206}Pb$	$^{208}Pb/^{206}Pb$	$^{206}Pb/^{238}U$	$^{207}Pb/^{235}U$
1	0.00691±0.00080	0.172±0.004	106.0±1.1	0.175±0.053	4.17±1.28
2	0.00429±0.00031	0.125±0.001	71.3±0.4	0.0827±0.0013	1.419±0.029
3	0.0176±0.0007	0.328±0.006	44.6±0.6	1.076±0.034	48.7±1.9
4	0.00250±0.00017	0.114±0.001	23.9±0.1	0.192±0.003	3.00±0.05

(b) Data corrected for common Pb (^{204}Pb method):

Spot	f 206[a] [%]	$^{206}Pb/^{238}U$	$^{206}Pb/^{236}U$ age [Ma]	$^{207}Pb/^{235}U$	$^{207}Pb/^{235}U$ age [Ma]	$^{207}Pb/^{206}Pb$	$^{207}Pb/^{206}Pb$ age [Ma]	Disc.[b] [%]
1	11.0	0.156±0.047	934±262	1.61±0.61	973±243	0.075±0.015	1065±404	12
2	6.8	0.0770±0.0012	478±7	0.667±0.059	519±36	0.0629±0.0053	704±180	32
3	28.2	0.773±0.027	3691±99	8.48±1.95	2282±212	0.080±0.018	1187±453	–211
4	4.0	0.184±0.003	1088±14	1.98±0.09	1108±29	0.0782±0.0030	1151±77	5

[a] f 206 = common ^{206}Pb / total ^{206}Pb, from the observed ^{204}Pb
[b] U–Pb discordance; ratio of the ^{204}Pb-corrected $^{206}Pb/^{238}U$ and $^{207}Pb/^{206}Pb$ ages

of the monazite–(Ce) [this interpretation is supported by the monazite's chemical composition (relatively high concentrations of intermediate REEs) and EPMA totals of close to 100 wt% (Table 1)[27]] or be interpreted as a metasomatic overprint age (supported by the high common Pb).

Assuming a ~1000 myr damage accumulation period for the host monazite–(Ce), and based on its Th and U concentrations (Table 1), an average time-integrated alpha fluence[5,28] of $\sim 4.5 \times 10^{19}$ g^{-1} is calculated. Even in view of the strong uncertainty of the age that was used to calculate this fluence, the value calculated surpasses appreciably the alpha dose of $<1 \times 10^{19}$ α/g^{-1} that is needed for the complete amorphisation of solids.[2] Consequently, if all of the alpha-event damage experienced over a ~1000 myr time period was stored, our sample should be amorphous. By contrast, the bulk monazite–(Ce) is found to be only mildly to moderately radiation-damaged, hence obviously representing a comparably low degree of damage accumulation. This observation indicates extensive thermal annealing experienced by the Moss monazite (which in turn is completely consistent with the general observation that natural monazite, which undergoes thermal annealing at comparably low temperatures, virtually never becomes fully metamict[19,24]).

4. Concluding Remarks

The partial replacement of monazite by secondary apatite is commonly observed,[29] however, the opposite situation, *i.e.* secondary monazite occurring within apatite, is also a well-known phenomenon.[30,31] A rather special case was reported by Seydoux-Guillaume *et al.*[32] and Hetherington and Harlov[33] who found Th-rich monazite to have decomposed into Th-poor monazite and Th-silicate, without the presence of any apatite, however with alteration textures largely similar to those observed in this present study. It has been observed more often that a secondary Th–Si phase (or, more correctly, a heterogeneous phase assemblage rich in Th and Si) is formed upon decomposition of monazite to form apatite.[25,34,35] In such cases, the secondary apatite occurs mostly as microscopic, fine-grained overgrowth rim or interspace filling, with the Th-rich phase being located in close proximity. Our sample seems to be analogous, however, with an unusually high degree of phase separation: The apatite is crystallographically homogeneous on a comparably large scale (Fig. 1c), indicating a close topotactic relationship[30,36] with monazite, and it occurs relatively well separated from the Th–Si phase, which is located in fractures. The occurrence of a significant volume fraction of apatite within the monazite–(Ce) suggests that the alteration fluid was rich in F.

As early as one century ago, it has been discussed that a notable portion of the radioactivity in monazite from Moss, Norway, may arise from included Th-silicate.[37] However, it was also found that the excess Th cannot, at least not solely, be present in the form of $ThSiO_4$, because of variable, and mostly too low, Si/Th ratios.[38] Our observations support the presence of a heterogeneous secondary phase rich in Th and Si, and characterise the 'monazite crystals' from Moss as poly-phase 'pseudomorphs' with a complex chemical and thermal post-growth alteration history. In view of sharp boundaries and the extremely low volume diffusion of Th in monazite,[39] the alteration is assigned to a fluid-driven dissolution and 'pseudomorphisation' process[40] which released the Th into the alteration fluid. This was followed by re-deposition in the form of Th-rich phases (however, these phases grew obviously only after the formation of Fe- and Pb-sulphides in the fractures). The clear textural separation of Th-free Ca-apatite and Th-rich fracture fillings observed may indicate a multi-step alteration involving secondary Th depletion and tertiary Th enrichment (the latter being connected with the incorporation of common Pb).

Our observations reconfirm that under conditions of fluid-driven alteration and/or low-grade metamorphism, monazite may undergo very complex chemical alteration. The susceptibility to such alteration (and hence the probability for the release of radionuclides) does not only depend on the alteration fluid[25] but may be enhanced potentially by the accumulation of self-irradiation damage. It has been discussed by Read *et al.*[35] that this may have important implications for the chemically similar Pu^{4+}, questioning the suitability of monazite-structured orthophosphates as ceramics for the long-term immobilisation of radionuclides under the potentially 'wet', low-temperature conditions of waste repositories.

Acknowledgements

The sample was kindly made available by A. Massanek from the mineral collection of TU Bergakademie Freiberg, Germany. We are most grateful to D. Dettmar (Bochum), K. Paech (Potsdam), and A. Wagner (Wien) for sample preparation. Thanks are due to H.-J. Berg and F. Corfu (Oslo) for literature advice and helpful comments on the occurrence of monazite in southern Norway, and to A.-M. Seydoux-Guillaume for fruitful discussions

on problems related to monazite alteration. The manuscript benefited from constructive comments by I. Broska and P. Uher (Bratislava), K. Mezger (Bern), and an anonymous expert. L.N. is indebted to W. Hofmeister (Mainz) and W. Heinrich (Potsdam) for financial support during the early stages of this research. Partial funding was provided by the German Research Council (DFG), grant Na284/2–1, the European Commission trough contract no. MEXC–CT–2005–024878, and the Austrian Science Fund (FWF), grants P20028–N10 to L.N. and P22408 to F.F.

Received: July 30, 2010

[1] a) P. J. Wasiliewski, F. E. Senftle, J. E. Vaz, A. N. Thorpe, C. C. Alexander, *Rad. Effects.* **1973**, *17*, 191; b) W. J. Weber, R. C. Ewing, C. R. A. Catlow, T. D. de la Rubia, L. W. Hobbs, C. Kinoshita, H. Matzke, A. T. Motta, M. Nastasi, E. K. H. Salje, E. R. Vance, S. J. Zinkle, *J. Mater. Res.* **1998**, *13*, 1434; c) S. X. Wang, L. M. Wang, R. C. Ewing, *Phys. Rev. B* **2001**, *63*, 41051; d) R. C. Ewing, W. J. Weber, J. Lian, *J. Appl. Phys.* **2004**, *95*, 5949, and references therein.

[2] W. J. Weber, R. C. Ewing, L.-M. Wang, *J. Mater. Res.* **1994**, *9*, 688.

[3] a) W. C. Brøgger, *Z. Kryst. Mineral.* **1895**, *25*, 427; b) R. C. Ewing, *Nucl. Instrum. Meth. B* **1994**, *91*, 22; c) E. K. H. Salje, J. Chrosch, R. C. Ewing, *Am. Mineral.* **1999**, *84*, 1107.

[4] a) A. Meldrum, L. A. Boatner, R. C. Ewing, *Phys. Rev. B* **1997**, *56*, 13805; A. Meldrum, L. A. Boatner, R. C. Ewing, *Miner. Mag.* **2000**, *64*, 183; c) L. Nasdala, P. W. Reiners, J. I. Garver, A. K. Kennedy, R. A. Stern, E. Balan, R. Wirth, *Am. Mineral.* **2004**, *89*, 219.

[5] L. Nasdala, M. Wenzel, G. Vavra, G. Irmer, T. Wenzel, B. Kober, *Contrib. Mineral. Petrol.* **2001**, *141*, 125.

[6] a) L. W. Hobbs, F. W. Clinard, S. J. Zinkle, R. C. Ewing, *J. Nucl. Mater.* **1994**, *216*, 291; b) J. K. W. Lee, J. Tromp, *J. Geophys. Res.* **1995**, *100*, 17753.

[7] a) H. Özkan, *J. Appl. Phys.* **1976**, *47*, 4772; b) B. C. Chakoumakos, W. C. Olivier, G. R. Lumpkin, R. C. Ewing, *Radiat. Eff. Defect. S.* **1991**, *118*, 393; c) W. C. Olivier, J. C. McCallum, B. C. Chakoumakos, L. A. Boatner, *Radiat. Eff. Defect. S.* **1994**, *132*, 131.

[8] B. C. Chakoumakos, T. Murakami, G. R. Lumpkin, R. C. Ewing, *Science* **1987**, *236*, 1556.

[9] a) R. C. Ewing, R. F. Haaker, W. Lutze, in 'Scientific basis for radioactive waste management, 5', Ed. W. Lutze, Elsevier, Amsterdam, **1982**, p. 389; b) E. Balan, D. R. Neuville, P. Trocellier, E. Fritsch, J.-P. Muller, G. Calas, *Am. Mineral.* **2001**, *86*, 1025.

[10] a) L. T. Silver, S. Deutsch, *J. Geol.* **1963**, *71*, 721; b) L. Nasdala, R. T. Pidgeon, D. Wolf, G. Irmer, *Mineral. Petrol.* **1998**, *62*, 1; c) N. G. Rizvanova, O. A. Levchenkov, A. E. Belous, N. I. Bezmen, A. V. Maslenikov, A. N. Komarov, A. F. Makeev, L. K. Levskiy, *Contrib. Mineral. Petrol.* **2000**, *139*, 101; d) D. W. Davis, T. E. Krogh, *Chem. Geol.* **2000**, *172*, 41, e) R. Romer, *Contrib. Mineral. Petrol.* **2003**, *145*, 481.

[11] a) R. C. Ewing, *Can. Mineral.* **2001**, *39*, 697; b) G. R. Lumpkin, *Elements* **2006**, *2*, 365.

[12] a) W. C. Brøgger, *Geol. Fören. Stock. För.* **1881**, *5*, 326; b) W. C. Brøgger, 'Die Mineralien der südnorwegischen Granitpegmatitgänge. I. Niobate, Tantalate, Titanate und Titanoniobate', *Videnskabs-Selskrabets Skrifter., Math.-Naturv. Klasse, no. 6*, **1906**; c) H.-J. Berg, *Bergverksmuseet Skrift* **1999**, *15*, 15.

[13] a) N. H. Magnusson, *GGF* **1960**, *82*, 407; b) A. A. Polkanov, E. K. Gerling, *Ann. N.Y. Akad. Sci.* **1961**, *91*, 492; c) G. Vidal, M. Moczydłowska, *Precambrian Res.* **1995**, *73*, 197.

[14] J. T. Armstrong, *Microbeam Anal.* **1995**, *4*, 177.

[15] For more experimental details see L. M. Keller, R. Wirth, D. Rhede, K. Kunze, R. Abart, *J. Metamorph. Geol.* **2008**, *26*, 99.

[16] The SHRIMP II used in this study is operated by a consortium consisting of Curtin University of Technology, the University of Western Australia, and the Geological Survey of Western Australia.

[17] For more experimental details see a) J. R. De Laeter, A. K. Kennedy, *Int. J. Mass Spectrom.* **1998**, *178*, 43; b) G. Foster, P. Kinny, D. Vance, C. Prince, N. Harris, *Earth Planet. Sc. Lett.* **2000**, *181*, 327.

[18] P. Kinny, 'Users guide to U–Th–Pb dating of titanite, perovskite, monazite and baddeleyite using the W.A. SHRIMP', Curtin University of Technology, School of Physical Sciences, report SPS 693/1997/AP72, **1997**, available from the author.

[19] A.-M. Seydoux-Guillaume, R. Wirth, L. Nasdala, M. Gottschalk, J. M. Montel, W. Heinrich, *Phys. Chem. Mineral.* **2002**, *29*, 240.

[20] L. P. Black, J. D. Fitzgerald, S. L. Harley, *Contrib. Mineral. Petrol.* **1984**, *85*, 141.

[21] A. Meldrum, L. A. Boatner, W. J. Weber, R. C. Ewing, *Geochim. Cosmochim. Ac.* **1998**, *62*, 2509.

[22] L. Nasdala, M. Wildner, R. Wirth, N. Groschopf, D. C. Pal, A. Möller, *Mineral. Petrol.* **2006**, *86*, 1.

[23] A.-M. Seydoux-Guillaume, J.-M. Montel, R. Wirth, B. Moine, *Chem. Geol.* **2008**, *261*, 318.

[24] A.-M. Seydoux-Guillaume, P. Goncalves, R. Wirth, A. Deutsch, *Geology* **2003**, *31*, 973.

[25] J. M. Montel, S. Foret, M. Veschambre, C. Nicollet, A. Provost, *Chem. Geol.* **1996**, *131*, 37; *cf.* also A. Cocherie, F. Albarede, *Geochim. Cosmochim. Ac.* **2001**, *65*, 4509.

[26] F. Poitrasson, S. Chenery, D. J. Bland, *Earth Planet. Sc. Lett.* **1996**, *145*, 79.

[27] a) C. M. Pointer, J. R. Ashworth, R. A. Ixer, *Mineral. Petrol.* **1988**, *39*, 21, b) L. Nasdala, A. Kronz, R. Wirth, T. Váczi, C. Pérez-Soba, A. Willner, A. K. Kennedy, *Geochim. Cosmochim. Ac.* **2009**, *73*, 1637.

[28] a) H. D. Holland, D. Gottfried, *Acta Cryst.* **1955**, *8*, 291; b) T. Murakami, B. C. Chakoumakos, R. C. Ewing, G. R. Lumpkin, W. J. Weber, *Am. Mineral.* **1991**, *76*, 1510

[29] a) A. Lanzirotti, G. N. Hanson, *Contrib. Mineral. Petrol.* **1996**, *125*, 332; b) F. Finger, I. Broska, M. P. Roberts, A. Schermeier, *Am. Mineral.* **1998**, *83*, 248; c) I. Broska, C. T. Williams, M. Janák, G. Nagy, *Lithos* **2005**, *82*, 71; d) J. Majka, B. Budzyń, *Mineralogia Polonica* **2006**, *37*, 61.

[30] D. E. Harlov, H.-J. Förster, T. G. Nijland, *Am. Mineral.* **2002**, *87*, 245.

[31] D. E. Harlov, R. Wirth, H.-J. Förster, *Contrib. Mineral. Petrol.* **2005**, *150*, 268.

[32] A.-M. Seydoux-Guillaume, R. Wirth, J. Ingrin, *Eur. J. Mineral.* **2007**, *19*, 7.

[33] C. J. Hetherington, D. E. Harlov, *Am. Mineral.* **2008**, *93*, 806.

[34] a) L. Hecht, M. Cuney, *Miner. Deposita* **2000**, *35*, 791; b) R. Mathieu, L. Zetterström, M. Cuney, F. Gauthier-Lafaye, H. Hikada, *Chem. Geol.* **2001**, *171*, 147; c) M. Stanisławska, M. Michalik, *Min. Soc. Poland – Special Papers* **2003**, *23*, 160; d) D. Papoulis, P. Tsolis-Katagas, C. Katagas, *Appl. Clay Sci.* **2004**, *24*, 271; e) R. Grapes, K. Bucher, P. W. O. Hoskin, *Eur. J. Mineral.* **2005**, *17*, 553; f) B. Rasmussen, J. R. Muhling, *Chem. Geol.* **2009**, *264*, 311.

[35] D. Read, M. A. G. Andreoli, M. Knoper, C. T. Williams, N. Jarvis, *Eur. J. Mineral.* **2002**, *14*, 487.

[36] Y. Pan, M. E. Fleet, *Mineral. Mag.* **1993**, *57*, 697.

[37] C. Doelter, H. Sirk, *Monatsh. Chem.* **1910**, *31*, 319.

[38] O. Kress, F. J. Metzger, *J. Am. Chem. Soc.* **1909**, *31*, 640.

[39] S. Teufel, C. A. Heinrich, *Chem. Geol.* **1997**, *137*, 273.

[40] A. Putnis, *Mineral. Mag.* **2002**, *66*, 689.

2.5 A Raman spectroscopic study on the radiation damage of monazite–(Ce)

Ruschel, K., Nasdala, L., Kronz, A., Hanchar, J.M., Többens, D.M., Škoda, R., Finger, F. & Möller, A.

Submitted to *Mineralogy and Petrology* (Submission Confirmation: 02.11.2011)

A Raman spectroscopic study on the structural disorder of monazite–(Ce)

Katja Ruschel • Lutz Nasdala • Andreas Kronz • John M. Hanchar • Daniel M. Többens • Radek Škoda • Friedrich Finger • Andreas Möller

K. Ruschel (✉) • L. Nasdala
Institut für Mineralogie und Kristallographie, Universität Wien,
Althanstraße 14, 1090 Wien, Austria
e-mail: katja.ruschel@univie.ac.at

A. Kronz
Geowissenschaftliches Zentrum, Universität Göttingen,
Goldschmidtstr. 1, 37077 Göttingen, Germany

J. M. Hanchar
Department of Earth Sciences, Memorial University of Newfoundland,
St. John's, NL A1B 3X5, Canada

D. M. Többens
Institut für Mineralogie und Petrographie, Universität Innsbruck,
Innrain 52, 6020 Innsbruck, Austria

R. Škoda
Institute of Geological Sciences, Masaryk University,
Kotlářská 2, 61137 Brno, Czech Republic

F. Finger
Institut für Mineralogie, Universität Salzburg,
Hellbrunnerstraße 34, 5020 Salzburg, Austria

A. Möller
Department of Geology, University of Kansas,
1475 Jayhawk Boulevard, 120 Lindley Hall, Lawrence, KS 66045-7613, USA

Present address:
D. M. Többens
Helmholtz-Zentrum Berlin für Materialien und Energie GmbH,
Hahn-Meitner-Platz 1,14109 Berlin, Germany

Abstract This study addresses whether Raman spectra can be used to estimate the degree of accumulated radiation damage in monazite-(Ce) samples whose chemical composition was previously determined. Our results indicate that the degree of disorder in monazite–(Ce), as observed from increasing Raman band broadening, generally depends on both the structural state (i.e., radiation damage) and the chemical composition (i.e., incorporation of non-formula elements). The chemical effects were studied on synthetic orthophosphates grown using the Li-Mo flux method, and non radiation-damaged analogues of the naturally radiation-damaged monazite–(Ce) samples, produced by dry annealing. We found that the "chemical" Raman-band broadening of natural monazite–(Ce) can be predicted by the empirical formula,

$$\text{FWHM } [\text{cm}^{-1}] = 3.95 + 26.66 \times (\text{Th+U+Ca+Pb})[\text{apfu}]$$

where, FWHM = full width at half maximum of the main Raman band of monazite–(Ce) (i.e., the symmetric PO_4 stretching near 970 cm^{-1}), and (Th+U+Ca+Pb) = sum of the four elements in apfu (atoms per formula unit). Provided the chemical composition of a natural monazite–(Ce) is known, this "chemical band broadening" can be used to estimate the degree of structural radiation damage from the observed FWHM of the $\nu_1(PO_4)$ band of that particular sample using Raman spectroscopy. Our annealing studies on a wide range of international monazite–(Ce) reference materials and other monazite–(Ce) samples confirmed that this mineral virtually never becomes highly radiation damaged. Potential advantages and the practical use of the proposed method in the Earth sciences are discussed.

Introduction

Monazite–(Ce) is a monazite-group orthophosphate mineral with the formula $A[PO_4]$ [where A = Ce, and other light rare earth elements (LREE) substituting for Ce]. These orthophosphate minerals crystallise in

the monoclinic system (space group $P2_1/n$, Z = 4) and consist of chains of alternating AO_9 polyhedrons and distorted PO_4 tetrahedrons parallel to the *c* axis. The polyhedrons share edges with each other to form chains parallel to the *a* axis, and corners and edges with seven neighbouring PO_4 tetrahedrons respectively (Ni et al. 1995; Finch and Hanchar 2003).

Monazite–(Ce) has an extremely broad range of chemical compositions, reflecting its formation in a wide variety of rock types under variable conditions (Williams et al. 2007). Extensive substitution of Ce by other LREEs (especially La, Nd, and Sm) is possible, resulting in solid solutions with other minerals of the monazite group. In addition to the more limited incorporation of heavy REEs, significant amounts of the actinide elements Th and U, and to a much lesser extent Pb, may also be present. The ThO_2 content in monazite–(Ce) normally ranges from 4 and 12 wt.% (Watt 1995; Förster 1998), but contents up to 30 wt.% ThO_2 have also been reported (Overstreet 1967; Bowles et al. 1980) . The incorporation of non-REE ions in the wt.% range is commonly explained by the two coupled substitutions: 1) $2REE^{3+} \leftrightarrow Ca^{2+} + Th^{4+}$; and 2) $P^{5+} + REE^{3+} \leftrightarrow Si^{4+} + Th^{4+}$, which are referred to as the cheralite $[CaTh(PO_4)_2]$ and huttonite ($ThSiO_4$) substitutions, respectively (Bea 1996; Williams et al. 2007; Linthout et al. 2007). In both of these substitution mechanisms, U can be incorporated in addition to Th. However, U is in general in lower abundance in monazite–(Ce), compared to Th; the Th/U ratio averages ≥10 (Förster 1998). Commonly the UO_2 content does not exceed 1 wt.% (Parrish 1990; Meldrum et al. 1996; van Emden et al. 1997). Only in rare cases, higher values for UO_2 have been reported (e.g., Förster 1998); Gramaccioli and Segalstad (1978) reported up to 16 wt.% UO_2. In the case of very high actinide contents, however, it needs to be verified whether Th and U are incorporated in the monazite–(Ce) structure or are an analytical artefact due to the presence of actinide-rich inclusions (e.g., thorite, huttonite, uraninite) that were analysed simultaneously. In the cheralite substitution, divalent cations other than Ca may also be incorporated (Williams et al. 2007). As a result of the radioactive decay of the actinides, high amounts of radiogenic Pb (up to 5 element wt.%, but often much lower) have been reported in monazite–(Ce) (Montel et al. 1996). Additional substitution mechanisms involving other elements (e.g., S, As, F, V) have also been reported (Ondrejka et al. 2007; Williams et al. 2007).

Through the radioactive decay of the incorporated actinides and their unstable daughter nuclei, and the resulting self-irradiation, structural damage is created in minerals. The accumulation of radiation damage may eventually lead to complete destruction of the crystal structure; a process called metamictisation (Ewing 1994). Whether or not the damage is retained in the mineral structure depends on the thermal history of the host mineral, i.e., post-crystallisation thermal annealing (Meldrum et al. 1998; Nasdala et al. 2001) and the physical properties of the mineral. Thermal annealing threshold temperatures depend on the structure type as well as on the chemical composition and are therefore mineral-specific (e.g., Meldrum et al. 2000). To the best of our knowledge, natural monazite–(Ce) has never been found in the fully metamict state, even after having experienced extensive self-irradiation (Chakoumakos et al. 1990; Popa et al. 2007). The generally low level of accumulated radiation damage in the monazite structure can be explained by the phenomena that monazite–(Ce) is able to restore its crystalline structure at relatively low temperatures over geologic time (Boatner and Sales 1988; Meldrum et al. 1998). Irradiation effects (i.e., electron beams or alpha particles) have also been reported to cause recovery of the structural damage (Meldrum et al. 1996; Ouchani et al. 1997; Harrison et al. 2002).

The investigation of the structural state of monazite–(Ce) is of crucial importance for Earth sciences and materials sciences. Radiation-damaged minerals are characterised typically by reduced physical stability and increased chemical reactivity (Lumpkin 2001; Horie et al. 2006; Nasdala et al. 2010b; Lenting et al. 2010). A radiation-damaged crystal structure has, for example, been proposed to enhance susceptibility to chemical alteration and hence the loss of radiogenic isotopes. In particular, Pb volume and/or grain boundary diffusion will disturb the U–Th–Pb isotope systematics and bias dating results (Goncalves et al. 2005; Kuiper 2005). Furthermore, monazite–(Ce) plays an important role in thermobarometry, geochemistry, and petrology (Williams et al. 2007), and the degree of accumulation of radiation damage may yield important information in reconstructing the geological history of a sample. Since monazite-based ceramics are considered as potential host matrices for the immobilisation of radionuclides (Ewing 1999; Terra et al. 2003), several studies have been done to assess the performance of monazite structure orthophosphates in the long-term storage of radioactive waste (Trocellier 2000; Oelkers and Poitrasson 2002; Burakov et al. 2008; Montel 2011).

Nasdala et al. (1995) introduced Raman spectroscopy as a method to quantify the degree of radiation damage in zircon. Compared to powder X-ray diffraction, Raman spectroscopy has the advantage to be a non-destructive technique that allows the material to be studied on a micrometre scale with minimum sample preparation. Also, the interpretation is relatively straightforward because the Raman spectrum of zircon is controlled mainly by the structural state, whereas chemical effects are mostly insignificant (except for Hf, zircon rarely incorporates non-formula elements (e.g., P, REEs, U, Th) in the wt.% range).

In contrast, the assignments of Raman spectral changes in monazite–(Ce) are more complex and

thus challenging due to its extensive chemical diversity and hence potentially strong chemical effects on the Raman spectrum. Monazite–(Ce) Raman spectra are thought to be affected by both the structural state and the chemical composition (i.e., its compositional deviation from pure $CePO_4$). The main objective of this present study is to quantify the "chemical" effects, in order to develop an empirical Raman-based in situ assessment of the degree of damage in monazite–(Ce) samples of known chemical composition.

Background information on Raman spectroscopy of monazite–(Ce)

The Raman spectrum of a well-crystallised, undoped, synthetic $CePO_4$ crystal is presented in Fig. 1. The spectrum shows distinct vibrational bands in the ranges 970–1075 cm^{-1} and below 620 cm^{-1}. The former are assigned to the internal PO_4 stretching vibrations, whereas the latter are due to the PO_4 bending and external vibrations involving movements of the Ce^{3+} ions and the $[PO_4]^{3-}$ units (Begun et al. 1981; Hobart et al. 1983; Silva et al. 2006). The most intense band near 970 cm^{-1}, an A_g mode, is assigned to the symmetric stretching of the PO_4 tetrahedrons. Silva et al. (2006) discussed that this band may also involve a small contribution of a B_g mode.

The interpretation of the Raman spectrum of monazite–(Ce), that is, the assignment of individual Raman bands to specific vibrational modes, is still somewhat controversial (Begun et al. 1981; Hobart et al. 1983; Silva et al. 2006). To support these assignments, we have performed ab initio calculations of the theoretical Raman spectrum of monoclinic $CePO_4$ at Γ-point using 3D-periodic density functional theory and Gaussian basis sets, employing the program CRYSTAL 09 (Dovesi et al. 2009; Pascale et al. 2004). A description of the calculation procedure and the results are presented in the online resource S1. For more details on the theoretical background of the ab initio calculations, the reader is referred to Többens and Kahlenberg (2011). Symmetry representation analysis gives the species of the optical modes for monazite–(Ce) as $\Gamma = 18\ A_g + 17\ A_u + 18\ B_g + 16\ B_u$, thus a total of 36 Raman-active modes ($A_g + B_g$). Calculated Raman shifts are represented as tick-marks in Fig. 1. The maximum deviation between calculated and observed Raman shifts is ±13 cm^{-1}, with a standard deviation 6 cm^{-1}. Within this limit of accuracy, the assignment is in full agreement with the experimental mode symmetries (Begun et al. 1981; Silva et al. 2006), and complete and unequivocal assignment is possible for nearly all bands (see online resource S1 for full table).

The calculated mode in best agreement with the observed ν_1 vibration is the A_g mode at 957 cm^{-1}, which agrees with previous assignments. The corresponding B_g mode is calculated with slightly lower wavenumber of 951 cm^{-1}. Apart from the symmetry the atomic displacements of the two modes are very similar. The vibration has been correctly assigned as symmetric P–O stretching mode. However, the displacement of the O2 atom was found to be especially pronounced. This oxygen atom is the one with increased O–Ce distances and a decreased P–O–Ce angle compared to the other three oxygen atoms in the PO_4 tetrahedron (Beall et al. 1981).

The Raman spectrum of the radiation-damaged natural monazite–(Ce) corresponds in general to that of its annealed and hence well-crystallised analogue; however, bands show some variations in their Raman shifts (typically toward lower wavenumbers), extensive increases of their widths (commonly expressed as FWHMs), intensity losses, and the increasing development of band asymmetries. These spectral changes reflect the interaction of phonons with defects, the irregularity of the structure and strain (Falkovsky 2001; Nasdala et al. 2010a). Possible additional effects, such as the splitting of Raman bands or the appearance of additional bands have to the best of our knowledge, not been described thus far for radiation-damaged monazite–(Ce).

It needs to be pointed out, however, that the spectral changes mentioned above (i.e., band shifts, FWHM increases, intensity losses, and sometimes band asymmetries) are typical of a decrease in short-range order. Therefore they may indicate, but do not necessarily verify, the accumulation of radiation damage in the mineral structure. The same or similar spectral changes may alternatively be caused by shock-compression (Gucsik et al. 2004), mechanical stress (Pačevski et al. 2008), and in particular by the extensive incorporation of non-formula elements in the host structure, as shown for other minerals (Hoskin and Rodgers 1996; Bergman et al. 1997; Gasanly 2003; Geisler et al. 2005; Sahoo et al. 2009).

Samples investigated and sample preparation

Both natural (i.e., hence potentially radiation damaged) and synthetic (i.e., well crystallised) monazite–(Ce) samples were investigated in this study. In the case of natural samples, chemically homogeneous specimens were preferred because of reduced uncertainties in the comparability of un-annealed and annealed parts of grains. A few heterogeneous samples, showing relatively large interior regions, were also included. An overview of the natural monazite–(Ce) samples analysed in this study, including their origins and ages, is given in Table 1.

Of each natural monazite–(Ce) sample either fractions of one crystal or several crystals were subjected to dry annealing experiments. For this, chips or crystals of several hundred micrometres up to several millimetres in size were placed individually

in a platinum crucible and annealed in air at a temperature of 1200 °C for four days. These annealing conditions (i.e., temperature and especially duration) are known from previous studies to ensure nearly complete annealing of the radiation damage in monazite–(Ce) (e.g., Seydoux-Guillaume et al. 2002). Samples were heated at a rate of 10 °C/min. After the 96 hours annealing run, the furnace switched off; samples were taken out after another 24 hours, after which they had cooled down slowly to near room temperature.

Single crystals of monazite-structure APO_4 orthophosphates were synthesised using a Li-Mo flux-type method (Hanchar et al. 2001) at Memorial University of Newfoundland. The flux consisted of 10 mol% Li_2MoO_4 and 84 mol% MoO_3. An additional 3 mol% $NH_4H_2PO_4$ was added to each run as the phosphorous source. The raw materials for the various cations were added in the individual syntheses as shown in Table S2 in the online resource S2. The starting materials were mechanically mixed in an agate mortar and pestle and then transferred to a clean platinum crucible with a tightly fitted Pt lid. The crucible was lowered into the "hot spot" of a preheated (1250°C) Deltech $MoSi_2$ vertical tube furnace for eight hours, and then cooled over 138 hours to 1030 °C at a cooling rate of 1.6 °C per hour. Using a type S control thermocouple, the temperature in the hot spot was measured to within ±5°C. When saturation was reached, the monazite–(Ce) crystals began to grow in the residual flux.

Afterwards the crucible was removed and after cooling to room temperature the crystals were extracted from the residual flux (if any existed) by placing the crucible in concentrated NH_4OH for 12 hours, followed by rinsing in distilled H_2O. This was followed by a rinse in concentrated HNO_3 for half an hour, and then a final rinse in distilled H_2O. Further information on the method, including a discussion on the redox conditions in the flux, is given in Hanchar et al. (2001).

Chips of the untreated and the annealed natural specimens, as well as the synthetic samples, were prepared as doubly polished thin sections attached to a glass slide (thicknesses ~30 μm) with random crystallographic orientations. For back-scattered electron (BSE) imaging and electron microprobe analysis, the sections were coated with carbon.

Experimental details

The internal structures of samples were characterized with BSE imaging using a JEOL JSM-6400 scanning electron microscope (SEM) at the University of Vienna and a JEOL JXA-8900 RL electron probe microanalyser (EPMA) at the Georg-August-University of Göttingen, both operated at an accelerating voltage of 20 kV and a beam current of 20 nA. The BSE images were used to check for potential internal heterogeneity, and to select the interior regions to be studied.

In situ chemical analyses were done using a JEOL JXA-8900 RL (Göttingen) and a Cameca SX 100 EPMA at the Masaryk University of Brno. All results reported are means of multiple analyses. An average of eight point analyses were done on homogeneous grains, whereas heterogeneous grains were probed by three to five single analyses per interior region.

Analyses on the JEOL JXA-8900 (Göttingen) were done with an acceleration voltage of 20 kV, a beam current of 20 nA and a beam diameter of ~7 μm. The following reference standards were used (respective element and peak counting time listed in brackets): REE-CAS glasses (from P&H Developments) (for REEs; 30–60s), synthetic $ThSiO_4$ (for Th; 60s), synthetic UO_2 (for U; 60s), natural cerussite (for Pb; 15s), natural wollastonite (for Si and Ca; 15 and 30s), and synthetic YPO_4 (for P and Y; 30s). The background counting times were always set at half the respective peak counting time. Data processing was done with the CITZAF routine in the JEOL software, which is based on the $\Phi(\rho Z)$ correction method (Armstrong 1991, 1995). Average detection limits (2σ error by counting statistics of the background signal) given in oxide wt.% are: for REE (0.08–0.16), for Si (0.07), for Th (0.03), for Ca (0.02), for Pb (0.11), and for U (0.03). Relative errors (2σ error) are estimated to be <2% at the >10 wt.% level, <5% at the 1–10 wt.% level and >5% at the <1 wt.% level.

Additional point analyses were done using a Cameca SX 100 EPMA (Brno) with an accelerating voltage of 15 kV, a beam current of 20 nA and a beam diameter of 2 μm. The following reference standards were used: individual synthetic $REEPO_4$ compounds (for the REEs); synthetic $LaPO_4$ (for P); synthetic $CaTh(PO_4)_2$ (for Ca and Th); U (for U); synthetic PbS (for Pb); and YAG (for Y), and natural spessartine (for Si). The counting times were set as 20s for major elements and 40s to 60s for minor and trace elements. Background counting times were set at half the respective peak counting times and data were reduced using the PAP routine (Pouchou and Pichoir 1985). Average detection limits (2σ error by counting statistics of the background signal) given in oxide wt.% are: for REE (0.11–0.46), for Si (0.07), for Th (0.14), for Ca (0.07), for Pb (0.10), and for U (0.19). Relative errors (2σ error) are estimated to be <5% at the >10 wt.% level, <15% at the 1–10 wt.% level and >15% at the <1 wt.% level.

Room-temperature Raman microprobe measurements used a Horiba Jobin Yvon LabRam-HR (high resolution) system at the University of Vienna equipped with Olympus BX41 optical microscope, a grating with 1800 grooves per millimetre, and Si-based, Peltier thermo-electrically cooled charge-coupled device (CCD) detector. Spectra were excited using the He–Ne 632.8 nm emission line (8 mW measured behind the

microscope objective). This red excitation wavelength was chosen because, in contrast to blue or green laser excitations, it involves the least number of problems with laser-induced photoluminescence that may obscure the Raman signal. With the system operated in confocal mode and an Olympus 100× objective (numerical aperture = 0.9), the lateral resolution was better than 1.5 μm, and the depth resolution (with the beam focused at the sample surface) was approximately 2–3 μm. The spectral resolution was determined to be 0.8 cm^{-1}. Eight replicate measurements per sample [homogeneous monazite–(Ce)] or four replicate measurements per interior region [heterogeneous monazite–(Ce)] were done, respectively. Raman bands were fitted after appropriate background correction assuming Lorentzian–Gaussian band shapes. The actual FWHMs of the most intense monazite–(Ce) Raman band at ~970 cm^{-1} (symmetric stretching of the PO_4 tetrahedrons) were calculated by correcting the measured FWHM values for the apparatus function of the Raman instrument (see Dijkman and van der Maas 1976; Nasdala et al. 2001). Wavenumber calibration was done using the Rayleigh line and Ne lamp emissions; the wavenumber accuracy was better than 0.5 cm^{-1}. The errors of FWHMs determined from single spectra are assessed to be between ±0.4 cm^{-1} for narrow Raman bands (FWHM <6.5 cm^{-1}) and ±1.5 cm^{-1} for strongly broadened Raman bands (FWHM >20 cm^{-1}). For broader Raman bands fitted, uncertainties are higher, especially for slightly asymmetric bands (cf. discussion below). Raman microprobe measurements were generally carried out prior to EPMA analysis, to exclude possible effects of the focused electron beam on the accumulated radiation damage (Meldrum et al. 1996; Nasdala et al. 2003).

Results and Discussion

Preliminary notes on the Raman evaluation

The dominant $\nu_1(PO_4)$ symmetric stretching band near 970 cm^{-1} (cf. Fig. 1) proved to be most suitable for studying the short-range order of monazite–(Ce). The high intensity of the $\nu_1(PO_4)$ band is advantageous insofar as the band remains well detectable even in radiation-damaged samples, which commonly show lowered band intensities. Furthermore, the relevant spectral parameters of this band (i.e., Raman shift and FWHM) do not show significant orientation dependence, which is advantageous for the application of analysing non-oriented unknown monazite-(Ce) grains in thin section. The $\nu_1(PO_4)$ vibration was already shown to be sensitive to disorder by Seydoux-Guillaume et al. (2002). According to Gouadec and Colomban (2007), Raman stretching modes are especially sensitive to the disorder of their nearest neighbouring structure atoms. Our observations suggests that the FWHM of the $\nu_1(PO_4)$ Raman band as the most suitable spectral parameter to estimate the degree of short-range order of monazite–(Ce). In Raman spectroscopy, disorder is commonly characterised by band broadening and the FWHM value is used often as a parameter to study and quantify disorder in crystal structures (Mohanan et al. 1993; Nasdala et al. 1998, 2003; Gouadec and Colomban 2007).

It should be noted that the structure of partially radiation-damaged minerals can be described as a three-dimensional, nanometre-scale network consisting of amorphous (recoil-) damage clusters and crystalline remnants which are characterised by increasing defect density and increasing stress (e.g., Weber et al. 1994; Salje et al. 1999; Seydoux-Guillaume et al. 2004). By evaluating the spectral parameters of the $\nu_1(PO_4)$ band discussed above, only the degree of disorder of the remnant crystalline volume-fraction of the radiation-damaged monazite–(Ce) is studied. The Raman signal of the amorphous volume-fraction has not been observed, perhaps due to its relative intensity being too low (as shown for zircon by Nasdala et al. 2003).

Synthetic monazites

Single crystals of APO_4 orthophosphates ~1 mm up to 5 mm in length were produced in all of the syntheses. In the synthesis done to produce Y-bearing monazite–(Ce), a small amount of Ce-bearing xenotime–(Y) was also co-crystallised as a distinct phase.

The crystals grown are generally euhedral shaped. Most syntheses produced chemically homogeneous samples. Average formulae were calculated from EPMA analyses based on 4 oxygen atoms per formula unit and that all REE are incorporated in the trivalent state (see Table 2; detailed results of EPMA analyses are shown in Table S3 in the online resource S2). Only the syntheses containing Th, Y, and Gd produced relatively heterogeneous crystals. For those samples, values for two interior regions each are reported in Table 2 (respectively Table S3). In the syntheses involving Ca^{2+} and Th^{4+}, no charge-compensating species (e.g., tetravalent Si) were intentionally added to the flux. It remains therefore unclear how charge balance is maintained. However, the incorporation of small amounts of divalent and tetravalent elements without any coupled substitution has been reported to occur in natural and synthetic monazite–(Ce); it was explained by the formation of vacancies (Clavier et al. 2011). Another explanation might be the occurrence of tetravalent Ce, which according to Hanchar et al. (2001) might exist in small amounts. The dominant form, however, of Ce is 3+ under the fO_2 and temperature conditions for the flux used [see Appendix in Hanchar et al. (2001)]. Nevertheless, Ce is thought to be incorporated predominantly in the

trivalent state under the syntheses conditions used (Bregiroux et al. 2007; Popa et al. 2007).

Raman band shifts and FWHMs of the synthesis run products are reported in Table 2. The Raman shift of the PO_4 symmetric stretching band increases with the decrease of the average ionic radius of the A-site cation(s) [calculated based on the radii from Shannon (1976)]. This is shown in Fig. 2A, in comparison with corresponding data for some pure lanthanide orthophosphates ($REEPO_4$) from Silva et al. (2006). The systematic shift of the $\nu_1(PO_4)$ band toward higher Raman shift values, with decreasing radius of the A-site cation (or its increasing atomic number), has previously been described for pure orthophosphates and was controversially interpreted by several authors (cf. below). On the one hand, shorter P–O distances and higher vibrational frequencies of the P–O bonds in the phosphate groups are thought to occur as a consequence of a closer packing (compression) of the PO_4 groups (Begun et al. 1981; Hobart et al. 1983; Paschoal et al. 2002). On the other hand, the increase of the Raman band shift was attributed to the reduction of the REE–O bond length in the unit-cell and a contraction of the cation site (Podor 1995; Santos et al. 2007).

Changes observed in FWHM values are moderate among the types of REEs and for variable REE concentrations (see Table 2 and Fig. 2B). Slight band-shape asymmetry is observed for some samples. Only samples including Th reveal strongly increased FWHMs when compared to pure $CePO_4$. This indicates a strong effect of Th substitution on band broadening. However, the contribution of other potential causes, such as vacancies or pores, need to be considered in discussing the Raman band broadening of Th-containing syntheses; note that crystals produced in these syntheses revealed deficient analytical totals (in some cases down to 97 wt.%). A significant effect of the Th content on the FWHMs is supported by the results of Podor (1995) who demonstrated that the $\nu_1(PO_4)$ Raman band of $(La_{1-2x}U_xCa_x)PO_4$ and $(La_{1-2x}Th_xCa_x)PO_4$ compounds showed systematic band broadening with increasing actinide content. Those authors explained their observation with the random cation-site population around the PO_4 tetrahedrons. Raison et al. (2008) stated that the cheralitic substitution of REE^{3+} by Th^{4+} and Ca^{2+} in the monazite structure has significant effects on Raman spectra. These authors found that the PO_4 tetrahedrons in synthetic cheralite $[CaTh(PO_4)_2]$ exhibit significant distortions compared to structural values of $CePO_4$ and assigned this to the different oxidation states and ionic radii of the cations. According to Raison et al. (2008) the strong broadening of the $\nu_1(PO_4)$ Raman band indicates that the P–O distances in $CaTh(PO_4)_2$ are less well defined than in $CePO_4$. They concluded that (Ca,Th) substitution causes similar distortion in the monazite structure as radiation damage, and hence leads to almost identical spectra. This is supported by a spectrum obtained from synthetic $CePO_4$ irradiated with 8.8 MeV $^4He^{2+}$ ions (fluences of 1×10^{16} ions/cm^2) (Fig. 2B). For details concerning the irradiation experiments see Nasdala et al. (2011).

Natural monazite–(Ce)

Results of selected in situ chemical and Raman analyses of natural monazite–(Ce) samples are shown in Table 3. In the upper part of that table, results for un-annealed homogeneous monazite–(Ce) specimens and their annealed counterparts are reported, whereas in the lower part of the table, analyses placed in interior regions of annealed heterogeneous samples are quoted. Note that the chemical data reported for the homogeneous samples are means of chemical analyses done on both un-annealed and annealed chips of the same sample; this was done to get better representative mean values. Note also that chemical analyses revealed no systematic changes in the samples' chemical composition resulting from the thermal annealing. All analysed samples proved to be monazite–(Ce). They show a broad variation in actinide contents, with ThO_2 ranging from 1.3 wt.% to 19.6 wt.% and UO_2 from below the detection limit up 4.9 wt.%. Some of the analyses yielded deficient totals down to 97 wt.%. This may first be due to non-formula elements that were not analysed (however, element scans did not indicate the presence of such constituents). Second, deficient totals may potentially indicate a porous texture on the sub-micrometre range, as it typically results from secondary alteration processes (Nasdala et al. 2009).

Homogeneous samples show only minor changes of their $\nu_1(PO_4)$ Raman band position upon annealing; slight shifts to higher wavenumbers (up to +2.9 cm^{-1}; Table 3) were observed. The moderately lower wavenumbers of radiation-damaged monazite–(Ce) indicate expansion of the P–O bonds, due to the increasing distortion and tilting of PO_4 tetrahedrons, as well as dilative strain (Nasdala et al. 2010a). Changes in bandwidths are more significant; the FWHMs of the $\nu_1(PO_4)$ band were found to decrease through annealing up to as much as minus 12.8 cm^{-1}. The likely major causes of the broadened bands of the un-annealed (and hence somewhat radiation-damaged) monazite–(Ce) are the accumulation of point defects and the increasing irregularity of the PO_4 tetrahedrons (Nasdala et al. 2010a).

A BSE image of the un-annealed heterogeneous sample P1 and two corresponding spectra showing the $\nu_1(PO_4)$ Raman band are presented in Fig. 3A,B. The spectra are affected by radiation damage and the chemical composition. The BSE image and spectra for an annealed grain of sample P1 are shown in Figs. 3C and D. In that example, chemical heterogeneity is solely responsible for the differences in the spectra, and in particular, the different FWHMs. Some oxides (e.g., CeO_2 was identified by Raman spectroscopy) occur at the surface of the

annealed grain (Fig. 3C). These artefacts result probably from slight surficial decomposition upon annealing (Váczi et al. 2009). The $\nu_1(PO_4)$ Raman bands (Figs. 3B and D) are characterised by slight asymmetry on the low-wavenumber side. The occurrence of asymmetric (and broadened and down-shifted) Raman bands has often been assigned to phonon confinement effects (Spanier et al. 2001; Sahoo et al. 2009). Phonon confinement is, however, expected for particle or domain sizes on the nanometre length scale (Kanemitsu et al. 1993). For radiation-damaged zircon, notable confinement effects on Raman spectra are therefore expected to occur only at elevated stages of the metamictisation process, where nanometre-sized crystalline and amorphous domain sizes exist (Geisler et al. 2001; Geisler and Pidgeon 2002; Nasdala et al. 2002). However, in the case of the rather moderately radiation-damaged monazite–(Ce), and in particular in the case of the annealed material, phonon confinement is less likely. The cause of the observed slight asymmetries therefore remains unclear.

Our results suggest that the broadening of the $\nu_1(PO_4)$ Raman band in the annealed monazite–(Ce) samples are strongly correlated with the Th content. For the example of the annealed sample P1 (Figs. 3C and D), a Th-rich interior region (0.15 apfu Th) yielded a FWHM of the $\nu_1(PO_4)$ Raman band of 10.2 cm^{-1}. In contrast, in a low-Th region (0.02 apfu Th) of the same sample, a notably lower FWHM value of 4.9 cm^{-1} was obtained. The striking dependence of the FWHM on the Th content is consistent with results from our studies on synthetic monazite–(Ce) samples. For all other elements, no such obvious chemical effect on the Raman spectrum was observed. However, possible chemical effects of similar strength as caused by other elements incorporated may either have been overlooked because of too low concentrations, or they might be obscured by the strong effect of Th, which is always present in the wt.% oxide range.

Using an empirical approach we found a close correlation of the FWHM of the $\nu_1(PO_4)$ Raman band with the sum of the four elements Th, U, Ca and Pb (contents in apfu; Fig. 4). Other elements, in contrast, in particular Si and REEs other than Ce, seem to have only minor or insignificant effects on the FWHM. An empirical linear regression was determined using

$$\text{FWHM}\ [cm^{-1}] = 3.95 + 26.66 \times (\text{Th}+\text{U}+\text{Ca}+\text{Pb})[\text{apfu}] \quad (1)$$

where 3.95 and 26.66 are coefficients from the linear regression fitting. This interpretation, however, is not straightforward. The PO_4 vibrations in monazite–(Ce) are influenced by numerous factors (especially the ionic radii, valences, and masses of the nearest neighbouring cations, bond forces among atoms, etc.), which lead to complex interactions especially in the case of monazite–(Ce) containing high amounts of non-formula elements. However, the four elements Th, U, Ca, and Pb differ more significantly from Ce, when compared to REEs other than Ce. They are hence expected to have stronger disordering effects on their nearest neighbouring PO_4 groups, and consequently induce stronger broadening of PO_4 vibrational modes, compared to the presence of REE^{3+} other than Ce. The apparent absence of a clear FWHM-broadening effect of the Si^{4+} present might be explained by the consideration that Si is substituted at the 4-coordinated phosphorus site. It is hence located much further away from other PO_4 groups, compared to the larger A-site cations, which accounts for smaller or even negligible effects on the PO_4 vibrations. However, our samples showed relatively minor Si contents. It appears worthwhile to study potential spectroscopic effects of the silicon substitution in more detail by investigating particularly Si-rich monazites or synthetic samples.

The regression and subsequent considerations given above imply that the actinides Th and U (which are similar in ionic radius and valence) may have similarly strong effects on the Raman spectrum of monazite–(Ce). This hypothesis is supported in general by the results of Podor (1995) and Bregiroux et al. (2007; that study did not reveal significant differences between the Raman spectra of $Ca_{0.5}Th_{0.5}PO_4$ and $Ca_{0.5}U_{0.5}PO_4$) and the current study. Note that the correlation above is still inconclusive as it is based on a sample set limited in terms of both chemical compositions and ages (and hence possible radiation damage). For odd chemical compositions (e.g., high amounts of Mg, As, V, etc.) the applicability of the formula given above requires further investigation.

The correlation of FWHMs of the $\nu_1(PO_4)$ band versus the sums of Th, U, Ca and Pb for pairs of un-annealed monazite–(Ce) and their annealed analogues are shown in Fig. 5. The respective difference between $FWHM_{un\text{-}annealed}$ and $FWHM_{annealed}$ (Δ_{FWHM}; indicated by the lengths of dotted lines in Fig. 5), is taken as a measure of the degree of the radiation damage in the natural (i.e., un-annealed) sample. As Δ_{FWHM} is a result of both self-irradiation and thermal annealing over geologic periods of time, it does not correlate with the calculated alpha doses (which only quantify the theoretically maximum self-irradiation; see Table 3). To give an example, sample Elk Mountain (alpha dose 10.8×10^{19}/g; Δ_{FWHM} values of 8.9 cm^{-1}) has experienced much more alpha induced self-irradiation but obviously stored only about the same amount structural damage, compared to sample Namon (alpha dose 3.8×10^{19}/g; Δ_{FWHM} values of 9.2 cm^{-1}). This indicates that sample Elk Mountain has experienced a higher degree of partial annealing.

The alpha doses calculated for the monazite–(Ce) samples studied (between 1.2×10^{19}/g and 10.8×10^{19}/g) are high compared to the alpha dose value of $\sim 10^{19}$ alpha events per gram calculated for nearly amorphous Sri Lankan zircon (Weber et al. 1994,

Nasdala et al. 2004). If view of this, it is remarkable: 1) that all samples yielded well-detectable Raman bands of crystalline $CePO_4$; and 2) that these bands showed rather moderate damage-induced broadening. The first observation verifies that none of the samples have become fully metamict, which indicates decidedly incomplete storage of the radiation damage experienced by samples, and notable to strong partial reconstitution due to thermal annealing. The second observation is supported by the fact that all calculated Δ_{FWHM} values lie between 6.6 cm^{-1} and 12.8 cm^{-1} (Table 3). The maximum of 12.8 cm^{-1} is comparably moderate, considering analogous data for strongly radiation-damaged zircon for which the radiation-induced band broadening of the $\nu_3(SiO_4)$ mode FWHMs may exceed 30 cm^{-1} (Nasdala et al. 2001). This suggests that all samples investigated in the present study represent moderate degrees of radiation damage.

It should also be pointed out that it is not completely unexpected to see differences in the response to self-irradiation in a monazite–(Ce), a monoclinic orthophosphate, and zircon, a tetragonal orthosilicate, given that these materials are quite different in their chemical and physical properties. Meldrum et al. (2000), showed for a range of ABO_4-type phosphates and silicates that the different materials responded quite differently to similar doses of implanted ions and that orthophosphates are much more efficient at thermal annealing than are orthosilicates.

The detection of "crystalline" Raman spectra, and the calculation of moderate Δ_{FWHM} values, for all 16 homogeneous monazite–(Ce) samples studied reconfirms that monazite–(Ce) never becomes strongly radiation damaged or even fully metamict (Nasdala et al. 1999). Only a small fraction of the radiation damage experienced has been stored by the samples whereas the majority of the damage is lost through thermal annealing. The high extent of the damage annealing, connected with the preservation of the crystalline state (and hence the physical and chemical resistance of the material), accounts for the potential suitability of monazite–(Ce) and other orthophosphates as host materials for the immobilisation of radioactive waste (see Montel, 2011 and references therein). Nevertheless it is important to note that the resistance of the material largely depends on the environmental conditions. Monazite–(Ce) is more quickly dissolved in an undersaturated aqueous fluid than in a dry environment (Rapp und Watson 1986; Nasdala et al. 2010c). This behaviour somewhat questions the suitability of monazite–(Ce) for the long-term storage of radionuclides. Also, it is worthy of note that none of 16 samples from localities worldwide were found to be only mildly or even undamaged. In other words, the relatively limited range of Δ_{FWHM} values calculated (Table 3) indicates relatively similar degrees of (low to moderate) radiation damage in all samples studied. This may be explained by the consideration that the thermal annealing rate of monazite–(Ce) increases strongly with increasing damage accumulation; damage is stored relatively easily by the pristine material whereas the annealing rate is much higher as soon as moderate levels of structural damage are reached. A similar conclusion was drawn from the observation that the thermal stability of fission tracks lowers appreciably with increasing accumulation of structural radiation damage (Garver et al. 2005; Weise et al. 2009).

Conclusions

Equation (1) allows for the prediction of the effect(s) of chemically-induced disorder in monazite–(Ce) on the FWHM of its $\nu_1(PO_4)$ Raman band. The difference between band broadening that is estimated from the chemical composition and the observed band broadening, can then be used as a proxy of the "structural" Raman-band broadening due to accumulated radiation damage. A potential application is a relatively simple pre-selection of less radiation damaged crystals or interior regions within crystals prior to U–Th–Pb, U–He, or fission track dating. This would allow to avoid biased results caused by analysis of structurally "weakened" material that is potentially more susceptible to chemical alteration and/or the loss of radiogenic isotopes. Another application is the study of the thermal history of monazite–(Ce) grains and their host rocks, also possible within thin section. Grains whose observed $FWHM_{un\text{-}annealed}$ do not deviate significantly from the value predicted using equation (1) cannot have accumulated notable amounts of radiation damage. This would point either to a very young sample or a young annealing event in the host rock's thermal history.

Raman spectroscopy has been demonstrated to be a convenient method for analysing accessory minerals (minor preparation requirements, volume-resolution on the micrometre scale, non-destructive analysis), with the special advantage of its sensitivity to detect the short-range order in natural minerals, including monazite–(Ce).

Our observations suggest that all monazite–(Ce) samples studied are characterised by moderate degrees of radiation damage. This assessment, however, must remain "semi-quantitative" at the present stage. To provide a reliable Raman-based estimation of the structural radiation damage in monazite–(Ce), a calibration of irradiation effects on Raman spectral parameters needs to be compiled. Ion-irradiation experiments on various synthetic and natural monazite–(Ce) samples are needed to achieve this and are planned for future work.

Acknowledgements: The natural monazite–(Ce) samples used in this study were kindly made available by A. Ertl, M. J. Jercinovic, A. Kennedy, B. Schulz,

and A.-M. Seydoux-Guillaume. Thanks are due to A. Wagner for sample preparation, and C. Fisher, E. Libowitzky and D. Talla for experimental assistance. Partial funding for this research was provided by the European Commission through contract no. MEXC–CT–2005–024878, the Austrian Science Fund (FWF) grant P20028–N10 to LN. This work was supported by the Austrian Ministry of Science (BMWF) as part of the UniInfrastrukturprogramm of the Forschungsplattform Scientific Computing at LFU Innsbruck. JMH thanks the Canadian Natural Sciences and Research Council (NSERC) for partial support for this research in the form of a Discovery Grant, and Memorial University of Newfoundland, for additional financial support for this project.

References

Alagna KE, Petrelli M, Perugini D, Poli G (2008) Micro-Analytical Zircon and Monazite U-Pb Isotope Dating by Laser Ablation-Inductively Coupled Plasma-Quadrupole Mass Spectrometry. Geostand Geoanal Res 32:103–120

Armstrong JT (1991) Quantitative elemental analysis of individual microparticles with electron beam instruments. In: Heinrich KFJ, Newbury DE (eds) Electron Probe Quantitation, Plenum Press, New York, London, pp 261–315

Armstrong JT (1995) CITZAF: a package of correction programs for the quantitative electron microbeam X-ray analysis of thick polished materials, thin films, and particles. Microbeam Anal 4:177–200

Bea F (1996) Residence of REE, Y, Th and U in Granites and Crustal Protoliths; Implications for the Chemistry of Crustal Melts. J Petrol 57:521–552

Beall GW, Boatner LA, Mullica DF, Milligan WO (1981) The structure of cerium orthophosphate, a synthetic analogue of monazite. J Inorg Nucl Chem 43:101–105

Begun GM, Beall GW, Boatner LA, Gregor WJ (1981) Raman Spectra of the Rare Earth Orthophosphates. J Raman Spectrosc 11:273–278

Bergman L, Bremser MD, Perry WG, Davis RF, Dutta M, Nemanich RJ (1997) Raman analysis of the configurational disorder in $Al_xGa_{1-x}N$ films. Appl Phys Lett 71:2157–2159

Boatner LA, Sales BC (1988) Monazite. In: Lutze W, Ewing RC (eds) Radioactive waste forms for the future. Elsevier, New York, pp 495–564

Bowles JFW, Jobbins EA, Young BR (1980) A re-examination of cheralite. Mineral Mag 43:885–888

Boyce JW, Hodges KV, Olszewski WJ, Jercinovic MJ, Carpenter BD, Reiners PW (2006) Laser microprobe (U-Th)/He geochronology. Geochim Cosmochim Ac 70:3031–3039

Bregiroux D, Terra O, Audubert F, Dacheux N, Serin V, Podor R, Bernache-Assollant D (2007) Solid-State Synthesis of Monazite-type Compounds Containing Tetravalent Elements. Inorg Chem 46:10372–10382

Burakov BE, Yagovkina MA, Zamoryanskaya MV, Petrova MA, Domracheva YV, Kolesnikova .V, Nikolaeva LD, Garbuzov VM, Kitsay AA, Zirlin VA (2008) Behavior of Actinide Host-Phases Under Self-irradiation: Zircon, Pyrochlore, Monazite, and Cubic Zirconia Doped with Pu-238. In: Krivovichev SV (ed) Minerals as Advanced Materials I, 1st edn. Springer Berlin, Heidelberg, pp 209–217

Chakoumakos BC, Sales BC, Boatner LA (1990) Alpha-decay-induced condensation of phosphate anions in a mineral. Am Mineral 75:1447–1450

Clavier N, Podor R, Dacheux N (2011) Crystal chemistry of the monazite structure. J Eur Ceram Soc 31:941–976

Dijkman FG, van der Maas JH (1976) Dependence of Bandshape and Depolarization Ratio on Slitwidth. Appl Spectrosc 30:545–546

Dovesi R, Saunders VR, Roetti C, Orlando R, Zicovich-Wilson CM, Pascala F, Civalleri B, Doll K, Harrison NM, Busch IJ, D'Arco P, Llunell M (2009) CRYSTAL09 – A computational tool for solid state chemistry and physiscs. University of Torino, Italy

Dumond G, McLean N, Williams ML, Jercinovic MJ, Bowring SA (2008) High-resolution dating of granite petrogenesis and deformation in a lower crustal shear zone: Athabasca granulite terrane, western Canadian Shield. Chem Geol 254:175–196

Ewing RC (1994) The metamict state: 1993 – the centennial. Nucl Instrum Meth B 91:22–29

Ewing RC (1999) Nuclear waste forms for actinides. P Natl Acad Sci Usa 96:3432–3439

Falkovsky LA (2001) Width of optical phonons: Influence of defects of various geometry. Phys Rev B 64: 024301

Finch RJ, Hanchar JM (2003) Structure and Chemistry of Zircon and Zircon-Group Minerals. In: Hanchar JM, Hoskin PWO (eds) Zircon. Rev Mineral Geochem 53:1–25

Fletcher IR, McNaughton NJ, Davis WJ, Rasmussen B (2010) Matrix effects and calibration limitations in ion probe U-Pb and Th-Pb dating of monazite. Chem Geol 270:31–44

Förster H-J (1998) The chemical composition of REE-Y-Th-U-rich accessory minerals in peraluminous granites of the Erzgebirge-Fichtelgebirge region, Germany, Part I: The monazite-(Ce)-brabantite solid solution series. Am Mineral 83:259–272

Garver JI, Reiners PW, Walker LJ, Ramage JT, Perry SE (2005) Implications for Timing of Andean Uplift from Thermal Resetting of Radiation-Damaged Zircon in the Cordillera Huayhuash, Northern Peru. J Geol 113:117–138

Gasanly NM (2003) Effect of crystal disorder on linewidth of the Raman modes in $GaS_{1-x}Se_x$ layered mixed crystals. Cryst Res Technol 38:962–967

Geisler T, Pidgeon RT, van Bronswijk W, Pleysier R (2001) Kinetics of thermal recovery and recrystallization of partially metamict zircon: a Raman spectroscopic study. Eur J Mineral 13:1163–1176

Geisler T, Pidgeon RT (2002) Raman scattering from metamict zircon: comments on "Metamictisation of natural zircon: accumulation versus thermal

annealing of radioactivity-induced damage" by Nasdala et al. 2001 (Contribution to Mineralogy and Petrology 141: 125–144). Contrib Mineral Petr 143:759–755

Geisler T, Burakov BE, Zirlin V, Nikolaeva L, Pöml P (2005) A Raman spectroscopic study of high-uranium zircon from the Chernobyl "lava". Eur J Mineral 17:883–894

Goncalves P, Williams ML, Jercinovic MJ (2005) Electron-microprobe age mapping of monazite. Am Mineral 90:578–585

Gouadec G, Colomban P (2007) Raman Spectroscopy of nanomaterials: How spectra relate to disorder, particle size and mechanical properties. Prog Cryst Growth Ch 53:1–56

Gramaccioli CM, Segalstad TV (1978) A uranium- and thorium-rich monazite from a south-alpine pegmatite at Piona, Italy. Am Mineral 63:757–761

Gucsik A, Zhang M, Koeberl C, Salje EKH, Redfern SAT, Pruneda JM (2004) Infrared and Raman spectra of ZrSiO4 experimentally shocked at high pressures. Mineral Mag 68:801–811

Hanchar JM, Finch RJ, Hoskin PWO, Watson EB, Cherniak DJ, Mariano AM (2001) Rare earth elements in synthetic zircon: Part 1. Synthesis, and rare earth element and phosphorus doping. Am Mineral 86:667–680

Harrison TM, Catlos EJ, Montel J-M. (2002) U–Th–Pb dating of Phosphate Minerals. In: Kohn ML, Rakovan J, and Hughes JM (eds) Phosphates. Rev Mineral Geochem 48:523–558

Hobart DE, Begun GM, Haire RG, Hellwege HE (1983) Raman Spectra of the Transplutonium Orthophosphates and Trimetaphosphates. J Raman Spectrosc 14:59–62

Horie K, Hidaka H, Gauthier-Lafaye F (2006) Elemental distribution in zircon: Alteration and radiation-damage effects. Phys Chem Earth 31:587–592

Hoskin PWO, Rodgers KA (1996) Raman spectral shift in the isomorphous series $(Zr_{1-x}Hf_x)SiO_4$. Eur J Solid State Inorg Chem 33:1111–1121

Kanemitsu, Y, Uto H, Masumoto Y, Masumoto T, Futagi T, Mimura H (1993) Microstructure and optical properties of free-standing porous silicon films: Size dependence of absorption spectra in Si nanometer-sized crystallites. Phys Rev B 48: 2827–2830

Kuiper YD (2005) Isotopic age constraints from electron microprobe U-Th-Pb dates, using a three-dimensional concordia diagram. Am Mineral 90:586–591

Lenting C, Geisler T, Gerdes A, Kooijman E, Scherer EE, Zeh A (2010) The behavior of the Hf isotope system in radiation-damaged zircon during experimental hydrothermal alteration. Am Mineral 95:1343–1348

Linthout K (2007) Tripartite division of the system 2 $REEPO_4$ – $CaTh(PO_4)_2$ – $2ThSiO_4$, discreditation of brabantite, and recognition of cheralite as the name for members dominated by $CaTh(PO_4)_2$. Can Mineral 45:503–508

Lumpkin GR (2001) Alpha-decay damage and aqueous durability of actinide host phases in natural systems. J Nucl Mater 289:136–166

Meldrum A, Wang LM, Ewing RC (1996) Ion beam induced amorphization of monazite. Nucl Instrum Meth B 116:220–224

Meldrum A, Boatner LA, Weber WJ, Ewing RC (1998) Radiation damage in zircon and monazite. Geochim Cosmochim Ac 62:2509–2520

Meldrum A, Boatner LA, Ewing RC (2000) A comparison of radiation effects in crystalline ABO_4-type phosphates and silicates. Mineral Mag 64:185–194

Möller A, Mezger K, Schenk V (2000) U-Pb dating of metamorphic minerals: Pan-African metamorphism and prolonged slow cooling of high pressure granulites in Tanzania, East Africa. Precamb Res 104:123–146

Mohanan K, Sharma SK, Bishop FC (1993) A Raman spectral study of forsterite-monticellite solid solutions. Am Mineral 78:42–48

Montel J-M, Foret S, Veschambre M, Nicollet C, Provost A (1996) Electron microprobe dating of monazite. Chem Geol 131:37–53

Montel JM (2011) Minerals and design of new waste forms for conditioning nuclear waste. C R Geosci 343:230–236

Murakami T, Chakoumakos BC, Ewing RC, Lumpkin GR, Weber WJ (1991) Alpha-decay event damage in zircon. Am Mineral 76:1510–1532

Nasdala L, Irmer G, Wolf D (1995) The degree of metamictization in zircon: a Raman spectroscopic study. Eur J Mineral 7:471–478

Nasdala L, Pidgeon RT, Wolf D, Irmer G (1998) Metamictization and U-Pb isotopic discordance in single zircons: a combined Raman microprobe and SHRIMP ion probe study. Miner Petrol 62:1–27

Nasdala L, Finger F, Kinny P (1999) Can monazite become metamict? Eur J Mineral 11, Beih 1:164

Nasdala L, Wenzel M, Vavra G, Irmer G, Wenzel T, Kober B (2001) Metamictisation of natural zircon: accumulation versus thermal annealing of radioactivity-induced damage. Contrib Mineral Petr 141:125–144

Nasdala L, Irmer G, Jonckheere R (2002) Radiation damage ages: Practical concept or impractical vision? – Reply to two comments on " Metamictisation of natural zircon: Accumulation versus thermal annealing of radioactivity-induced damage", and further discussion. Contrib Minera Petr 143:758–765

Nasdala L, Zhang M, Kempe U, Panczer G, Gaft M, Andrut M, Plötze M (2003) Spectroscopic methods applied to zircon. In: Hanchar JM, Hoskin PWO (eds) Zircon. Rev Mineral Geochem 53:427–468

Nasdala L, Reiners PW, Garver JI, Kennedy AK, Stern RA, Balan E, Wirth R (2004) Incomplete retention of radiation damage in zircon from Sri Lanka. Am Mineral 89:219–231

Nasdala L, Kronz A, Wirth R, Váczi T, Pérez-Soba C, Willner A, Kennedy AK (2009) The phenomenon of deficient electron microprobe totals in radiation-damaged and altered zircon. Geochim Cosmochim Ac 73:1637–1650

Nasdala L, Grötzschel R, Probst S, Bleisteiner B (2010a) Irradiation damage in monazite-(Ce): An example to establish the limits of Raman confocality and depth resolution. Can Mineral 48:351–359

Nasdala L, Hanchar JM, Rhede D, Kennedy AK, Váczi T (2010b) Retention of uranium in complexly altered zircon: An example from Bancroft, Ontario. Chem Geol 269:290–300

Nasdala L, Ruschel K, Rhede D, Wirth R, Kerschhofer-Wallner L, Kennedy AK, Kinny PD, Finger F, Groschopf N (2010c) Phase Decomposition upon Alteration of Radiation-Damaged Monazite–(Ce) from Moss, Østfold, Norway. Chimia 64:705–711

Nasdala L, Grambole D, Götze J, Kempe U, Váczi T (2011) Helium irradiation study on zircon. Contrib Mineral Petr 161:777–789

Ni Y, Hughes JM, Mariano AN (1995) Crystal chemistry of the monazite and xenotime structures. Am Mineral 80:21–26

Novák M, Černý P, Kimbrough DL, Taylor MC, Ercit TS (1998) U-Pb ages of monazite from granitic pegmatites in the Moldanubian Zone and their geological implications. Acta U Carol Geol 42:309–310

Oelkers EH, Poitrasson F (2002) An experimental study of the dissolution stoichiometry and rates of a natural monazite as a function of temperature from 50 to 230 °C and pH from 1.5 to 10. Chem Geol 191:73–87

Ondrejka M, Uher P, Pršek J, Ozdín D (2007) Arsenian monazite-(Ce) and xenotime-(Y), REE arsenates and carbonates from the Tisovec-Rejkovo rhyolite, Western Carpathians, Slovakia: Composition and substitutions in the $(REE,Y)XO_4$ system (X = P, As, Si, Nb, S). Lithos 95:116–129

Ouchani S, Dran J-C, Chaumont J (1997) Evidence of ionization annealing upon helium-ion irradiation of pre-damaged fluorapatite. Nucl Instrum Meth B 132:447–451

Overstreet WC (1967) The geologic occurrence of monazite. Geol Surv Prof Paper 530:114–118

Pačevski A, Libowitzky E, Žinković P, Dimitrijević R, Cvetković L (2008) Copper-bearing pyrite from the Čoka Marin polymetallic deposit, Serbia: Mineral inclusions or true solid-solution? Can Mineral 46:249–261

Parrish RR (1990) U–Pb dating of monazite and its application to geological problems. Can J Earth Sci 27:1431–1450

Pascale F, Zicovich-Wilson CM, Lopez F, Civalleri B, Orlando R, and Dovesi R (2004) The calculation of the vibrational frequencies of crystalline compounds and its implementation in the CRYSTAL code. J Comput Chem 25:888–897

Paschoal CWA, Ayala AP, Guedes I, Loong C-K, Boatner LA (2002) Raman phonons in RPO4 crystals. Proceedings of XVIIIth International Conference on Raman Spectroscopy, 25-30 August, 2002 Budapest, Hungary 18:577–578

Podor R (1995) Raman spectra of the actinide-bearing monazites. Eur J Mineral 7:1353–1360

Popa K, Bregiroux D, Konings RJM, Gouder T, Popa AF, Geisler T, Raison PE (2007) The chemistry of the phosphates of barium and tetravalent cations in the 1:1 stoichiometry. J Solid State Chem 180:2346–2355

Pouchou JL, Pichoir F (1985) "PAP" (Φ-ϱ-Z) procedure for improved quantitative microanalysis. In: Armstrong JT (ed) Microbeam Analysis. San Francisco, California, San Francisco Press, San Francisco, pp 104–106

Rapp RP, Watson EB (1986) Monazite solubility and dissolution kinetics: implications for the thorium and light rare earth chemistry of felsic magmas. Contrib Mineral Petr 94:304–316

Raison PE, Jardin R, Bouëxière, Konings RJM, Geisler T, Pavel CC, Rebizant J, Popa K (2008) Structural investigation of the synthetic CaAn(PO4)2 (An = Th and Np) cheralite-like phosphates. Phys Chem Miner 35:603–609

Sahoo S, Dhara S, Sivasubramanian V, Kalavathi S, Arora AK (2009) Phonon confinement and substitutioanl disorder in $Cd_{1-x}Zn_xS$ nanocrystals. J Raman Spectrosc 40:1050–1054

Salje EKH, Chrosch J, Ewing RC (1999) Is "metamictization" of zircon a phase transition? Am Mineral 84:1107–1116

Santos CC, Silva EN, Ayala AP, Guedes I, Pizani PS, Loong C-K, Boatner LA (2007) Raman investigations of rare earth orthovanadates. J Appl Phys 101:053511-1–053511-5

Schulz B, Brätz H, Bombach K, Krenn E (2007) In situ Th-Pb dating of monazite by 266 nm laser ablation and ICP-MS with a single collector, and its control by EMP analysis. Z Geol Wissenschaft 6:377–392

Seydoux-Guillaume A-M, Wirth R, Nasdala L, Gottschalk M, Montel JM, Heinrich W (2002) An XRD, TEM and Raman study of experimentally annealed natural monazite. Phys Chem Miner 29:240–253

Seydoux-Guillaume A-M, Wirth R, Deutsch A, Schärer U (2004) Microstructure of 24-1928 Ma concordant monazites; implications for geochronology and nuclear waste deposits. Geochim Cosmochim Ac 68:2517–2527

Seydoux-Guillaume A-M, Wirth R, Ingrin R (2007) Contrasting response of $ThSiO_4$ and monazite to natural irradiation. Eur J Mineral 19:7–14

Shannon RD (1976) Revised effective ionic radii and systematic studies of interatomic distances in halides and chalcogenides. Acta Crystallogr A 32: 751–767

Silva EN, Ayala AP, Guedes I, Paschoal CWA, Moreira RL, Loong C-K, Boatner LA (2006) Vibrational spectra of monazite-type rare-earth orthophosphates. Opt Mater 29:224–230

Spanier JE, Robinson RD, Zhang F, Chan S-W, Herman IP (2001) Size-dependent properties of CeO_{2-y} nanoparticles as studied by Raman scattering. Phys Rev B 64:245407

Terra O, Clavier N, Dacheux N, Podor R (2003) Preparation and characterization of lanthanum-gadolinium monazites as ceramics for radioactive waste storage. New J Chem 27:957–967

Többens DM, Kahlenberg V (2011) Improved DFT calculation of Raman spectra of silicates. Vib Spectrosc 56:265–272

Trocellier P (2000) Immobilization of radionuclides in single-phase crystalline waste forms: A review on their intrinsic properties and long term behaviour. Ann Chim-Sci Mat 25:321–337

Váczi T, Nasdala L, Wirth R, Mehofer M, Libowitzky E, Häger T (2009) On the breakdown of zircon upon "dry" thermal annealing. Miner Petrol 97:129–138

Van Emden B, Thornber MR, Graham J, Lincoln FJ (1997) The incorporation of actinides in monazite and xenotime from placer deposits in Western Australia. Can Mineral 35:95–104

Watt GR (1995) High-thorium monazite– (Ce) formed during disequilibrium melting of metapelites under granulite-facies conditions. Mineral Mag 59:735–743

Weber WJ, Ewing RC, Wang LM (1994) The radiation-induced crystalline-to-amorphous transition in zircon. J Mater Res 9:688–698

Weise C, van den Boogaart KG, Jonckheere R, Ratschbacher L (2009) Annealing kinetics of Kr-tracks in monazite: Implications for fission-track modelling. Chem Geol 260:129–137

Williams ML, Jercinovic MJ, Hetherington CJ (2007) Microprobe Monazite Geochronology: Understanding Geologic Processes by Integrating Composition and Chronology. Annu Rev Earth Pl Sci 35:137–175

Table 1 Natural monazite–(Ce) samples: Summary of origins and ages

Sample name	Location	Age (Ma)	Technique[a]	Age reference
Arendal	Arendal, Norway	930 ± 17	EPMA	Seydoux-Guillaume et al. 2007
Burnet	Burnet County, TX, U.S.A.	1096 ± 8	EPMA	M.J. Jercinovic, pers. comm.
D. Bory	Dolní Bory, Czech Republic	337 ± 2	TIMS	Novák et al. 1998
ECA6	Central Australia	369 ± 1	TIMS	A. Möller, unpublished data
Elk Mountain	San Miguel County, NM, U.S.A.	1391 ± 1	TIMS	Alagna et al. 2008
F6	Managoutry pass, Madagascar	560 ± 2	TIMS	A. Möller, unpublished data
FF	Madagascar	502 ± 15	EPMA	F. Finger, unpublished data
GM2	Itambé, Brazil	493 ± 6	TIMS	A. Möller, unpublished data
GM3	Itambé, Brazil	484 ± 3	TIMS	A. Möller, unpublished data
JUP	Juniper Flats, Riverside, CA, U.S.A.	101 ± 0.2	TIMS	A. Möller, unpublished data
Madmon	Madagascar	496 ± 10	SHRIMP	Schulz et al. 2007
Moacyr	Itambé, Brazil	506 ± 1	TIMS	Dumond et al. 2008
Moacir	Itambé, Brazil	474 ± 1	TIMS	Seydoux-Guillaume et al. 2002
MOM3	Ataleia, Brazil	450 ± 10	(U-Th)/He	Boyce et al. 2006
Namon	Braban Farm, Namibia	485 ± 4	SHRIMP	A. Kennedy, pers. comm.
Noe	Königsalm, Austria	334 ± 14	EPMA	Ertl et al., submitted
P1	Uluguru Mountains, Tanzania	655 ± 2	TIMS	Möller et al. 2000
SIV	Sivamalai, India	507 ± 1	TIMS	A. Möller, unpublished data
SL	Sri Lanka	491 ± 5	EPMA	A.-M. Seydoux-Guillaume, pers. comm.
VK-1	Madagascar	488 ± 1	SHRIMP	Fletcher et al. 2010

[a] Age determination techniques: EPMA = electron probe micro-analyser, TIMS = thermal ionization mass spectrometry, SHRIMP = sensitive high-resolution ion microprobe

Table 2 Chemical composition and Raman data for synthetic monazite-structure APO_4 samples

A-site cation(s)	Chemical formula[a]	Raman data[b]	
		Shift (cm^{-1})	FWHM[c] (cm^{-1})
Homogeneous samples			
Ce	$Ce_{1.01}P_{0.99}O_4$	970.4	2.3
Ce, Ca	$Ce_{0.98}Ca_{0.02}P_{0.99}O_4$	970.6	3.6
Ce, La	$Ce_{0.52}La_{0.49}P_{0.99}O_4$	968.9	2.4
Ce, Pr	$Pr_{0.51}Ce_{0.50}P_{0.99}O_4$	972.0	2.4
Ce, Nd	$Ce_{0.51}Nd_{0.50}P_{0.99}O_4$	973.5	2.4
Ce, Sm	$Ce_{0.52}Sm_{0.49}P_{0.99}O_4$	976.3	3.1
Sm	$SmPO_4$	981.3	2.6
Ce, Eu	$Ce_{0.51}Eu_{0.50}P_{0.99}O_4$	980.3	3.8
Ce, La, Nd	$Ce_{0.74}La_{0.14}Nd_{0.14}P_{0.99}O_4$	970.7	2.4
Interior regions inside heterogeneous samples			
Ce, Y	$Ce_{0.81}Y_{0.20}P_{0.99}O_4$	976.1	4.5
Ce, Y	$Ce_{0.70}Y_{0.31}PO_4$	978.6	5.0
Ce, Gd	$Gd_{0.52}Ce_{0.49}P_{0.99}O_4$	979.5	3.8
Ce, Gd	$Gd_{0.59}Ce_{0.41}PO_4$	980.7	4.0
Ce, Th	$Ce_{0.96}Th_{0.03}P_{0.99}O_4$	971.1	5.6
Ce, Th	$Ce_{0.94}Th_{0.05}P_{0.99}O_4$	971.5	7.5
Ce, La, Nd, Th	$Ce_{0.66}La_{0.14}Nd_{0.13}Th_{0.05}P_{0.99}O_4$	972.1	8.2
Ce, La, Nd, Th	$Ce_{0.62}Nd_{0.15}La_{0.12}Th_{0.08}PO_4$	973.0	10.5

[a] Calculated based on 4 oxygen atoms

[b] Raman data of the $\nu_1(PO_4)$ band of monazite

[c] Corrected for the apparatus function (Dijkman and van der Maas 1976)

Table 3 Results of EPMA and Raman analyses, and calculated alpha doses for natural monazite–(Ce) samples

Sample name	EPMA chemical analyses (wt.%)															(apfu)	Raman data[a]					α dose[d]
– spot	SiO_2	P_2O_5	CaO	Y_2O_3	PbO	La_2O_3	Ce_2O_3	Pr_2O_3	Nd_2O_3	Sm_2O_3	Gd_2O_3	Dy_2O_3	ThO_2	UO_2	Total	∑ Th, U, Ca, Pb	Shift (cm^{-1})		FWHM[b] (cm^{-1})			($\times 10^{19}$/g)
																	un-ann.	ann.	un-ann.	ann.	Δ[c]	
Homogeneous monazite–(Ce)[e]																						
Burnet	1.77	26.7	0.63	0.47	0.44	10.3	31.8	3.76	9.54	3.01	1.21	0.75	8.26	0.22	98.8	0.11	971.8	973.8	17.3	6.9	10.4	7.1
D. Bory	0.15	29.9	1.27	3.40	0.26	9.58	24.9	3.07	11.5	3.87	2.48	1.53	1.33	4.85	98.8	0.11	974.6	976.7	16.6	6.5	10.1	5.1
ECA6	0.59	28.8	0.94	2.17	bdl	11.1	25.7	3.32	14.2	3.26	2.41	0.88	5.35	0.32	99.0	0.09	973.1	975.8	14.3	6.5	7.8	1.7
Elk Mountain	2.11	26.4	0.84	0.65	0.66	10.3	24.5	3.05	11.1	4.25	2.80	1.79	9.76	0.28	98.3	0.14	973.3	975.5	16.9	8.0	8.9	10.8
F6	2.28	26.0	0.89	0.22	0.32	14.0	28.5	3.01	10.0	1.2	0.46	0.18	11.3	0.13	98.6	0.15	971.4	973.4	18.1	7.9	10.2	4.5
GM2	0.47	29.7	1.18	2.14	0.18	10.5	27.7	3.23	10.5	3.35	2.22	1.14	6.57	0.68	100.1	0.12	973.0	975.5	14.1	6.9	7.2	3.2
GM3	0.56	29.7	1.50	1.93	0.43	11.7	27.9	2.98	9.82	2.43	1.78	0.63	7.76	0.55	100.1	0.14	973.3	976.2	15.3	7.5	7.8	3.6
JUP	1.48	28.5	1.69	4.02	bdl	10.3	21.0	2.40	9.45	2.64	2.51	1.31	13.2	1.17	100.5	0.20	974.0	976.6	16.2	9.6	6.6	1.2
Madmon	3.13	24.7	0.16	1.18	0.34	6.90	23.8	3.81	15.3	4.96	2.31	0.40	11.4	0.43	98.9	0.12	972.8	975.1	18.8	7.7	11.1	4.5
Moacyr	1.30	27.6	0.48	1.39	0.16	14.7	29.7	3.28	11.2	1.97	0.81	0.28	6.19	0.08	99.1	0.08	971.2	973.7	14.3	6.3	8.0	2.3
Moacir	1.43	27.4	0.41	0.73	0.19	14.3	29.9	3.40	11.2	2.36	0.96	0.31	6.51	0.11	99.2	0.08	971.3	973.5	14.1	6.2	7.9	2.3
MOM3	1.46	27.3	0.42	1.51	0.14	10.7	28.0	3.63	13.1	3.63	2.00	n.a.	6.47	0.11	98.6	0.08	972.2	974.9	13.7	6.4	7.3	2.1
Namon	1.59	28.0	0.85	1.93	0.23	10.3	25.5	3.04	10.8	3.68	2.54	1.18	10.1	0.29	100.4	0.13	973.2	975.7	16.9	7.6	9.2	3.8
SIV	1.15	27.8	0.09	2.30	0.11	5.38	24.3	4.12	15.5	8.98	5.14	n.a.	4.23	0.24	99.3	0.05	973.9	976.7	12.7	5.4	7.3	1.8
SL	5.20	21.5	0.46	0.68	0.46	12.1	23.4	2.41	8.44	1.20	0.65	0.39	19.6	0.46	96.9	0.22	971.6	974.0	22.7	9.9	12.8	7.7
VK-1	1.71	27.9	1.73	2.63	0.36	11.1	24.0	2.48	7.87	2.21	1.59	1.08	14.2	0.82	100.2	0.21	973.4	976.1	19.6	9.7	9.9	5.9
Interior regions inside heterogeneous samples (only annealed samples were analysed)[f]																						
Arendal – a	1.14	28.3	0.92	2.72	bdl	12.0	26.6	3.34	11.7	2.72	1.52	0.81	6.15	0.61	99.0	0.10	–	975.2	–	7.0		5.8
Arendal – b	1.72	27.0	0.86	2.13	0.43	12.0	25.8	3.07	11.4	2.45	1.38	0.74	8.82	0.42	98.4	0.13	–	975.0	–	7.9		6.9
FF – a	0.48	28.4	0.05	0.62	bdl	8.04	28.1	4.52	18.0	6.36	3.15	0.26	1.69	0.04	99.9	0.02	–	974.2	–	4.1		0.6
FF – b	0.57	28.0	0.16	0.49	bdl	8.00	27.8	4.52	17.9	6.13	2.88	0.20	2.75	bdl	99.5	0.03	–	974.4	–	5.0		0.9
FF – c	2.17	26.0	0.16	1.59	0.22	7.05	24.4	4.03	15.8	5.60	2.77	0.44	7.82	0.40	98.6	0.09	–	975.5	–	6.7		3.3
Noe	0.15	29.8	1.63	3.13	0.11	11.6	25.9	3.03	11.2	2.45	1.65	0.99	6.59	0.46	98.9	0.13	–	975.8	–	7.3		1.9
P1 – a	0.12	29.7	0.52	1.24	bdl	16.8	30.6	3.47	12.2	1.74	1.15	n.a.	2.19	0.17	100.0	0.04	–	973.3	–	4.9		1.3
P1 – b	0.28	29.5	1.07	0.75	0.18	14.8	29.0	3.26	12.6	2.18	1.27	n.a.	4.45	0.36	99.9	0.09	–	973.9	–	5.9		2.7
P1 – c	0.57	28.9	2.30	0.16	0.30	11.9	25.7	3.08	12.5	2.00	0.92	n.a.	10.3	0.37	98.9	0.20	–	975.0	–	8.7		5.4
P1 – d	2.41	25.9	2.09	0.10	0.47	10.5	23.8	3.04	11.5	1.47	0.41	n.a.	16.0	0.44	98.1	0.25	–	974.9	–	10.2		8.1

Note: Analytical data for Eu_2O_3, Tb_2O_3, Ho_2O_3 and Er_2O_3 were below the detection limit or partly not available and are therefore not listed

bdl = not detected or below average detection limit

n.a. = not analysed

un-ann. = un-annealed; ann. = annealed

[a] Raman data of the $\nu_1(PO_4)$ band of monazite–(Ce)

[b] Corrected for the apparatus function (Dijkman and van der Maas 1976)

[c] Difference between $FWHM_{un\text{-}annealed}$ and $FWHM_{annealed}$

[d] Calculated according to Murakami et al. (1991) from actinide concentrations and age (cf. Table 1)

[e] Means of ≥ 8 individual analyses, made on several crystals

[f] Single point analyses

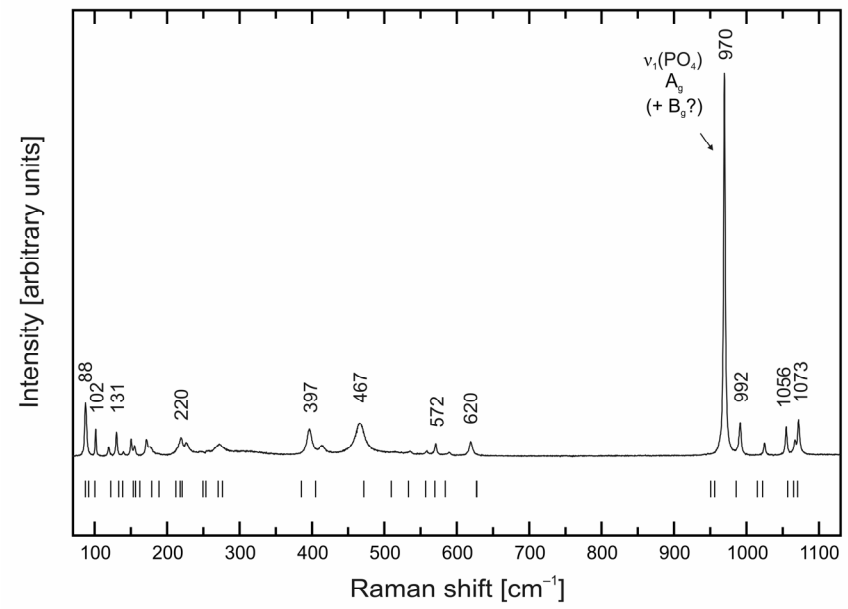

Fig. 1 Raman spectrum of synthetic monazite–(Ce). The spectrum is dominated by the intense $\nu_1(PO_4)$ band (symmetric stretching). Tick-marks represent the calculated vibrational modes

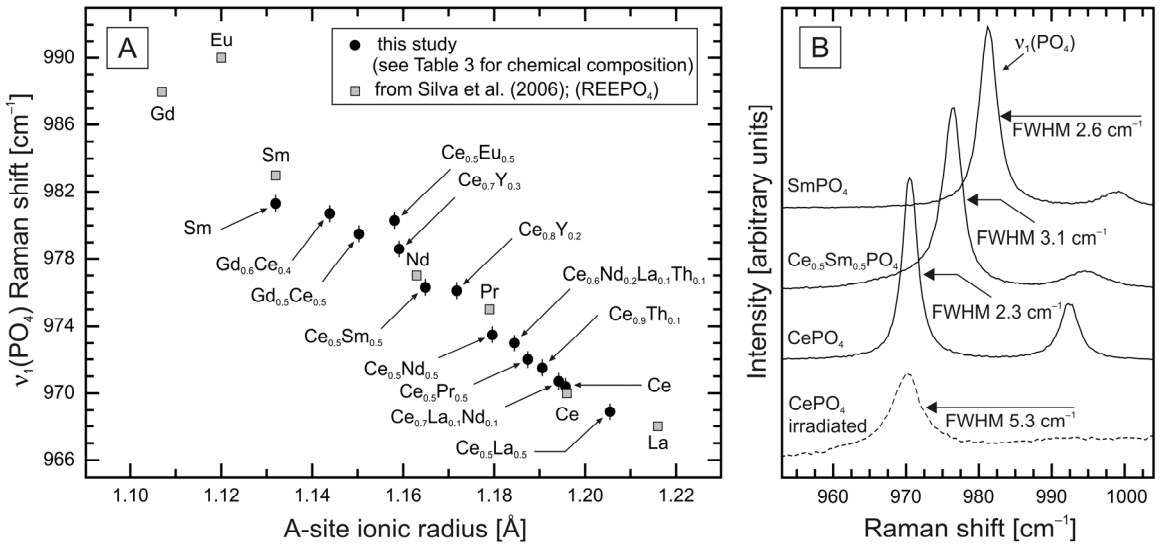

Fig. 2 (A) Correlation of the Raman shift of the $\nu_1(PO_4)$ band of synthetic monazite-structure APO_4 samples and their A-site ionic radius. For the syntheses produced in this study (circles), the A-site ionic radius plotted is an average for all A-site cations incorporated. Raman shift values for pure APO_4 end members (squares) were extracted from Silva et al. (2006). (B) Raman spectra (stacked) showing the PO_4 stretching region of synthetic (un-irradiated) $CePO_4$, $Ce_{0.5}Sm_{0.5}PO_4$ and $SmPO_4$ (solid), and irradiated $CePO_4$ (dashed). Note the strong chemical shift of the symmetric PO_4 stretching band and the influence of radiation damage on the band FWHM

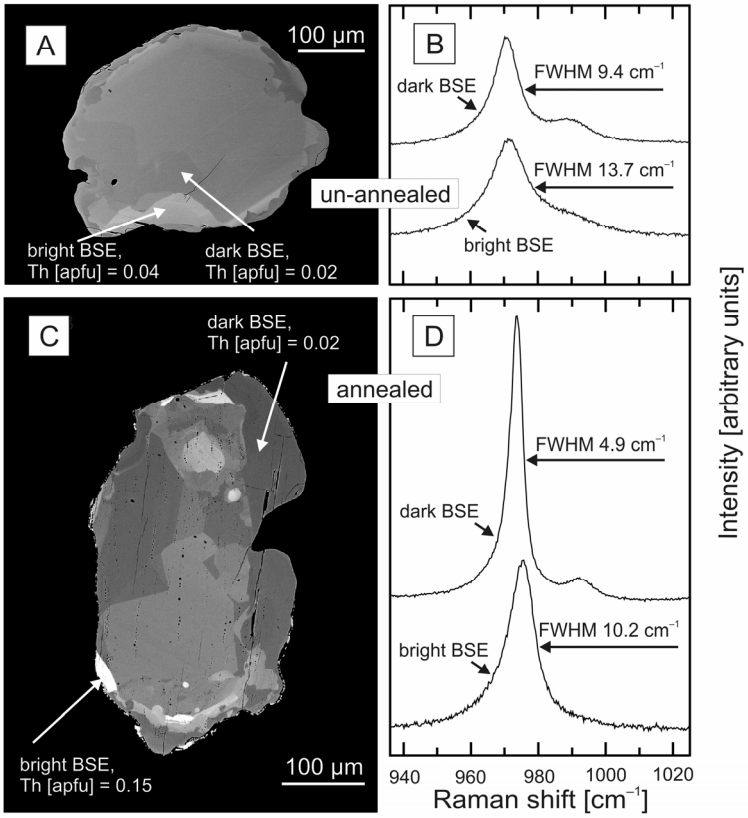

Fig. 3 Back-scattered electron images and Raman spectra of grains of the heterogeneous monazite–(Ce) P1 (Tanzania). (A) Un-annealed grain, BSE image. (B) Two corresponding Raman spectra (see arrows in A). Variations in spectra represent the combined effects of chemical composition and structural state. (C) Annealed grain, BSE image. (D) Two corresponding Raman spectra (see arrows in C). Note that variations in Figs. C-D are attributed solely to chemical heterogeneity. Contrast and brightness of the BSE images were adjusted individually

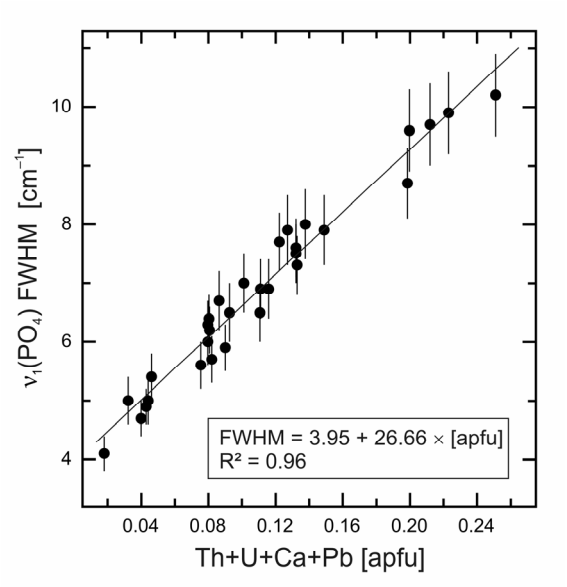

Fig. 4 Correlation of corrected FWHMs of the $\nu_1(PO_4)$ Raman band with the sum of Th, U, Ca, and Pb (apfu) for natural annealed monazite–(Ce) samples

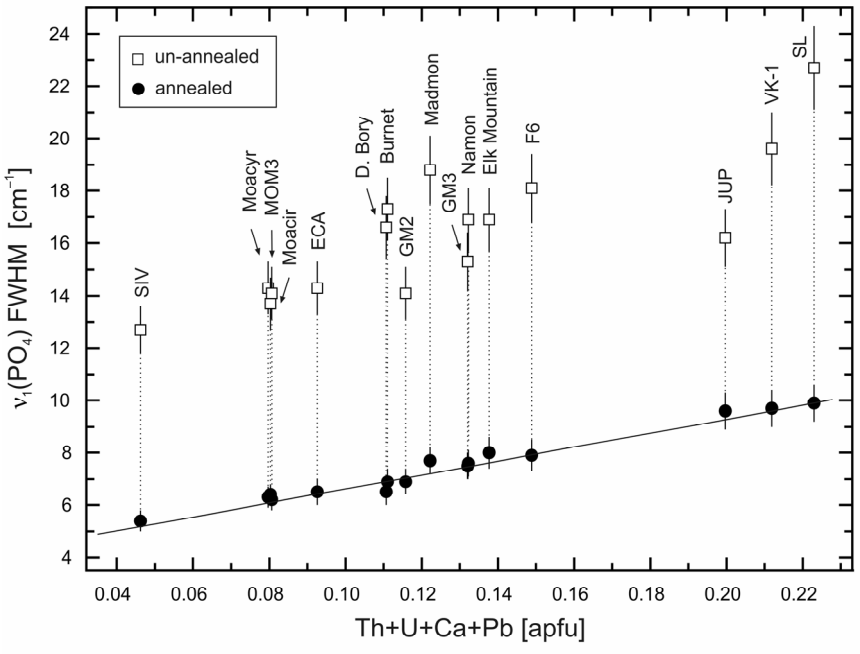

Fig. 5 Plot of corrected FWHMs of the $\nu_1(PO_4)$ Raman band versus the sum of Th, U, Ca, and Pb (apfu). Pairs of un-annealed monazite–(Ce) and their annealed analogues are shown. The FWHM difference within each data pair (dotted lines as visual guides) represents the degree of radiation damage (i.e., the structurally induced disturbance of the short-range order)

Supplementary material S1 for

A Raman spectroscopic study on the structural disorder of monazite–(Ce)

Katja Ruschel • Lutz Nasdala • Andreas Kronz • John M. Hanchar • Daniel M. Többens • Radek Škoda • Friedrich Finger • Andreas Möller

Table S1 Experimentally determined and calculated (DFT-calculations) Raman shift values of synthetic $CePO_4$

Raman shift experimental (cm^{-1})	Mode symmetry experimental[a]	Raman shift calculated (cm^{-1})	Mode symmetry calculated	Raman shift Δ[b] (cm^{-1})	Type[c]
		87	A_g		
88	B_g	92	B_g	-4	
102	A_g	101	A_g	1	
120	A_g/B_g	122	A_g	-2	
131	B_g	134	B_g	-3	
140		139	B_g	1	
151	A_g	157	A_g	-6	
155	B_g	154	B_g	1	
		163	A_g		
172	B_g	179	B_g	-7	
177	A_g	189	A_g	-12	
220	B_g	212	B_g	8	
		218	A_g		
227	B_g	221	B_g	6	
248		250	B_g	-2	
258	A_g	254	A_g	4	
		271	B_g		
273	A_g	277	A_g	-4	
397	B_g	386	B_g	11	
414	A_g	405	A_g	9	
467	A_g	472	A_g	-5	ν_2, b(O1–P–O2), b(O3–P–O4), symmetric
515		510	B_g	5	
536	A_g	534	A_g	2	
559		558	B_g	1	
572	A_g	570	A_g	2	
581	B_g	584	B_g	-3	
620	A_g/B_g	628	A_g	-8	ν_4, b(O1–P–O2), b(O3–P–O4), asymmetric
		628	B_g		
		951	B_g		
970	A_g	957	A_g	13	ν_1, s(P–O2), symmetric
992	A_g	986	A_g	6	
		1015	A_g		
1026	B_g	1023	B_g	3	
1056	A_g	1058	A_g	-2	ν_3, s(P–O1), s(P–O4), asymmetric
1068		1066	B_g	2	
1073	B_g	1071	B_g	2	

[a] From Begun et al. (1981) and Silva et al. (2006); the more specific declaration is quoted

[b] Δ = difference between experimentally determined and calculated Raman shift

[c] Atom numbers according to Beall et al. (1981)

Ab initio calculation procedure of the theoretical Raman spectrum of synthetic $CePO_4$: The calculation was done at Γ-point using 3D-periodic density functional theory and Gaussian basis sets, employing the program CRYSTAL 09 (Dovesi et al. 2009; Pascale et al. 2004). The level of numerical accuracy was set as described in Többens and Kahlenberg (2011), and a Pack-Monkhorst k net with 4×4×4 points in the Brillouin zone was used. The B3LYP functional (Becke 1993) was used, which in this case was found to perform slightly better than more modern functionals (Demichelis et al. 2010; Többens and Kahlenberg 2011). All-electron basis sets of the atoms were selected as follows: 1) for oxygen a 8-411G(11) contraction based on a 8-411G contraction (Towler et al. 1994); 2) for phosphorus a 85-211G(11) contraction based on a 85-21G(1) contraction (Zicovich-Wilson et al. 2002); and 3) for cerium the Stuttgart-Dresden ECP47MWB (Dolg et al. 1989, 1993) was modified into a ECP47-3s3p-11G(31) contraction. For these basis sets the exponents of the two most diffuse sp and d shells have been optimized to the following values: sp(O) = 0.458, 0.159, d(O) = 0.82, 0.167; sp(P) = 0.549, 0.255, d(P) = 2.68, 0.613 and sp(Ce) = 0.589, 0.254, d(Ce) = 0.13.

Note that some uncertainty remains for the assignments of 1) the calculated A_g and B_g modes at 628 cm^{-1} (the associated observed band at 620 cm^{-1} was experimentally determined to be either an A_g mode, a B_g mode or both modes); 2) the calculated B_g modes at 1066 cm^{-1} and 1071 cm^{-1} to the observed Raman bands at 1068 cm^{-1} and 1973 cm^{-1}; and 3) the calculated B_g modes at 134 cm^{-1} and 139 cm^{-1} to the observed Raman bands at 131 cm^{-1} and 140 cm^{-1}. In the latter two cases the observed Raman bands are too close to each other to allow a distinct assignment of the modes. Hence the correct assignments might in these cases be converse to the ones proposed in Table S1.

References

Beall GW, Boatner LA, Mullica DF, Milligan WO (1981) The structure of cerium orthophosphate, a synthetic analogue of monazite. J Inorg Nucl Chem 43:101–105

Becke, AD (1993) Density-functional thermochemistry. III The role of exact exchange. J Chem Phys 98:5648–5652

Begun GM, Beall GW, Boatner LA, Gregor WJ (1981) Raman Spectra of the Rare Earth Orthophosphates. J Raman Spectrosc 11:273–278

Demichelis R, Civalleri B, Ferrabone M, Dovesi R (2010) On the preference of eleven DFT functionals in the description of the vibrational properties of aluminosilicates. Int J Quantum Chem 110: 406–415

Dolg M, Stoll H, Savin A, Preuss H (1989) Energy-adjusted pseudopotentials for the rare earth elements. Theor Chim Acta 75:173–194

Dolg M, Stoll H, Preuss H (1993) A combination of quasirelativistic pseudopotential and ligand field calculations for lanthanoid compounds. Theor Chim Acta 85:441–450

Dovesi R, Saunders VR, Roetti C, Orlando R, Zicovich-Wilson CM, Pascala F, Civalleri B, Doll K, Harrison NM, Busch IJ, D'Arco P, Llunell M (2009) CRYSTAL09 – A computational tool for solid state chemistry and physiscs. University of Torino, Italy

Pascale F, Zicovich-Wilson CM, Lopez F, Civalleri B, Orlando R, and Dovesi R (2004) The calculation of the vibrational frequencies of crystalline compounds and its implementation in the CRYSTAL code. J Comput Chem 25:888–897

Silva EN, Ayala AP, Guedes I, Paschoal CWA, Moreira RL, Loong C-K, Boatner LA (2006) Vibrational spectra of monazite-type rare-earth orthophosphates. Opt Mater 29:224–230

Többens DM, Kahlenberg V (2011) Improved DFT calculation of Raman spectra of silicates. Vib Spectrosc 56:265–272

Towler MD, Allan NL, Harrison NM, Saunders VR, Mackrodt WC, Aprà E (1994) An ab initio Hartree-Fock study on MnO and NiO. Phys Rev B 50, 5041–5054

Zicovich-Wilson CM, Bert A, Roetti C, Dovesi R, Saunders VR (2002) Characterization of the electronic structure of crystalline compounds through their localized Wannier functions. J Chem Phys 116:1120–1127

Supplementary material S2 for

A Raman spectroscopic study on the structural disorder of monazite–(Ce)

Katja Ruschel • Lutz Nasdala • Andreas Kronz • John M. Hanchar • Daniel M. Többens • Radek Škoda • Friedrich Finger • Andreas Möller

Table S2 Reagents for the A-site cations in the syntheses experiments

A-site cation(s)	Reagent(s)
Ce	3.0 mol% CeO_2
Sm	1.5 mol% Sm_2O_3
Ce, REE[a]	2.0 mol% CeO_2 + 1.0 mol% REE_2O_3
Ce, Pr	2.0 mol% CeO_2 + 0.3 mol% Pr_6O_{11}
Ce, Ca	2.0 mol% CeO_2 + 2.0 mol% $CaCO_3$
Ce, Th	2.0 mol% CeO_2 + 2.0 mol% ThO_2
Ce, La, Nd	2.9 mol% CeO_2 + 0.3 mol% La_2O_3 + 0.3 mol% Nd_2O_3
Ce, La, Nd, Th	1.4 mol% CeO_2 + 0.2 mol% La_2O_3 + 0.2 mol% Nd_2O_3 + 2.0 mol% ThO_2

[a] REE = La, Nd, Sm, Eu, Gd or Y

Table S3 Results of EPMA analyses for synthetic monazite-structure APO_4 samples

A-site cation(s)	EPMA chemical analyses (wt.%)													
	SiO_2	P_2O_5	CaO	Y_2O_3	La_2O_3	Ce_2O_3	Pr_2O_3	Nd_2O	Sm_2O_3	Eu_2O_3	Gd_2O	ThO_2	UO_2	Total
Homogeneous samples[a]														
Ce	bdl	29.7	bdl	bdl	0.20	69.7	bdl	bdl	0.11	bdl	bdl	bdl	bdl	100.0
Ce, Ca	bdl	30.2	0.37	bdl	bdl	68.5	bdl	bdl	0.14	bdl	bdl	0.27[b]	bdl	99.7
Ce, La	bdl	29.8	bdl	bdl	34.0	36.0	bdl	bdl	0.10	bdl	bdl	bdl	bdl	100.0
Ce, Pr	bdl	29.5	bdl	bdl	bdl	34.7	35.0	bdl	bdl	bdl	bdl	bdl	bdl	99.2
Ce, Nd	bdl	29.3	bdl	bdl	bdl	35.1	bdl	35.5	bdl	bdl	bdl	bdl	bdl	100.1
Ce, Sm	bdl	29.1	bdl	bdl	bdl	35.4	bdl	bdl	35.4	bdl	bdl	bdl	bdl	100.0
Sm	bdl	28.8	bdl	bdl	bdl	0.02	bdl	bdl	71.4	bdl	bdl	bdl	bdl	100.3
Ce, Eu	bdl	29.1	bdl	bdl	bdl	34.3	bdl	bdl	bdl	36.5	bdl	bdl	bdl	100.0
Ce, La, Nd	bdl	29.5	bdl	bdl	9.34	29.5	bdl	9.70	bdl	bdl	bdl	bdl	bdl	99.7
Interior regions inside heterogeneous samples[c]														
Ce, Y	bdl	31.0	bdl	9.98	bdl	58.3	bdl	bdl	bdl	bdl	bdl	bdl	bdl	99.5
Ce, Y	bdl	32.6	bdl	15.9	bdl	52.8	bdl	bdl	0.12	bdl	bdl	bdl	bdl	101.5
Ce, Gd	bdl	28.7	bdl	bdl	bdl	28.7	bdl	bdl	bdl	bdl	38.0	bdl	bdl	99.5
Ce, Gd	bdl	28.4	bdl	bdl	bdl	28.4	bdl	bdl	bdl	bdl	42.6	bdl	bdl	98.3
Ce, Th	0.11	29.2	0.03	bdl	bdl	65.5	bdl	bdl	bdl	bdl	bdl	3.52	bdl	98.5
Ce, Th	0.11	29.1	0.03	0.15	bdl	64.1	bdl	bdl	bdl	bdl	bdl	5.01	bdl	98.6
Ce, La, Nd, Th	bdl	28.7	bdl	bdl	9.50	44.4	bdl	9.11	bdl	bdl	bdl	5.72	bdl	97.6
Ce, La, Nd, Th	bdl	28.8	bdl	bdl	8.10	41.3	bdl	10.4	bdl	bdl	bdl	8.64	bdl	97.1

bdl = not detected or below average detection limit

[a] Means of ≥ 8 individual analyses, made on several crystals

[b] Thorium was added unintentionally (probably slight contamination of the crucible)

[Pc] Single point analyses

2.6 Annealing behaviour of radiation-damaged minerals

This subchapter presents data that have not been published in refereed journals thus far. Some of the results have been included in poster presentations (Ruschel et al. 2007a, 2007b, 2008).

Introduction

The behaviour of radiation-damaged minerals upon thermal annealing was studied by means of Raman spectroscopy and laser-induced photoluminescence (PL). During annealing of radiation-damaged minerals typical changes are commonly observed in the Raman spectra, including variations in their Raman shifts (typically shifts toward higher wavenumbers), extensive decreases of their widths, and intensity gains. These changes reveal the increasing short-range order during heat treatment [see e.g., Nasdala et al. (1995) and subchapter 2.5 of this present thesis].

Photoluminescence spectra obtained from well-crystallised samples (e.g., produced upon annealing) commonly show sharper emission bands and higher emission intensities, when compared to spectra obtained from their radiation-damaged analogues. This is due to increased crystal field effects and indicates recovery of the short-range order during annealing [see e.g., luminescence studies in Nasdala et al. (2002) and Seydoux-Guillaume et al. (2002)].

Samples and experimental methods

The following minerals (end member formula in parentheses) were investigated: monazite–(Ce) ($CePOB_4$), fergusonite–(Y) ($YNbO_4$) and baddeleyite (ZrO_2). Two of the samples are already well characterised, namely monazite–(Ce) from Brazil (equates to "Moacir" from subchapter 2.5) and fergusonite–(Y) from Madagascar (equates to the sample studied in subchapter 2.3). In contrast, no additional information (e.g., concerning the chemical composition) is available for the studied baddeleyite sample from the Phalaborwa complex in South Africa.

For the annealing experiments either fractions of one crystal or several crystals of each sample were subjected to dry annealing experiments. The chips or grains (several hundred micrometres up to several millimetres in length) were placed individually in a platinum crucible and annealed in air for 96 hours. Annealing experiments (with 100°C steps) were done in the range 300–1400°C for monazite–(Ce) and fergusonite–(Y), whereas baddeleyite was annealed at 1100°C only. Samples were heated at a rate of 10°C/min. After an annealing run, the furnace switched off and samples were removed after the furnaces had cooled to room temperature. Chips of the untreated and the annealed natural specimens were prepared as doubly polished thin sections attached to a glass slide (thicknesses ~30 μm) with random crystallographic orientations.

Raman and laser-induced PL spectra were obtained in quasi back-scattering geometry using an edge-filter based Renishaw RM1000 system equipped with a Leica DMLM optical microscope (50× objective, numerical aperture 0.75) and Peltier-cooled, Si-based charge-coupled device (CCD) detector. The lateral resolution was ~4–5 μm. Photoluminescence spectra of all studied minerals

and Raman spectra of fergusonite–(Y) were excited with the 488 nm emission line of an Ar^+ laser (17 mW). The spectral resolution was ~5–6 cm^{-1} (which corresponds to 0.2 nm). Raman spectra of monazite–(Ce) and baddeleyite were excited with the 632.8 nm emission of a He–Ne laser (~8 mW). The spectral resolution was ~2.2 cm^{-1}. Band positions were calibrated using the Rayleigh line and neon lamp emission lines; the resulting wavenumber accuracy was better than 1 cm^{-1}.

Note that the observed Raman and emission bands depend on the sample orientation with respect to the polarisation plane of the laser light. As spectra were obtained from samples with random orientation, the relative intensities of the bands may show significant variations. Hence no quantitative comparison of intensities of individual bands in the various spectra is possible.

Results and discussion

For monazite–(Ce) and fergusonite–(Y) only a selection of the Raman and PL spectra obtained from the annealing products as well as the untreated material is shown in the Figs. 1A and B, respectively Figs. 2A and B. The Raman and PL spectra of the untreated monazite–(Ce) sample reveal distinct bands. This indicates that the material is not in a metamict state. Upon increase of the annealing temperature Raman and PL spectra of monazite–(Ce) show a stepwise increase in intensity and general sharpening of their bands. This indicates a gradual reconstitution of the short-range order. Furthermore the most dominant band of the monazite–(Ce) Raman spectrum, the symmetric PO_4 stretching band, shows a shift toward higher wavenumbers (for details see subchapter 2.5). Photoluminescence spectra are dominated by emission bands that can most probably be assigned to rare earth element (REE) emission centres (Sm^{3+}, Nd^{3+}, Pr^{3+}) (see e.g., Gaft et al. 2005; Ruschel et al. 2007a).

The Raman and PL spectra obtained from untreated fergusonite–(Y) show strongly broadened bands of extremely weak intensity, which lack any fine structure (Figs. 2A and B). This indicates that the material analysed is in a strongly radiation-damaged to fully metamict state. Photoluminescence spectra revealed that the main structural reorganisation (i.e., band sharpening and large intensity gain) occurs in the temperature range from 600°C to 800°C. The continuing sharpening of the emission bands between 800°C and 1300°C reflects the continuous improvement of the short range order. In the PL spectrum of the sample annealed at 1300°C, all emission bands have notable fine structures which are assigned to crystal-field effects in the recrystallised fergusonite–(Y). The PL spectra are dominated by trivalent REE emissions, mainly Er^{3+}, Pr^{3+}, Ho^{3+} and Tm^{3+} (Ruschel et al. 2007b). Structural reconstitution upon annealing is confirmed by Raman spectra. The Raman spectrum obtained after annealing at 1300°C corresponds reasonably well to a spectrum of a synthetic, fergusonite-type $YNbO_4$ phase (Yashima et al. 1997). Some additional information on the annealing of fergusonite–(Y) was obtained from X-ray diffraction patterns (including information on the transition from alpha- to beta-fergusonite) (see subchapter 2.3 for details).

For baddeleyite only a limited number of preliminary results is available (see Figs. 3A and B). The Raman spectrum of the untreated material shows distinct Raman bands. Upon annealing of the sample at 1100°C only minor changes (in particular slight decreases of band widths) are

observed in the spectra. The spectrum obtained at 1100°C corresponds very well to a spectrum of crystalline baddeleyite presented in Valdez et al. (2004). Note that the small band at ~261 cm^{-1} observed in the spectrum of the untreated baddeleyite has disappeared in the spectrum of the annealed fragment. The reverse case, the appearance of this band upon ion-irradiation experiments has been described in Valdez et al. (2004) and Simeone et al. (2000). The latter assigned the band to a tetrahedral baddeleyite phase produced upon ion irradiation. From the data obtained in this study, no conclusion about the cause of this band is possible. In contrast to the Raman spectrum, the PL spectrum of the untreated baddeleyite does not indicate any short-range order, whereas after annealing at 1100°C the emission bands are sharp and show high intensities. Main emission bands can most probably be assigned to Tb^{3+}, Nd^{3+}, Sm^{3+} and Dy^{3+} (Gaft et al. 2005).

However, these results show that for a better understanding of the annealing behaviour of this mineral, more annealing steps should be performed for baddeleyite. Furthermore a detailed characterisation of the sample including different analytical techniques is needed, such as the determination of the chemical composition. A heterogeneity of this sample cannot be excluded and might potentially also influence the comparability of the Raman and PL spectra obtained.

In spite of these limitations, the study confirms the suitability of Raman and PL spectroscopy to investigate the short-range order of minerals. Photoluminescence further allows to study trace element-related centres. Differences in the sensitivity of the two applied spectroscopic methods are obvious from the baddeleyite spectra, where the Raman spectrum obtained from the untreated material shows distinct bands, whereas in the corresponding PL spectrum no bands can be observed. The latter is assigned to luminescence suppression even at low levels of accumulated radiation damage.

The fine structure of PL emissions related to certain trace elements with 3*d* or 4*f* electronic structure is very sensitive to the host lattice. Emission spectra of a certain REE^{3+} may for instance vary significantly if the REE is incorporated at different crystallographic sites in different materials (Gaft et al. 2005). More detailed investigations are necessary for a precise and more sound interpretation of the obtained complex emission spectra.

The experiments show that the response to thermal annealing (i.e., the structural recovery) is material-specific. Natural monazite–(Ce), for instance, recovers its structure at relatively low temperatures over geologic time periods (Boatner and Sales 1988; Meldrum et al. 1998). Therefore, to the best of our knowledge natural monazite–(Ce) has never been found in the fully metamict state (Popa et al. 2007).

However, it should be noted that heat-treatment of radiation-damaged minerals does not always result in a gradual reconstitution of the original phase. The formation of another crystalline phase or the decomposition into several phases is also possible. Heavily metamict zircon, for instance, was shown to have an intermediate annealing stage, where it decomposes into different oxides. A fully recrystallised zircon was obtained only after annealing at 1250°C and above (Nasdala et al. 2002). Note that the recovery of the original phase might also be entirely prevented (e.g., due to an alteration process that changed the primary chemical composition).

Thanks are due to A. Kennedy for kindly providing the baddeleyite sample.

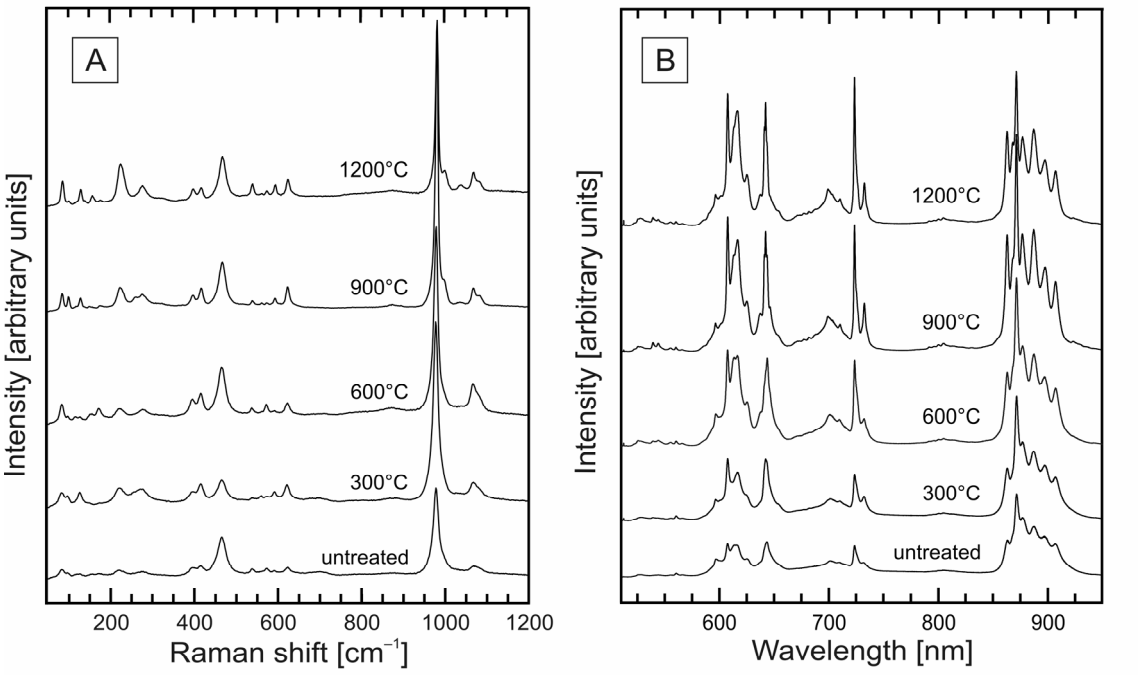

Fig. 1 Raman spectra (A) and PL spectra (B) for the untreated monazite–(Ce) and annealing products.

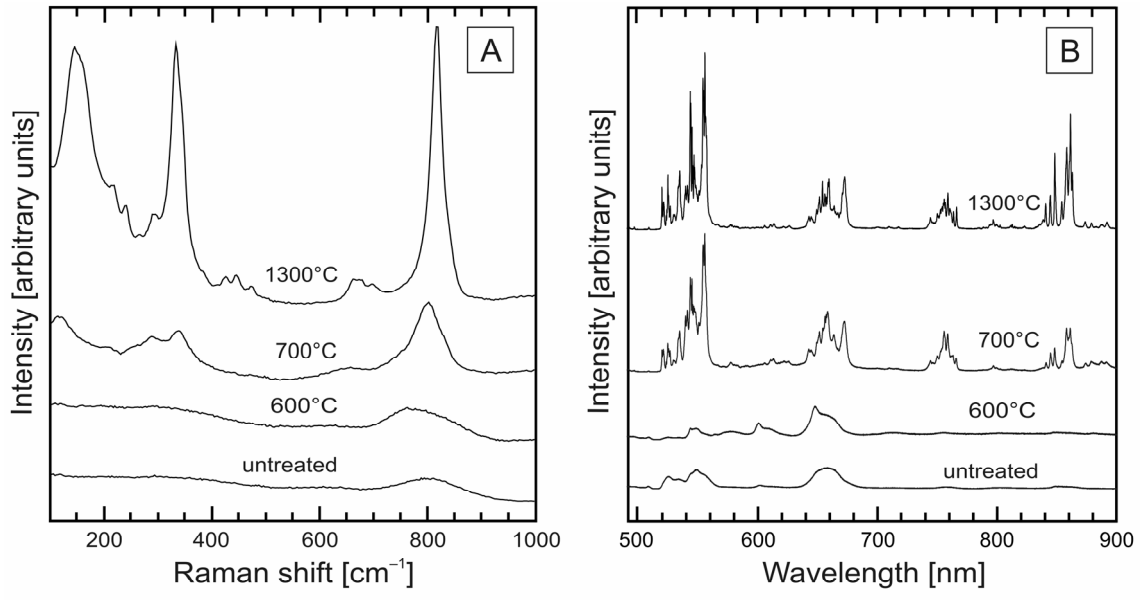

Fig. 2 Raman spectra (A) and PL spectra (B) for the untreated fergusonite–(Y) and annealing products.

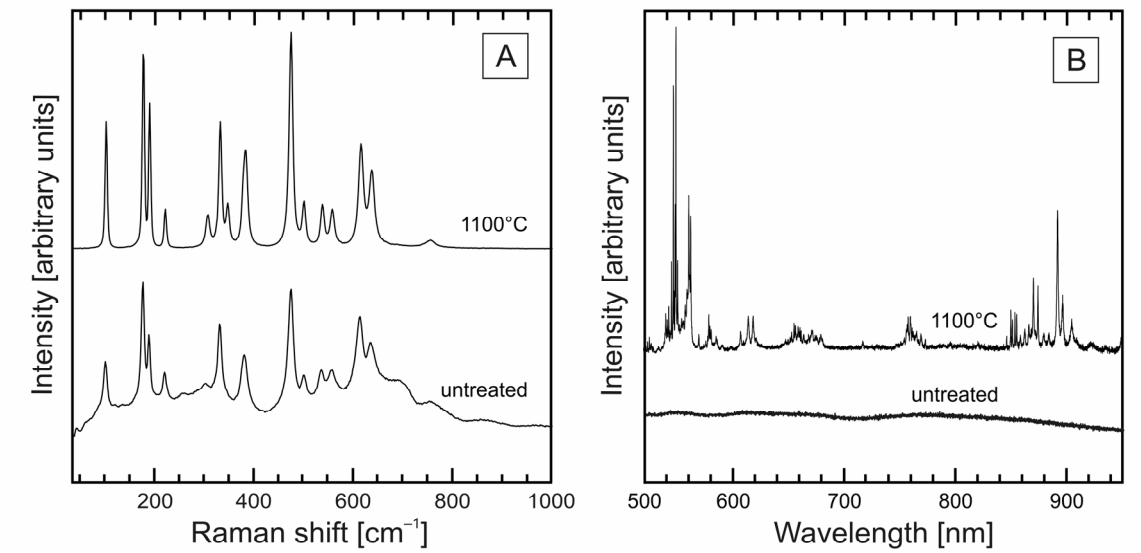

Fig. 3 Raman spectra (A) and PL spectra (B) for the untreated baddeleyite and a fragment annealed at 1100°C.

3 Final discussion and implications

For each individual study included in this thesis, results as well as a subsequent discussion are provided in detail in the respective subchapters 2.1–2.6. In the following part a summarising discussion of all results and their implications, as well as a short review on the suitability of some analytical methods used in studying radiation-damaged and potentially altered samples is presented.

The study reprinted in subchapter 2.1 shows that the degree of radiation damage in zircon can be estimated from the width of the Raman $\nu_3(SiO_4)$ band even under high pressure conditions. This allows, for instance, to estimate the degree of radiation damage of zircon inclusions in situ inside a host mineral, without significant influence of potential "fossilized pressures" or compressive strain acting on the inclusion. A potential application is, for instance, to recognise whether a host gemstone was subjected to heat treatment (i.e., thermal annealing) or not: The observation of significantly broadened Raman bands of zircon verifies radiation damage, which in turn allows one to exclude high-temperature treatment (because heating would have resulted in structural reconstitution, leading to narrow Raman bands).

In the study presented in subchapter 2.5, a method was developed to predict the effect of chemically-induced disorder on the FWHM of the monazite–(Ce) $\nu_1(PO_4)$ Raman band. The total band broadening affecting the Raman spectrum of a given natural monazite–(Ce) sample consists of chemically caused broadening (i.e., disturbance of the short-range order due to the incorporation of non-formula elements) and broadening due to structural disorder (i.e., radiation damage and/or stress). Provided the chemical composition of a natural monazite–(Ce) is known, the "chemical band broadening" can be used to estimate the degree of radiation damage from the observed FWHM of the $\nu_1(PO_4)$ band of that particular sample. This method might be useful to investigate the thermal history of monazite–(Ce) samples. Furthermore biased dating results can be avoided by pre-selecting less radiation-damaged (and potentially unaltered) crystals or interior regions within crystals for age determination. Nevertheless, future work should compile a quantitative calibration of irradiation effects on Raman spectral parameters in monazite–(Ce) using ion-irradiation experiments.

The monazite–(Ce) and fergusonite–(Y) samples studied in subchapters 2.2–2.4 suffered radiation-damage arising from the decay of the incorporated actinides and their daughter nuclei. The monazite–(Ce) crystals from Norway are only moderately radiation-damaged, while the fergusonite–(Y) samples from Madagascar and Italy are highly radiation-damaged. The monazite–(Ce) and the fergusonite–(Y) from Madagascar additionally show strong secondary alteration textures. This points to complex chemical and thermal post-growth alteration histories in both cases. The monazite–(Ce) specimens even turned out to be "pseudomorphs" of a multi-phase composite after primary monazite–(Ce) crystals. The presumable multi-step alteration was in both samples caused by fluid-driven replacement reactions. The fractures in the crystal are likely to have served as "fast migration pathways" for the alteration fluids, which is particularly obvious in case of the fergusonite–(Y) sample. Regarding the implications for geochronology and the development of radioactive waste forms, it is especially of interest to study the potential mobility of radionuclides in

radiation-damaged minerals, particularly if the minerals have been affected by a fluid-driven replacement reaction.

In the monazite–(Ce) specimens, Th was extensively released from the primary monazite–(Ce) into the alteration fluid and locally redeposited in fracture fillings. This process, as well as the incorporation of high amounts of common Pb in the monazite–(Ce) structure, resulted in the disturbance of the U–Th–Pb system during the alteration. Due to the notably biased isotopic ratios, no reliable radiometric age value could be obtained. The observations question the stability and alteration-resistance of orthophosphate phases, contrary to earlier studies (e.g., Terra et al. 2003; Poitrasson et al. 2004). The results obtained in this present study indicate that the behaviour of monazite–(Ce) largely depends on the environmental conditions this mineral is exposed to. Further critical performance assessment of monazite–(Ce) as potential ceramic host phase for the long-term immobilisation of radioactive waste appears crucial.

In contrast to monazite–(Ce), fewer studies were done to date on the stability and alteration behaviour of fergusonite–(Y) (e.g., Janeczek, 2004). To the best of our knowledge, the study on the fergusonite–(Y) sample from Madagascar (subchapter 2.3) provides the first detailed characterisation of natural fergusonite–(Y) that was affected by a low-T hydrothermal overprint. Though this sample has experienced heavy chemical alteration, the concentrations of U and Th remained almost constant. This suggests that the actinides were not preferentially released in the alteration fluid, which seems in turn to support the suitability of the fergusonite-group minerals to be included in ceramics for the immobilisation of nuclear waste.

For the fergusonite–(Y) specimens from Adamello (subchapter 2.2) it remains unclear whether an alteration process had occurred or not. A few indications of a fluid-driven alteration process are discussed in the study. Many Th-rich uraninite inclusions, which probably nucleated spontaneously after metamictisation, are present in these samples. Their occurrence indicates that fergusonite–(Y) is able to retain actinides even when it is entirely metamict. Hence this study also suggests fergusonite–(Y) as a potential host phase for the long-term immobilisation of nuclear waste. However, for the fergusonite–(Y) sample from Madagascar as well as for the sample from Italy some observations remain difficult to interpret [e.g., the absence of pores in altered material compared to the occurrence of the pores in the "primary" host (subchapter 2.3); or the origin of nanometre-sized pores (subchapter 2.2)]. These observations might be starting points for further studies.

In summary, these three latter case studies on natural minerals strongly indicate that further investigations on a larger number of radiation-damaged and potentially hydrothermally altered mineral samples need to be carried out. Observations on natural samples are able to provide information on the long-term accumulation of radiation damage in minerals and on the behaviour of the minerals during long-term alteration processes. Comparable information can not be obtained from short-term laboratory experiments.

Concerning the study on the annealing behaviour of different minerals (subchapter 2.6) preliminary data are presented only. They indicate that additional annealing experiments need to be performed for baddeleyite. However, it should be noted that heat-treatment of a radiation-damaged mineral does not necessarily result in the recovery of the mineral's original crystal structure. The

formation of another crystalline phase or the decomposition into several phases is also possible (see e.g., Nasdala et al. 2002). Particularly in cases where, due to an alteration process, the chemical composition of the material to be annealed differs from its primary composition, the recovery of the original phase might be prevented. This has to be considered whenever a structural characterisation is performed after annealing of a radiation-damaged material in the laboratory (see e.g., subchapter 2.3). However, annealing proved to be a suitable method for the recovery of monazite–(Ce) samples (subchapter 2.5), which did not seem to have suffered significantly from any alteration and which were only radiation-damaged moderately.

Electron probe microanalysis (EPMA) turned out again to be a most suitable in-situ technique to investigate the chemical composition of a mineral. This technique was applied in the studies in subchapters 2.2–2.5. An EPMA may additionally be used to generate high-resolution element distribution maps. These maps proved to be in particular useful for the evaluation of alteration effects as they show the complexity of the compositional changes. For instance, the observation of sharp boundaries between the altered areas and their neighbouring host provided an indication for a fluid-driven alteration process in the two studies reprinted in subchapters 2.3 and 2.4.

To study the structural state of tiny samples or zones in minerals, transmission electron microscopy (TEM) and Raman spectroscopy are, due to their high spatial resolution, very suitable techniques. A TEM allows one to record a variety of images, such as bright field (BF) and dark field (DF) images, high resolution TEM (HRTEM) images, as well as selected area electron diffraction patterns (SAED). In the scanning TEM (STEM) mode high resolution images, which show compositional contrast, the so-called HAADF images, can be generated using a high-angle annular dark-field (HAADF) detector. A STEM that is equipped with an energy-dispersive X-ray (EDX) spectrometer further allows element analysis with the resolution of a few nanometres through the collection of EDX line scans and EDX-STEM element distribution maps. The imaging methods and the element analysis of a STEM were applied partly in the three case studies reported in subchapters 2.2–2.4. The TEM proved to be a very suitable technique for the detailed characterisation of radiation-damaged material as well as for altered material. Compared to the sample preparation that was needed for TEM analyses (e.g., using the focused ion beam technique) only minor sample preparation was needed for Raman spectroscopic analyses.

For the present work, Raman spectroscopy proved to be an important method regarding its suitability to study the short-range order of a material. The sensitivity of photoluminescence to probe the short-range order of a mineral is shown in subchapters 2.3 and 2.6. As both of these spectroscopic techniques have a spatial resolution on a micrometre scale, they are very well suitable and hence recommended for future studies on radiation-damaged and potentially altered minerals.

4 References

Bakker, K., Hein, H., Konings, R.J.M., van der Laan, R.R., Matzke, Hj. & van Vlaanderen, P. (1998): Thermophysical property measurements and ion-implantation studies on $CePO_4$. *Journal of Nuclear Materials*, 252:228–234.

Boatner, L.A. & Sales, B.C. (1988): Monazite. *In* Lutze, W. & Ewing, R.C. (eds.): Radioactive waste forms for the future. Elsevier, New York, pp 495–564.

Chakoumakos, B.C., Murakami, T., Lumpkin, G.R. & Ewing, R.C. (1987): Alpha-decay–induced fracturing in zircon: The transition from the crystalline to the metamict state. *Science*, 236:1556–1559.

Chakoumakos, B.C., Oliver, W.C., Lumpkin, G.R. & Ewing, R.C. (1991): Hardness and elastic modulus of zircon as a function of heavy-particle irradiation dose: I. In situ α-decay event damage. *Radiation Effects and Defects in Solids*, 118:393–403.

Cherniak, D.J. & Watson, E.B. (2003): Diffusion in zircon. *In* Hanchar, J.M. & Hoskin, P.W.O. (eds.): Zircon. *Reviews in Mineralogy and Geochemistry*, 53:113–143.

Dijkman, F.G. & van der Maas, J.H. (1976): Dependence of Bandshape and Depolarization Ratio on Slitwidth. *Applied Spectroscopy*, 30:545–546.

Ewing, R.C. (1994): The metamict state: 1993 – the centennial. *Nuclear Instruments and Methods in Physics Research B*, 91:22–29.

Ewing, R.C. (1999): Nuclear waste forms for actinides. *Proceedings of the National Academy of Sciences of the United States of America*, 96:3432–3439.

Ewing, R.C., Meldrum, A., Wang, L., Weber, W.J. & Corrales, L.R. (2003): Radiation effects in zircon. *In* Hanchar, J.M. & Hoskin, P.W.O. (eds.): Zircon. *Reviews in Mineralogy and Geochemistry*, 53:387–425.

Ewing, R.C. (2005): Plutonium and "minor" actinides: safe sequestration. *Earth and Planetary Science Letters*, 229:165–181.

Gaft, M., Reisfeld, R., & Panczer, G. (2005): Modern Luminescence Spectroscopy of Minerals and Materials. 356 p. Springer-Verlag, Berlin-Heidelberg.

Geisler, T., Pidgeon, R.T., van Bronswijk, W. & Pleysier, R. (2001): Kinetics of thermal recovery and recrystallization of partly metamict zircon: a Raman spectroscopic study. *European Journal of Mineralogy*, 13:1163–1176.

Goncalves, P., Williams, M.L. & Jercinovic, M.J. (2005): Electron-microprobe age mapping of monazite. *American Mineralogist*, 90:578–585.

Harrison, T.M., Catlos, E.J. & Montel, J.-M. (2002): U–Th–Pb dating of Phosphate Minerals. *In* Kohn, M.L., Rakovan., J. & Hughes, J.M. (eds.): Phosphates. *Reviews in Mineralogy and Geochemistry*, 48:523–558.

Holland, H.D. & Gottfried, D. (1955): The effect of nuclear radiation on the structure of zircon. *Acta Crystallographica*, 8:291–300.

Horie, K., Hidaka, H. & Gauthier-Lafaye, F. (2006): Elemental distribution in zircon: Alteration and radiation-damage effects. *Physics and Chemistry of Earth*, 31:587–592.

Lee, J.K.W. & Tromp, J. (1995): Self-induced fracture generation in zircon. *Journal of Geophysical Research: Solid Earth*, 100:17753–17770.

Lenting, C., Geisler, T., Gerdes, A., Kooijman, E., Scherer, E.E. & Zeh, A. (2010): The behavior of the Hf isotope system in radiation-damaged zircon during experimental hydrothermal alteration. *American Mineralogist*, 95:1343–1348.

Lumpkin, G.R. & Ewing, R.C. (1995): Geochemical alteration of pyrochlore group minerals: pyrochlore subgroup. *American Mineralogist*, 80:732–743.

Lumpkin, G.R. (2001): Alpha-decay damage and aqueous durability of actinide host phases in natural systems. *Journal of Nuclear Materials*, 289:136–166.

Lumpkin, G.R. (2006): Ceramic Waste Forms for Actinides. *Elements*, 2:365–372.

Janeczek, J. (2004): Re-examination of kochelite: a mixture of metamict fergusonite-(Y) and altered zircon. *Neues Jahrbuch für Mineralogie – Monatshefte*, 5:193–207.

Krickl, R., Nasdala, L., Götze, J., Grambole, D. & Wirth, R. (2008): Alpha irradiation effects in SiO_2. *European Journal of Mineralogy*, 20:517–522.

Kuiper, Y.D. (2005): Isotopic age constraints from electron microprobe U-Th-Pb dates, using a three-dimensional concordia diagram. *American Mineralogist*, 90:586–591.

Markwort, L., Kip, B., Dasilva, E. & Roussel, B. (1995): Raman imaging of heterogeneous polymers: A comparison of global versus point illumination. *Applied Spectroscopy*, 49:1411–1430.

Meldrum, A., Boatner, L.A. & Ewing, R.C. (1997): Displacive radiation effects in the monazite- and zircon-structure orthophosphates. *Physical Review B*, 56:805–814.

Meldrum, A., Boatner, L.A., Weber ,W.J. & Ewing, R.C. (1998): Radiation damage in zircon and monazite. *Geochimica et Cosmochimica Acta*, 62:2509–2520.

Meldrum, A., Boatner, L.A. & Ewing, R.C. (2000): A comparison of radiation effects in crystalline ABO_4-type phosphates and silicates. *Mineralogical Magazine*, 64:185–194.

Montel, J.M. (2011): Minerals and design of new waste forms for conditioning nuclear waste. *Comptes Rendus Geoscience*, 343:230–236.

Murakami, T., Chakoumakos, B.C., Ewing, R.C., Lumpkin, G.R. & Weber, W.J. (1991): Alpha-decay event damage in zircon. *American Mineralogist*, 76:1510–1532.

Nasdala, L., Irmer, G. & Wolf, D. (1995): The degree of metamictization in zircon: a Raman spectroscopic study. *European Journal of Mineralogy*, 7:471–478.

Nasdala, L., Wenzel, M., Vavra, G., Irmer, G., Wenzel, T. & Kober, B. (2001): Metamictisation of natural zircon: accumulation versus thermal annealing of radioactivity-induced damage. *Contributions to Mineralogy and Petrology*, 141:125–144.

Nasdala, L., Lengauer C.L., Hanchar J.M., Kronz A., Wirth R., Blanc P., Kennedy A.K. & Seydoux-Guillaume A.-M. (2002): Annealing radiation damage and the recovery of cathodoluminescence. *Chemical Geology*, 191:121–140.

Nasdala, L., Reiners, P.W., Garver, J.I., Kennedy, A.K., Stern, R.A., Balan, E. & Wirth, R. (2004): Incomplete retention of radiation damage in zircon from Sri Lanka. *Amercian Mineralogist*, 89:219–231.

Nasdala, L., Wildner, M., Wirth, R., Groschopf, N., Pal, D.C. & Möller, A. (2006): Alpha particle haloes in chlorite and cordierite. *Mineralogy and Petrology*, 86:1–27.

Nasdala, L., Hanchar, J.M., Rhede, D., Kennedy, A.K. & Váczi, T. (2010): Retention of uranium in complexly altered zircon: An example from Bancroft, Ontario. *Chemical Geology*, 269:290–300.

Nasdala, L., Grambole, D., Götze, J., Kempe, U. & Váczi, T. (2011): Helium irradiation study on zircon. *Contributions to Mineralogy and Petrology*, 161:777–789.

Omel'yanenko, B., Livshits, T., Yudintsev, S. & Nikonov, B. (2007): Natural and artificial minerals as matrices for immobilization of actinides. *Geology of Ore Deposits*, 49:173–193.

Ouchani, S., Dran, J.-C. & Chaumont, J. (1997): Evidence of ionization annealing upon helium-ion irradiation of pre-damaged fluorapatite. *Nuclear Instruments and Methods in Physics Research B*, 132:447–451.

Picot, V., Deschanels, X., Peuget, S., Glorieux, B., Seydoux-Guillaume, A.-M. & Wirth, R. (2008): Ion beam radiation effects in monazite. *Journal of Nuclear Materials*, 381:290–296.

Peucat, J.-J., Capdevila, R., Drareni, A., Choukroune, P., Fanning, C.M., Bernard-Griffiths, J. & Fourcade, S. (1996): Major and trace element geochemistry and isotope (Sr, Nd, Pb, O) systematics of an Archaean basement involved in a 2.0 Ga very high-temperature (1000 °C) metamorphic event: In Ouzzal Massif, Hoggar, Algeria. *Journal of metamorphic Geology*, 14:667–692.

Poitrasson, F., Oelkers, E., Schott, J. & Montel, J.-M. (2004): Experimental determination of synthetic $NdPO_4$ monazite end-member solubility in water from 21°C to 300°C: Implications for rare earth element mobility in crustal fluids. *Geochimica et Cosmochimica Acta*, 68:2207–2221.

Popa, K., Bregiroux, D., Konings, R.J.M., Gouder, T., Popa, A.F., Geisler, T. & Raison, P.E. (2007): The chemistry of the phosphates of barium and tetravalent cations in the 1:1 stoichiometry. *Journal of Solid State Chemistry*, 180:2346–2355.

Putnis, A. (2002): Mineral replacement reactions: from macroscopic observations to microscopic mechanisms. *Mineralogical Magazine*, 66:689–708.

Raman, C.V. & Krishnan, K.S. (1928): A new type of secondary radiation. *Nature*, 121:501–502.

Ruschel, K., Nasdala, L., Finger, F., Kinny, P. & Seydoux-Guillaume, A.M. (2007a): Annealing radiation damage in monazite: changes in photoluminescence and Raman spectra. (Abstract). Programme with Abstracts, 6th European Conference on Mineralogy and Spectroscopy, Stockholm, Sweden, p. 70.

Ruschel, K., Nasdala, L., Gaft, M., Schnier, C. & Schlüter, J. (2007b): Photoluminescence recovery upon annealing of fergusonite. Abstract Volume, 17th Goldschmidt Conference, Köln, Deutschland, p. A861.

Ruschel, K., Nasdala, L. & Lengauer, C.L. (2008): Annealing behaviour of natural monazite compared to other radiation-damaged minerals. 8th International Conference on Raman Spectroscopy Applied to the Earth Sciences – Sensu Latu, Ghent, Belgium, Book of Abstracts, p. 114.

Seydoux-Guillaume, A.-M., Wirth, R., Nasdala, L., Gottschalk, M., Montel, J.M. & Heinrich, W. (2002): An XRD, TEM and Raman study of experimentally annealed natural monazite. *Physics and Chemistry of Minerals*, 29:240–253.

Simeone, D., Bechade, J.L., Gosset, D., Chevarier, A., Daniel, P., Pilliaire, H. & Baldinozzi, G. (2000): Investigation on the zirconia phase transition under irradiation. *Journal of Nuclear Materials*, 281:171–181.

Suzuki, K., Adachi, M. & Kajizuka, I. (1994): Electron microprobe observations of Pb diffusion in metamorphosed detrital monazites. *Earth and Planetary Science Letter*s, 128:391–405.

Terra, O., Clavier, N., Dacheux, N. & Podor, R. (2003): Preparation and characterization of lanthanum-gadolinium monazites as ceramics for radioactive waste storage. *New Journal of Chemistry*, 27:957–967.

Trocellier, P. (2000): Immobilization of radionuclides in single-phase crystalline waste forms: A review on their intrinsic properties and long term behaviour. *Annales de Chimie - Science des Matériaux*, 25:321–337.

Tromans, D. (2006): Solubility of crystalline and metamict zircon: A thermodynamic analysis. *Journal of Nuclear Materials*, 357:221–233.

Valdez, J.A., Tang, M., Chi, Z., Peters, M.I. & Sickafus, K.E. (2004): Characterization of an ion irradiation induced phase transformation in monoclinic zirconia. *Nuclear Instruments and Methods in Physics Research B*, 218:103–110.

Weber, W.J., Ewing, R.C., Catlow, C.R.A., de la Rubia, T.D., Hobbs, L.W., Kinoshita, C., Matzke, H., Motta, A.T., Nastasi, M., Salje, E.K.H., Vance, E.R. & Zinkle, S.J. (1998): Radiation effects in crystalline ceramics for the immobilization of high-level nuclear waste and plutonium. *Journal of Materials Research*, 13:1434–1484.

Weber, W.J., Navrotsky, A., Stefanovsky, S., Vance, E.R. & Vernaz, E. (2009): Materials science of high-level nuclear waste immobilization. *Materials Research Bulletin*, 34:46–53.

Williams, K.P.J., Pitt, G.D., Batchelder, D.N. & Kip, B.J. (1994): Confocal raman microspectroscopy using a stigmatic spectrograph and CCD detector. *Applied Spectroscopy*, 48:232–235.

Yashima, M., Lee, J.-H., Kakihana, M. & Yoshimura, M. (1997): Raman spectral characterization of existing phases in the Y_2O_3–Nb_2O_5 system. *Journal of Physics and Chemistry of Solids*, 58:1593–1597.

Zhang, M., Salje, E.K.H., Bismayer, U., Groat, L.A. & Malcherek, T. (2002): Metamictization and recrystallization of titanite: An infrared spectroscopic study. *American Mineralogist*, 87:882–890.

Acknowledgements

This thesis would not have been possible without the support of many people:

I particularly thank my supervisor Lutz Nasdala for his support, encouragement and inspiration within the last years. I am grateful for fruitful scientific discussions, for teaching me how to write scientific papers and for providing me with the opportunity to attend to international conferences.

Many thanks also to Manfred Wildner and Zdeněk Losos for the agreement to review this thesis.

This is also a good opportunity to express my thanks to John M. Hanchar for the support and hospitality through my stay at the Memorial University of Newfoundland.

Thank you to Andreas Ertl and Peter Valley for improving the English style of this thesis.

My special gratitude goes to the staff members and colleagues at the Institut für Mineralogie and Kristallographie for all help and the friendly working atmosphere. Explicitly I would like to thank Christian Lengauer, Eugen Libowitzky and Michael Götzinger for assistance with various analytical methods, Andreas Wagner for the excellent sample preparation, and Wolfgang Zirbs and Thomas Rosen for assistance with computer problems.

I would also like to say a big thank you to my friends for their support and understanding, with particular thanks to Björn.

Finally, I thank my parents for every support and encouragement during all my studies.

Contribution to the publications

Nasdala, L., Miletich, R., Ruschel, K. & Váczi, T. (2008): Raman study of radiation-damaged zircon under hydrostatic compression. *Physics and Chemistry of Minerals*, 35:597–602.

- Acquisition and interpretation of Raman spectroscopic data
- Assistance with preparation of the manuscript for publication

Gieré, R., Williams, C.T., Wirth, R. & Ruschel, K. (2009): Metamict fergusonite–(Y) in a spessartine-bearing granitic pegmatite from Adamello, Italy. *Chemical Geology,* 261:333–345.

- Acquisition and interpretation of the Raman spectroscopic data
- Discussion of results
- Assistance with preparation of the manuscript for publication

Ruschel, K., Nasdala, L., Rhede, D., Wirth, R., Lengauer, C.L. & Libowitzky, E. (2010): Chemical alteration patterns in metamict fergusonite. *European Journal of Mineralogy,* 22:425–433.

- Concept
- Acquisition of images (optical and scanning electron microscopy)
- Performance of annealing experiments
- Acquisition and interpretation of the spectroscopic data (Raman, photoluminescence and infrared spectroscopy)
- Assistance with the transmission electron microscope (Potsdam)
- Data interpretation
- Preparation of the manuscript for publication

Nasdala, L., Ruschel, K., Rhede, D., Wirth, R., Kerschofer-Wallner, L., Kennedy, A.K., Kinny, P.D., Finger, F. & Groschopf, N. (2010): Phase Decomposition upon Alteration of Radiation-Damaged Monazite–(Ce) from Moss, Østfold, Norway. *Chimia,* 64:705–711.

- Acquisition of images (optical and scanning electron microscopy)
- Acquisition and interpretation of Raman spectroscopic data
- Discussion of results
- Assistance with preparation of the manuscript for publication

Ruschel, K., Nasdala, L., Kronz, A., Hanchar, J.M., Többens, D.M., Škoda, R., Finger, F. & Möller, A. (2011): A Raman spectroscopic study on the radiation damage of monazite–(Ce). Submitted to *Mineralogy and Petrology*.

- Preparation of the synthetic orthophosphates (Memorial University, St. John`s)
- Performance of annealing experiments
- Acquisition and interpretation of Raman spectroscopic data
- Assistance with electron probe microanalyses (Göttingen)
- Data interpretation
- Preparation of the manuscript for publication

Curriculum Vitae

Personal information

Name	Katja Ruschel
Date of birth	18/11/1977
Place of birth	Boppard, Germany
Nationality	German

Education

since 04/2006	Institute of Mineralogy and Crystallography, University of Vienna, Austria, PhD student including two month at the Memorial University of Newfoundland, St. John's, Canada
27.06.2005	Diploma examination in Mineralogy
10/2001 – 06/2005	Institute for Geosciences, Johannes Gutenberg-University Mainz, Studies of Mineralogy Specialisation in Crystallography, General and Applied Mineralogy, Geology, Anorganic Chemistry Diploma thesis: „Mineralogische Untersuchungen zur Veränderung der Materialeigenschaften von Tansanit“
10/1997 – 09/2001	Institute for Geosciences, Johannes Gutenberg-University Mainz, Studies of Geology including six months at the Universität von Oviedo, Spain

Research experience

09/2005 – 03/2006	Center of Excellence for Mineralogical Archaeometry and Conservation Research, Mainz, Germany, research assistant
02/2002 – 06/2005	Institute for Geosciences, Johannes Gutenberg-University Mainz, Germany, student assisant
06/2000 – 08/2000	Max-Planck-Institut for Chemistry, Mainz, Germany, student assistant

List of publications

Articles published in peer-reviewed journals

Nasdala, L., Ruschel, K., Rhede, D., Wirth, R., Kerschhofer-Wallner, L., Kennedy, A.K., Kinny, P.D., Finger, F. & Groschopf, N. (2010): Phase decomposition upon alteration of radiation-damaged monazite–(Ce) from Moss, Østfold, Norway. *Chimia*, 64:705–711.

Ruschel, K., Nasdala, L., Rhede, D., Wirth, R., Lengauer, C.L. & Libowitzky, E. (2010): Chemical alteration patterns in metamict fergusonite. *European Journal of Mineralogy*, 22:425–433.

Gieré, R., Williams, C.T., Wirth R. & Ruschel, K. (2009): Metamict Fergusonite-(Y) in a spessartine-bearing granitic pegmatite from Adamello, Italy. *Chemical Geology*, 261:333–345.

Nasdala, L., Miletich, R., Ruschel, K. & Váczi, T. (2008): Raman study of radiation-damaged zircon under hydrostatic compression. *Physics and Chemistry of Minerals*, 35:597–602.

Articles submitted to peer-reviewed journals

Ruschel, K., Nasdala, L., Kronz, A., Hanchar, J.M., Többens, D.M., Škoda, R., Finger, F. & Möller, A. (2011): A Raman spectroscopic study on the structural disorder of monazite–(Ce). Submitted to *Mineralogy and Petrology*.

Ertl, A., Schuster, R., Hughes, J.M., Ludwig, T., Meyer H.-P., Finger, F., Dyar, M. D., Ruschel, K., Rossman, G.R., Klötzli, U., Brandstätter, F., Lengauer, C.L. & Tillmanns, E. (2011): Li-bearing tourmalines in Variscan granitic pegmatites from the Moldanubian nappes, Lower Austria. Submitted to *European Journal of Mineralogy*.

Abstracts published

Nasdala, L., Grambole, D., Ruschel, K. & Hanchar J.M. (2011): Irradiation effects on the luminescence of monazite. Joint Meeting, 19th Annual Meeting of the German Crystallographic Society, 89th Annual Meeting of the German Mineralogical Society, Annual Meeting of the Austrian Mineralogical Society (MinPet 2011), Salzburg, Österreich,. p. 60.

Nasdala, L., Ruschel, K., Rhede, D., Wirth, R., Kennedy, A.K., Kinny, P.D., Finger, F. & Groschopf, N. (2010): Phase decomposition upon alteration of radiation-damaged monazite-(Ce) from Moss, Østfold, Norway. International Mineralogical Association General Assembly, Budapest, Hungary, *Acta Mineralogica-Petrographica*, Abstract Series, vol. 6, p. 692.

Ruschel, K., Nasdala, L., Rhede, D., Wirth, R., Lengauer, C.L. & Libowitzky, E. (2009): Effect of fluid-driven chemical alteration on radiation-damaged fergusonite. *Mitteilungen der Österreichischen Mineralogischen Gesellschaft*, 155, p. 138.

Nasdala, L., Ruschel, K., Hanchar, J.M., Kramar, S., Petautschnig, C., Preuschl, F., Pristacz, H. & Talla, D. (2009): Photoluminescence emission of Rare Earth Elements in natural monazite and synthetic orthophosphates. *Mitteilungen der Österreichischen Mineralogischen Gesellschaft*, 155, p. 112.

Nasdala, L., Grötzschel, R., Probst, S., Ruschel, K. & Hanchar, J.M. (2009): Irradiation damage in monazite: A Raman study of Au-irradiated FIB foils. MinPet2009 & 4th Mineral Sciences in the Carpathians Joint Conference, Budapest, Hungary, *Mitteilungen der Österreichischen Mineralogischen Gesellschaft*, 156, p. 14.

Ruschel, K., Hanchar, J.M., Nasdala, L., Kronz, A., Libowitzky, E. & Wildner, M. (2008): Spectroscopic studies of doped synthetic monazite. 12th International Conference on Experimental Mineralogy, Petrology and Geochemistry, Innbruck, Österreich, p. 83.

Nasdala, L., Krickl, R., Ruschel, K. & Váczi, T. (2008): Spectroscopic studies of radiation damage in minerals. 19th Slovak-Czech Spectroscopic Conference, Casta-Papiernicka, Slowakai., Book of Abstracts, p. 25.

Ruschel, K., Nasdala, L. & Lengauer, C.L. (2008): Annealing behaviour of natural monazite compared to other radiation-damaged minerals. 8th International Conference on Raman Spectroscopy Applied to the Earth Sciences – Sensu Latu, Ghent, Belgium, Book of Abstracts, p. 114.

Gieré, R., Williams, C.T., Wirth, R. & Ruschel, K. (2008): Metamict fergusonite-(Y) in a spessartine-bearing granitic pegmatite from Adamello, Italy. 86th Annual Meeting of the German Mineralogical Society, Berlin, Deutschland, Abstract no. 436.

Nasdala, L., Ruschel, K., Hanchar, J.M., Götze, J., Krickl, R., Seydoux-Guillaume, A.-M. & Panczer, G. (2008): Effects of structural radiation damage on cathode- and photoluminescence emissions of minerals. 2nd Central-European Mineralogical Conference (CEMC), Szklarska Poręba, Polen, Mineralogia, Special Papers, 32, p. 118.

Ruschel, K., Nasdala, L., Miletich, R., Hanchar, J.M., Wanthanachaisaeng, B. & Häger, T. (2007): Spectral changes of zircon at elevated pressure. *Mitteilungen der Österreichischen Mineralogischen Gesellschaft*, 153 , p. 98.

Ruschel, K., Nasdala, L., Finger, F., Kinny, P. & Seydoux-Guillaume, A.M. (2007): Annealing radiation damage in monazite: changes in photoluminescence and Raman spectra. (Abstract). Programme with Abstracts, 6th European Conference on Mineralogy and Spectroscopy, Stockholm, Sweden, p. 70.

Ruschel, K., Nasdala, L., Gaft, M., Schnier, C. & Schlüter, J. (2007): Photoluminescence recovery upon annealing of fergusonite. Abstract Volume, 17th Goldschmidt Conference, Köln, Deutschland, p. A861.